Spring 2012

Automated parcellation on the surface of human cerebral cortex generated from MR images

Wen Li
University of Iowa

Recommended Citation

Li, Wen. "Automated parcellation on the surface of human cerebral cortex generated from MR images."
PhD (Doctor of Philosophy) thesis, University of Iowa, 2012.
https://doi.org/10.17077/etd.dhduc5j3

AUTOMATED PARCELLATION ON THE SURFACE OF HUMAN CEREBRAL

CORTEX GENERATED FROM MR IMAGES

by

Wen Li

<u>An Abstract</u>

Of a thesis submitted in partial fulfillment of the
requirements for the Doctor of Philosophy
degree in Biomedical Engineering
in the Graduate College of
The University of Iowa

May 2012

Thesis Supervisor: Associate Professor Vincent A. Magnotta

ABSTRACT

The human cerebral cortex is a highly foliated structure that supports the complex cognitive abilities of humans. The cortex is divided by its cytoarchitectural characteristics that can be approximated by the folding pattern of the cortex. Psychiatric and neurological diseases, such as Huntington's disease or schizophrenias, are often related with structural changes in the cerebral cortex. Detecting structural changes in different regions of cerebral cortex can provide insight into disease biology, progression and response to treatment. The delineation of anatomical regions on the cerebral cortex is time intensive if performed manually, therefore automated methods are needed to perform this delineation. Magnetic Resonance Imaging (MRI) is commonly used to explore the structural change in patients with psychiatric and neurological diseases.

This dissertation proposes a fast and reliable method to automatically parcellate the cortical surface generated from MR images. A fully automated pipeline has been built to process MR images and generate cortical surfaces associated with parcellation labels. First, genus zero cortical surfaces for each hemisphere of a subject are generated from MR images. The surface is generated at the parametric boundary between gray matter and white matter. Geometry features are calculated for each cortical surface to as scalar values to drive a multi-resolution spherical registration that can align two cortical surfaces together in the spherical domain. Then, the labels on a subject's cortical surface are evaluated by registering a subject's cortical sur-

face with a population atlas and combining the information of prior probabilities on the atlas with the subject's geometry features. The automated parcellation has been tested on a group of subjects with various cerebral cortex structures. It shows that the proposed method is fast (takes about 3 hours to parcellate at one hemisphere) and accurate (with the weighted average Dice ~ 0.86).

The framework of this dissertation will be as follows: the first chapter is about the introduction, including motivation, background, and significance of the study. The second chapter describes the whole pipeline of the automated surface parcellation and focuses on technical details of every method used in the pipeline. The third chapter presents results achieved in this study and the fourth chapter discusses the results and draws a conclusion.

Abstract Approved: _____
                    Thesis Supervisor

                    _____
                    Title and Department

                    _____
                    Date

AUTOMATED PARCELLATION ON THE SURFACE OF HUMAN CEREBRAL

CORTEX GENERATED FROM MR IMAGES

by

Wen Li

A thesis submitted in partial fulfillment of the
requirements for the Doctor of Philosophy
degree in Biomedical Engineering
in the Graduate College of
The University of Iowa

May 2012

Thesis Supervisor: Associate Professor Vincent A. Magnotta

Graduate College
The University of Iowa
Iowa City, Iowa

CERTIFICATE OF APPROVAL

———————————————————

PH.D. THESIS

———————————

This is to certify that the Ph.D. thesis of

Wen Li

has been approved by the Examining Committee for the
thesis requirement for the Doctor of Philosophy degree
in Biomedical Engineering at the May 2012 graduation.

Thesis Committee: —————————————————————
                  Vincent A. Magnotta, Thesis Supervisor

                  —————————————————————
                  Gary E. Christensen

                  —————————————————————
                  Edwin L. Dove

                  —————————————————————
                  Hans J. Johnson

                  —————————————————————
                  Joseph M. Reinhardt

To my daughter, Jiaxuan Hu

ACKNOWLEDGEMENTS

ABSTRACT

The human cerebral cortex is a highly foliated structure that supports the complex cognitive abilities of humans. The cortex is divided by its cytoarchitectural characteristics that can be approximated by the folding pattern of the cortex. Psychiatric and neurological diseases, such as Huntington's disease or schizophrenias, are often related with structural changes in the cerebral cortex. Detecting structural changes in different regions of cerebral cortex can provide insight into disease biology, progression and response to treatment. The delineation of anatomical regions on the cerebral cortex is time intensive if performed manually, therefore automated methods are needed to perform this delineation. Magnetic Resonance Imaging (MRI) is commonly used to explore the structural change in patients with psychiatric and neurological diseases.

This dissertation proposes a fast and reliable method to automatically parcellate the cortical surface generated from MR images. A fully automated pipeline has been built to process MR images and generate cortical surfaces associated with parcellation labels. First, genus zero cortical surfaces for each hemisphere of a subject are generated from MR images. The surface is generated at the parametric boundary between gray matter and white matter. Geometry features are calculated for each cortical surface to as scalar values to drive a multi-resolution spherical registration that can align two cortical surfaces together in the spherical domain. Then, the labels on a subject's cortical surface are evaluated by registering a subject's cortical sur-

face with a population atlas and combining the information of prior probabilities on the atlas with the subject's geometry features. The automated parcellation has been tested on a group of subjects with various cerebral cortex structures. It shows that the proposed method is fast (takes about 3 hours to parcellate at one hemisphere) and accurate (with the weighted average Dice ~ 0.86).

The framework of this dissertation will be as follows: the first chapter is about the introduction, including motivation, background, and significance of the study. The second chapter describes the whole pipeline of the automated surface parcellation and focuses on technical details of every method used in the pipeline. The third chapter presents results achieved in this study and the fourth chapter discusses the results and draws a conclusion.

TABLE OF CONTENTS

LIST OF TABLES

LIST OF FIGURES

ix

LIST OF ALGORITHMS

Algorithm

CHAPTER 1
INTRODUCTION

1.1 Structures and Functions of Human Cerebral Cortex

The brain is the center of the nervous system of a human being. It has the most complex biological structure known. It is made of soft tissue floating in cerebrospinal fluid and protected by the skull. Between the brain and skull, there is a succession of three-layer connective tissue membranes called meninges. Major arteries and veins that supply the brain lie among the meninges.
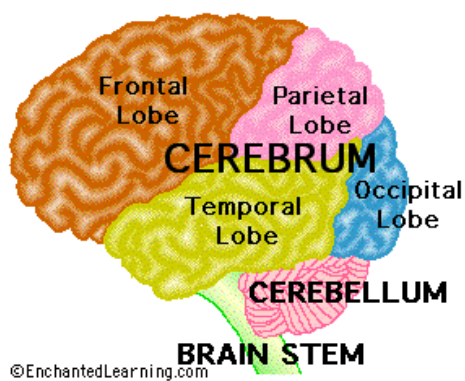
Figure 1.1: The major components of an adult human brain.

Source:http://www.enchantedlearning.com.

An adult human brain can be divided into three components: cerebrum, cerebellum, and brainstem[1] (see Fig.1.1). The cerebrum consists of two cerebral hemispheres (left and right hemisphere) and the diencephalon. Left and right cerebral hemispheres are separated by the medial longitudinal fissure. Each hemisphere is

covered by a layer of white matter, with a layer of gray matter on top of it. The gray matter is about 2-4 mm thick and is also called cerebral cortex. The gray matter is composed of nerve cells, while the white matter is composed of myelinated nerve cell axons that carry information between nerve cells and the spinal cord. The cerebral cortex is a highly folded structure and the size of it is significantly bigger in human beings than in any other kind of animals. Topographically, the surface of the cerebral cortex appears as a highly convoluted structure with sulci buried deeply between gyri. A huge amount of the surface area, along with neurobiological information that could be clinically relavent, is buried in the groove of the folded structure. If we could iron the surface of cerebral cortex to be flat, the surface area would become 4 times of the area of the exposed cortex[2].
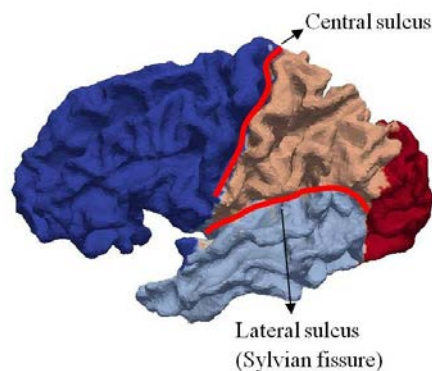
Figure 1.2: Brain lobes and fissures. The positions of central sulcus and Sylvian fissure on lateral view of the labeled surface of one hemisphere of human cerebral cortex (dark blue: frontal lobe; tan: parietal lobe; light blue: temporal lobe; red: occipital lobe).
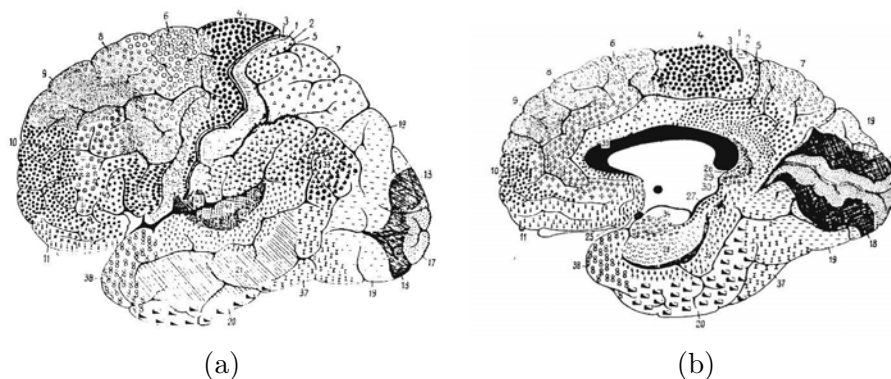
Figure 1.3: Brodmann's areas of human cerebral cortex[3]. (a) The lateral surface. (b) The medial surface.

The cerebral cortex is the most important part of the human brain, not only because it contains two-thirds of the neuronal mass and three-quarters of the synapses, but also because it plays a key role in high-level human functions, like memory, language, consciousness, planning, etc. Each hemisphere of the cerebral cortex can be divided into four (frontal, temporal, parietal, and occipital) lobes, by some obvious sulci or gyri landmarks on the cortex, as shown in Fig. 1.1. For example, the central sulcus can be used to separate the parietal lobe from the frontal lobe, and the lateral sulcus (Sylvian fissure) can be used to separate the temporal lobe from the frontal lobe (see Fig. 1.2).

In 1909, a German neurologist, Korbinian Brodmann, published his research on cortical cytoarchitectonics. He labeled 52 distinct areas (see Fig. 1.3) in human cortex according to their cytoarchitectonic characteristics using the Nissl stain[3]. Those areas are well known as Brodmann's areas and have been widely used in the study of brain structures and functions since they were published. In 1925, Economo and

Koskinas published another atlas of cytoarchitectonics of the adult human cerebral cortex with 107 areas[4].

Brodmann et al. labeled the subregions of human cerebral cortex based on "looking" differently under the microscope. The question is, do those cytoarchitecturally different areas also have different functionalities? Scientists have been working on understanding the relationship between structure and function of human brain for centuries. In the Middle Ages, philosophers and naturalists predicted that the mental "behaviors" could be localized in the "three cerebral ventricles". At the beginning of the 19th century, the anatomist, Gall, first described the difference between the gray matter and the white matter. He also pointed out that human "functions" were controlled by particularly and strictly localized areas of the brain.

Brodmann believed that "the function of an organ is correlated with its elementary histological structure". Sanides did the cyto- and myeloarchitecture studies of the human frontal lobe[5]. Sanides's work verified the fact that the shape of the nerve cells is modifiable and the volume and arrangement of nerve cells are relative to their functions. The cyto-myeloarchitectural study led to the conclusion that the vast majority of outlines of the human cerebral cortex are located in the indentations (sulci) of the cortical surface. Based on this conclusion, Sanides defined 8 "zones" of the frontal lobe and studied the functions of the frontal "zones"[5]. In late 20th century, a neuroscientist from Johns Hopkins University, Vernon Mountcastle, discovered the columnar organization of the neocortex[6]. According to Mountcastle's discovery, areas of the cerebral cortex are composed of modules. Those modules are

also called "cortex columns". Each module can be looked at as a local neural circuit that processes information from its input to its output, so it can be treated as a functional unit. And each module consists of basic functional units, "minicolumns". Modules are grouped into cortical areas according to their common or dominating extrinsic connections, which explains why certain functions can be located on certain areas of the brain. For example, the primary motor and sensory cortices have single dominating extrinsic connections and these areas also have distinct cytoarchitectural identifications from other cortices. His discovery shed light on the research of the relationship between structure and function of the human brain.

Before any medical imaging technology occurred, functions of human cerebral cortex can be observed by the responses of subjects who have partial cortex damage caused either by brain lesions or surgical ablation. That's how people in the middle 19th century recognized that the anterior part of cerebral cortex is more related with motor functions than the posterior part of it and that the posterior part of cerebral cortex is more related with sensory than the anterior part of it.

Later in modern science, Positron-emission tomography (PET) and functional magnetic resonance imaging (fMRI) are two types of most commonly used technologies to study functions in the human brain. Luria divided the cortex into two functional parts: one is the sensory unit and the other is the motor unit[7]. Overall, the cerebral cortex can be divided into three types of areas and each of these areas itself is hierarchical in structure: (1) motor area, including primary and secondary motor areas, (2) sensory area, including primary and secondary sensory areas, and (3) ter-

tiary, or association areas. Here, the primary area receives impulses from or sends impulses to the periphery; the secondary area is where the incoming information is processed; and the tertiary area is for the complex forms of mental activity requiring the concerted participation of many cortical areas. It is well accepted to provide the Brodmann area numbers associated with activation foci in a brain functional imaging study for publications. Table 1.1 shows the functions of a human cerebral cortex with corresponding Brodmann's area by numbers.

Table 1.1: Brodmann's Numbers at Functional Areas on the Cerebral Cortex

Function		Brodmann's Area
Vision	Primary	17
	Secondary	18, 19, 20, 21, 37
Auditory	Primary	41
Body Senses	Primary	1, 2, 3
	Sensory, tertiary	7, 22, 37, 39, 49
Motor	Primary	4
	Secondary	6
	Eye movement	8
	Speech	44
	Motor, tertiary	9, 10, 11, 45, 46, 47

Source: Kolb and Whishaw's study[8].

The cerebral cortex is also responsible for "higher-order" functions including language, memory, perception, thought, and planning. Specifically, each lobe of the cerebral cortex has specific functions[9]. The frontal lobe is involved in motor control and cognitive activities, such as long-term memory, planning, predicting the conse-

quences in the future for the present behaviors and making decisions. The temporal lobe is involved in auditory functions, language, and visual recognition. The parietal lobe is involved in sensory perception, attention, spatial reasoning, and language. The functions of the occipital lobe are mostly related with vision. The occipital lobe processes the visual information and passes its conclusions to the parietal lobe and the temporal lobe.

1.2 Cortical Morphology Caused by Brain Diseases

Brain disease includes any abnormality that happens in the head, such as headaches, brain tumors, vascular problems, infections, epilepsy, head trauma, and demyelinating diseases. However, the research about the relationship of brain diseases with changes of brain structures is more complicated. Brain structures can be affected by the brain disease, and also by other factors, such as gender, age, gene, environment, etc. By using the proper groups of control subjects, the deformation of anatomical structures can reflect the underlying pathology and may determine the clinical phenomenology. The deformation of brain structures can be shrinkage (atrophy) or enlargement of certain regions. Morphometric study is commonly used to detect the structural changes, like size and shape of objects[10][11][12]. The combination of morphometric study with modern medical imaging technology can be useful for diagnosis and treatment of brain diseases.

Headaches are the most common kind of brain diseases, and most headaches are related with migraines. The migraine is a common, chronic, and usually inherited neurovascular disorder[13]. Its syndrome involves a moderate to severe, recurrent,

unilateral or bilateral headache, which could last for hours or days, accompanied by nausea, photophobia, or phonophobia[14]. The trigeminal pain of migraine is associated with activations of several areas in cerebral cortex, such as insular cortex, anterior cingular cortex, and somatosensory cortex[15]. Until recently a common belief in the scientific community was that people who suffered from headaches, including migraines, tension type headaches and cluster headaches, had abnormal brain function yet completely normal brain structure. However, in 1999 May et al. reported that a significant structural difference in gray matter density between patients with cluster headaches and the healthy control group was detected by a voxel-based morphometric (VBM) study on headaches[16]. The researchers in this study acquired structural T1 weighted images using magnetic resonance imaging (MRI). Then in 2005, the chronic tension type headache was shown to be related with significant cell loss in gray matter[17]. The relationship between migraine and brain structural change is still under debate. One group proposed that no change can be detected in the brain structure of migraine patients[11], while another study showed that structural difference can be detected in the gray matter using a high-field (3 Tesla) MRI scanner[10].

Brain tissues shrink with aging. The first detection of neuron loss in an aging brain was reported by Brody in 1955[18]. Good et al. proposed that the global volumn of the gray matter decreases linearly with age while the global volumn of the white matter does not[12]. Magnotta et al. performed a study about the quantitative measurement of gyrification in the human brain[19]. It shows that shapes of gyri and

sulci of cerebral cortex change significantly along with aging. Gyri become thinner and more curved, while sulci become more flattened. Another study evaluating gender differences in brain aging shows that the brain size changes significantly greater in men than in women for the peripheral (sulcal) cerebrospinal fluid volume, the lateral (sylvian) fissure cerebrospinal fluid volume, and the area of the parieto-occipital region[20].

A number of psychiatric and neurological disorders have been shown to have accelerated age adjusted atrophy of the cerebral cortex. Double et al.[21] proposed that the significant brain atrophy may not be a consequence of the advancing age and that it could be a suggestion of Alzheimer's Disease (AD). It is well accepted among scientists that the cerebral atrophy always happens to AD patients[22]. The medial temporal lobe (MTL) is thought to be the most vulnerable region where the AD related cerebral atrophy could happen, so a large amount of publications have focused on the study of volumetric measurements of MTL in MR images[23][24][25][26][27][28][29][30][31]. People with hippocampal atrophies detected by MRI, along with memory complaints, may be considered to be in the early stage of AD[32][33][34][35].

Schizophrenia is a major type of mental disorder. Schizophrenia does not just cause mental disorders; schizophrenic patients die 12-15 years earlier than the average population. It causes more loss of lives compared with other major mortal diseases like cancer. It has been shown that schizophrenia syndromes are associated with the dysfunction of the prefrontal cortex[36][37][38][39]. Andreasen et al. studied the relationship between ventricular enlargements with the positive or negative symptoms

of schizophrenia, which presented the potential possibility of classifying schizophrenia based on a measure of brain structure[40]. Andreasen reviewed the potential role of structural MRI of a human brain in the morphometric studies of abnormal and normal brains, and pointed out that the structural change detected in vivo MR images of human brain could help us better understand the underlying mechanisms and the development of psychiatric diseases such as schizophrenia[41]. With the development of modern neuroimaging techniques in the past decades, a large number of studies have been performed to evaluate brain structure changes associated with schizophrenia and its progression. Meta-analysis shows that schizophrenic patients have overall smaller cranial or cerebral size[42][43], with enlarged ventricles[42][44]. Goldstein, et al. studied the structural difference between schizophrenia patients and healthy subjects[45]. They divided the neocortex into 48 bilateral PUs (parcellation units) based on major fissures and specified single nodal points. Significant cortical abnormalities were discovered in schizophrenia patients, which were localized primarily in regions of prefrontal and medial paralimbic cortices. The major reductions of frontal lobe in schizophrenia patients were in the middle, medial and right-sided fronto-orbital cortices. Yamasue, et al.[46] parcellated the prefrontal and temporal lobes of 27 schizophrenia patients and 27 age-, gender-, and parental socioeconomic-status-matched healthy control subjects into 15 subregions in each hemisphere (30 regions of each subject) on high resolution MRI scans of them. They concluded that the most significant gray matter reductions happens in the bilateral anterior cingulated gyrus (ACG), compared with healthy subjects. Patients with dysbindin-

associated schizophrenia were founded to have reduced occipital and prefrontal brain volumes[47].

Parkinson's Disease (PD) is defined by NIH (National Institutes of Health) to be one of a group of conditions called motor system disorders, which are the result of the loss of dopamine-producing brain cells[48]. The disease is characterized by four primary symptoms: rest tremor, bradykinesia, rigidity, and loss of postural reflexes. Motor cortex dysfunction was revealed by functional studies of human brains with PD[49], and cortex abnormalities of PD have been studied to understand the pathology of brain dysfunctions caused by the disease. VBM was used to study the cerebral atrophy in PD with and without dementia[50]. Bilateral reductions of the gray matter volume in the temporal lobe and occipital lobe were found in Parkinson's Disease with dementia (PDD) patients. The right frontal lobe and the left parietal lobe were also shown to have volume reductions by comparison with healthy control subjects. Only reduced gray matter in the frontal lobe was shown in PD without dementia, compared with control subjects. By comparing PDD patients with PD patients, significant bilateral gray matter atrophy in the occipital lobe was observed in PDD patients.

Huntington's Disease (HD) is a type of neurodegenerative disease in the human brain. It is a progressive, genetic, and familial disorder which can be passed down from parents to children. From the genetic point of view, HD is an autosomal-dominant disorder because of an expanded CAG repeat on the short arm of chromosome 4[51]. HD is characterized by progressive motor disorders, psychiatric disturbances, and cog-

nitive declines. Significant losses in the cerebral cortex volume were detected by the study of Monte, et al[52]. The study also showed that the size of the ventricular system is much bigger in HD patients than in healthy control subjects. The global brain atrophy in HD patients was also reported by Henley et al[53]. The cross-sectional and longitudinal studies were performed to choose a biomarker for the rate of brain neurodegenerative changes among gray matter, white matter, and cerebral spinal fluid (CSF) in HD patients[54]. Quantitative measurements of those brain structures were made in MR images among groups of subjects with presymptomatic to advanced HD. All of the subjects had CAG repeat expansion in their genes. The study showed that both of the gray matter volume and the white matter volumn decrease in the presymptomatic subjects, while CSF volume not only increases years before onset but it is also related with the CAG mutation size. Hobbs et al.[55] did a longitudinal MR imaging study showing that differences in caudate and ventricular volumes between HD patients and healthy control occurr earlier than motor symptoms. Aylward et al. published that the change of the volume in the white matter could be significantly related with HD[56]. The same PREDICT-HD group from Iowa also did the research among prodromal HD patients and healthy controls. They found signifiant atrophy in parietal lobe and occipital lobe of prodromal HD compared to controls. Five regions in the cerebral cortex were found to have significantly smaller surface areas as compared to controls[57].

In summary, we can see that changes in brain structures can provide a biomarker to aging, neurodegenerative diseases, dementia, or other brain disorders. In order to

detect those changes, the development of MRI technology allows neuroanatomical structures to be visualized in vivo. Manual tracing of brain structures on MR images are used commonly to do some quantitative measurements, such as volume, shape, and tissue characteristics. Automated VBM studies have been used to combine with advanced image processing techniques, so that there are no human disagreements among different experts when we use manual tracing. We believe that the automated parcellation on structural MRI images can help identify subregions of human cerebral cortex and it can also help us better understand the change of brain structure and function caused by aging, neurological disease or other diseases in human brain.

1.3   Cerebral Cortex Parcellation

"Parcellation" means to divide into parcels. It is a technique that is used to label the entire cerebral cortex in neuroanatomical studies. Once the cortex is labeled, regional quantitative measurements can be made on subregions to help us study and understand more about the human brain. The human cerebral cortex has been the major focus of psychiatry to understand the pathophysiology of mental illnesses. As mentioned in Sec. 1.1, the structure and the function of the human brain is closely related to each other. Some brain diseases have been observed to be related with structural changes in some particular regions of cerebral cortex, like medial temporal lobe in AD patients[23][24][25][26][27][28][29][31], while some other diseases are related with changes in several regions simultaneously, such as the frontal lobe and the temporal lobe in Schizophrenia patients[46], the frontal lobe and the parietal lobe in PD patients[50], etc. In order to understand better about those diseases and the

brain morphology they could possibly cause, the whole brain parcellation is preferred. Parcellation is also helpful in the study of cognitive neuroscience with fMRI. fMRI is a common tool of functional imaging technique of the human brain but it contains limited structural information, so changes in local circulation and metabolism before and after the brain responds to some stimuli are often highlighted at the activated region on the anatomical image/surface of the same subject by image/surface registration between the functional and anatomical images/surfaces (see Fig. 1.4). With the development of fMRI technology[58][59] and fMRI data analysis, SNR (signal-to-noise ratio) has been greatly increased so that task-specific brain activity can be mapped more precisely on structural MR images[60]. The parcellation of cerebral cortex can help identify and localize the activated regions for the fMRI study[61], so that we can define the functional related regions in cerebral cortex. The parcellation can be performed either on structural MR images or on surfaces generated from them as shown in Fig. 1.4.

When Brodmann, et al.[3][4][5] identified distinctive areas on the human cerebral cortex, they did it based on cytoarchitectonic characteristics, such as the shape and arrangement of nerve cells. Roland and Zilles published a review paper about how the cerebral cortex of humans can be parcelled based on structural and functional criteria[62]. According to the paper, criteria that are used to define a cortical area include cytoarchitecture, myeloarchitecture, the density of neurotransmitter receptors, the density of neurons, the density of enzymes, the architecture of synapses, etc. In the functional parcellation of the human cerebral cortex, the population map
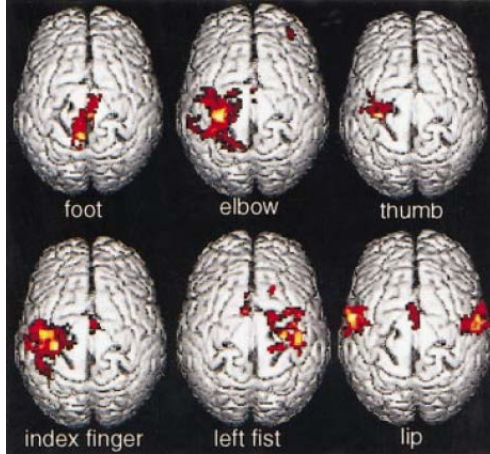
Figure 1.4: A fMRI group study that maps activated motor cortex on the cortical surface. It can be seen from the mapping which area on cerebral cortex is activated by the movement of the foot, elbow, thumb, index finger, left fist and lip.

is used to eliminate the inter-individual variation, so that functional domains can be determined. The correspondence between structure and function of cortical areas were also studied by Roland and Zilles in the review paper.

Structural MRI does not have the capability of presenting the cytoarchitectonic map of human cerebral cortex *in vivo*, but high-resolution structural MRI (1.5T, 3T) provides a clear visualization on anatomical landmarks of the human brain *in vivo*. It is common to use gyri and sulci as landmarks to define functionally relevant regions on MR images[63] [64][65]. Rademacher and colleagues used the "limiting sulci" and a set of coronal planes to do the parcellation on T1 weighted images[66]. Crespo-Facorro and Kim, et al. published a series of papers about how to parcellate the frontal lobe[67], the temporal lobe[68], and the whole cerebral cortex[69], based on multi-modal (T1, T2 and PD weighted) structural MR images. By visu-

alizing three orthogonal planes (axial, sagittal, and coronal) of MR images and the 3-dimensional rendering of cortical surface simultaneously, Crespo-Facorro and his colleagues were able to parcel the cerebral cortex into 41 regions[69]. The reliability of their parcellation was proved by intra-class correlation study and the validity (structure-function correlation) of the parcellation was supported by the PET study in the same institution of the University of Iowa.

Manually labeling the entire cerebral cortex on MR images could be both labor-intensive and time-consuming. Even an experienced rater with neuroanatomical knowledge and familiar with the neuroimaging technology needs 12-14 hours to finish a complete cerebral cortex parcellation for one subject on the regular MR images[69], and it takes up to a week to finish it on the high-resolution MR images[70]. The manual parcellation is prone to the intra-rater or the inter-rater variation as well. Therefore, we propose a fast and automated method to do the parcellation on the human cerebral cortex using structural MR images, which can produce stable and reliable results.

Basically, automated parcellation systems try to mimic how manual parcellation does the work by collecting various information including image intensity values, global position in the brain, local position relative to neighboring brain structures, and anatomical landmarks[70]. Generally, there are two types of automated approaches for cortical parcellation on MR images. One approach is based on the image/surface registration and the other is based on the image/surface segmentation. The basic idea of the first approach is to register a subject with an atlas. The brain atlas can be a

single subject randomly selected from the training set or a population atlas generated from the training set. The deformation field generated from the registration is used to warp labels from the atlas to the subject. The basic idea of the second approach is to be able to identify sulci or gyri patterns of cerebral cortex based on image/surface segmentation methods and to delineate subregions automatically using the identified sulci or gyri[71][72][73]. This dissertation will discuss about the methodologies of both approaches in the next chapter but it will focus on the first approach, because the proposed method is based on the surface registration.

A brain atlas of cortical parcellation provides the anatomic, cytoarchitectonic or functional labels in a standard coordinate system[74]. The most famous single-subject atlas is the "Talairach-Tournoux" atlas[75]. The atlas has brain structures labeled on transverse (axial), sagittal, and coronal slices from the post-mortem brain of a 60-year-old French woman (the "Talairach Brain"). The Talairach axes are constructed based on the line connecting the anterior commissure and the posterior commissure (AC-PC line) of the brain[75](Fig. 1.5a). Only one hemisphere is labeled, so the symmetry must be assumed. Talairach and Tournoux labeled the brain slices with anatomical labels, including important sulci and gyri. They also estimated the Brodmann cytoarchitectonic areas on it (shown as numbers in Fig. 1.5b). They gave the Brodmann's numbers based on their estimation on a comparison of the gross anatomy of the Talairach brain with the well-known map published by Brodmann. The atlas also described a simple set of scaling (the proportional grid) system that can be used to transform one brain to another so that they can be roughly matched overall

based on the brain size and shape. The "Talairach-Tournoux" atlas is a standard atlas with a standard coordinate system and with both of anatomical and cytoarchitectonic labels, so it is common that a subject's brain is registered with the atlas to localize the activated regions with Brodmann's numbers in functional imaging studies. The automated labeling of brain structures can be done in the standard stereotaxic space.

(a)   (b)
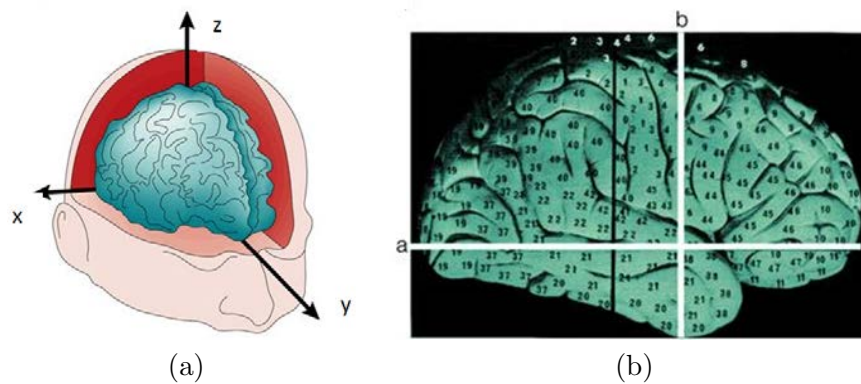
Figure 1.5: The Talairach atlas and associated coordinate system[76].

Andreasen et al.[77] did automatic volume estimation of large scale human brain region of interests (ROIs) on MR images. The subject's MR images are wrapped into an adapted Talairach atlas by the linear transformation. Then, 12 ROIs are labeled on the subject's brain including brain lobes (frontal, parietal, temporal, and occipital), cerebellum, and subcortical regions on both hemispheres. Manual delineation of those regions are treated as "gold standard" and used to evaluate the automatic results.

A database and server called "Talairach Daemon" was development by Lan-

caster and Fox for neuroanatomical labeling of Talairach coordinates[78][79]. Each subject's brain MRI is normalized using Talairach's coordinates. A "forward transform" (from subject to atlas) method is used to retrieve brain labels by the coordinates of the brain. The automated labeling system is evaluated by calculating the matching of the automated labels with several reference labels. The results shows a high dependence on the search range in Talairach space[79]. However, it still needs human interaction because it is possible that a voxel could get a label that it is unlikely to belong to. An expert is needed to verify the result and decide whether to accept the label or not.

The "inverse transform", which is used to transform a volume of interest (VOI) from the atlas to a subject and to label the subject's brain was developed by Collins and his fellows on MR images[80][81][82]. Linear or non-linear image registration is used to align the subject's brain with an atlas (single subject atlas[82] or average atlas[80][81]). The anatomical labels on the atlas are then mapped to the subject using the deformation field generated by the image registration. All of the MR images are normalized into a standard coordinate system of either the standardized Talairach space[80] or Talairach-like space[81][82]. The method is shown to have over 85% volumetric overlapping, but it is only used to label certain brain structures and has not been tested in the whole brain parcellation yet.

Even though "Talairach-Tournoux" atlas provides a standard coordinate system and detailed anatomical labels, it is inaccurate[61] (Fig. 1.6). In addition, it uses Brodmann's Areas to label brain structures while Brodmann's Areas are based on

cytoarchitectural features which may not be able to represent the exact relationship between functional and structural anatomy in human brain. And it has been shown that there exists a large inter-subject variability in cytoarchitectonic areas[83][84], so Brodmann's labeling cannot be considered as reliable.

Due to the substantial inter-individual variability of the topographic patterns of human cerebral cortex[85][86], bias exists in a single subject atlas when it is used as a model for cortical parcellation. The amount of inter-individual variability still remains from 9 to 18 mm even after an affine stereotaxic normalization[87]. The brain atlas generated from a large population of subjects has the advantage of showing the least deviation in shape and surface features over a single subject atlas[88]. Thus, a good atlas can encode local anatomic variability and also cortical topography. The construction of population atlas needs to incorporate high-dimensional non-rigid image registration to align the anatomy of a group of subjects together. The size of high-resolution brain MR images and the complexity of non-rigid intersubject registration both demand the use of automated computer-based construction of brain atlases[89][90]. Image registration is the key issue to generate the digital atlas. A comprehensive survey of the application of various image registration techniques on brain functional localization was published by Gholipour et al.[60]. Typically, either volume registration or surface registration can be used to align different brains together using their MR images. Volume registration does it by matching the size and shape of different brains with each other or warping both of them into a standard brain template, based on voxel intensity values or anatomical features shown in

Figure 1.6: The overlay of the "Talairach-Tourmoux" atlas on the MNI average atlas (a) The overlay of "Talairach-Tournoux" atlas on MNI (Montreal Neurological Institute) average brain of 152 subjects. (b) The overlay of "Talairach-Tournoux" atlas on MNI average brain of 152 subjects after non-linear correction. (c) The overlay of "Talairach-Tournoux" atlas on MNI single subject brain after non-linear correction. (The pictures were copied from Tzourio-Mazoyer's paper[61])

T1 or T2 weighted MR images. An anatomical textbook was proposed by Miller et al., it is an image template with a vector as the pixel value in an ideal coordinate system. The vector contains intensity values from multi-modality imaging methods, such as MR T1 and T2 images, CT images, and functional PET images, as well as anatomical labels and histological information. The informations (labels) in the textbook are then brought into the coordinates of a new subject by a deformable image transformation[91]. Iosifescu and his fellows managed to delineate 11 brain structures based on the atlas-to-subject image registration on MR images. The registration technique they used is a combination of linear registration on the surface and elastic registration on the volume images. The resulting deformation field from the registration is then used to warp manual labels from the atlas to the subject and the result is evaluated by measuring the volume of the delineated brain structures[92]. However, the propagation of the anatomical labels from the atlas to the subject based on the image registration is considered to have limited accuracy, so Heckemann et al. proposed a method of brain MRI segmentation combining the label propagation with the decision fusion[93]. The decision fusion is an alternative option of average atlas to eliminate inter-individual variabilities. Heckemann's combining method is tested on a dataset of 30 normal brain MR images. Each subject's brain was manually labeled with 67 regions. One subject is registered with each of the rest 29 subjects based on the 3D voxel-based registration using MR images. Thus, the registration can generate 29 transformations. The resulting transformations are then used to warp labels from the 29 subjects onto the first subject. Vote rules are used to fuse 29 labels and

assign an anatomical label to each voxel on the subject. 12 out of 67 brain structures are selected to verify the method. Sabuncu et al. improved Heckemann's method by proposing a probabilistic model to perform decision fusion of labels transferred from multiple atlases. Alzheimer's disease related brain structure, hippocampal is included in their experiment of brain parcellation[94]. In 2010, Heckemann et al. developed a software called MAPER (multi-atlas propagation with enhanced registration)[95], which combines tissue classification with deformable image registration to improve the accuracy of the image-based whole brain parcellation. MAPER has been applied to automatically label 83 regions covering the whole brain in 816 subjects using T1 weighted MR images. However, the evaluation of the automated labels are mainly based on visual assessment. The Jaccard Index between segmentations of paired images acquired at different field strengths was recently reported as 0.802 ± 0.0146[96].

The surface registration is another option to align subjects with the atlas. It uses sulci and gyri on the reconstructed surface as anatomical landmarks. The geometry features that can represent the patterns of sulci and gyri are calculated to drive the registration. We think the surface registration is a better choice for the purpose of cerebral cortex parcellation based on MR images:

1. Sulci and gyri are important bio-markers that are often used to separate adjacent regions of cerebral cortex. They can be better represented on the cortical surface than on 3D volumetric MR images, and topographic features such as curvatures can be easily calculated from the cortical surface[19]

2. It is difficult to identify cortical structures only based on image intensities of

MRI. According to the study of noninvasive identification of human central sulcus performed by Towle, et al.[97], the judgments experts could make based on T1-weighted MRI slices for the location of the cortical primary motor and the sensory hand area have a mean discrepancy of 25 mm to the direct cortical mapping results, with a 48 mm discrepancy in the worst case

3. The average atlas generated from volume registration could be more attempted to blur gyral and sulcal features[98]

4. Due to the highly folded structure of the cerebral cortex, it is impossible to do some particular measurements such as calculating the distance from two points along the cortical surface using the 3D volumetric images[99]. Because of the same reason, a small inaccuracy in volume registration may cause the same point in cerebral cortex have completely different labels. For example, the secondary somatosensory and parietal ventral cortex (SII/PV), and the primary auditory cortex and adjacent areas (AI/AII) locate at opposite banks of the Sylvian fissure. Because of the lack of capability to separate them with a major distance in the 3D volumetric image, a small inaccuracy in volume registration could cause one voxel be mislabeled as the wrong structure which has a completely different function[100]. Apart from the distance, there are some other measurements which we can do better on cortical surfaces such as cortical thickness, curvature and surface area[19][101][102] that have been proved to be significant for the study of neurodegenerative and psychiatric disorders

In brief, surface registration driven by geometry features of sulci and gyri can

give us better intersubjects and atlas-to-subject alignments, both of which can benefit the cerebral cortex parcellation. Here are some of the studies that have been done on the automated cerebral cortex parcellation based on the surface registration.

FreeSurfer provides a refined tool for automated labeling of cortical surfaces. An anatomical label is assigned to each location on a cortical surface based on a probabilistic atlas constructed from a manually labeled training dataset[65][103]. Topologically corrected surfaces can be generated either between the white matter and gray matter ("white" surface), or between the gray matter and the CSF[104][105]. The "pial" surface is shown in Fig. 1.7a). FreeSurfer also provides a nice tool to morph ("inflate") the cortical surface along the negative direction of the gradient of an energy function without intersecting itself, so that the information buried inside sulci can be visualized[106] (Fig. 1.7b). The cortical surface can be further inflated into a sphere (Fig. 1.7c), while the values to represent the folding pattern of the surface are calculated during or after the process of inflation[107]. For example, "Average convexities" are calculated during the inflation to represent the large-scale folding patterns on the cortical surface as shown in Fig. 1.7b and Fig. 1.7c. Once all of the cortical surfaces are mapped into the uniform spherical coordinate system, they can be aligned together by minimizing an energy function which is used to calculate the difference of folding patterns between two cortical surfaces[99]. Once all of subjects in the training set are aligned together, an average template can be constructed from them. In the assumption that the spatial distribution of labels in cerebral cortex can be modeled by a non-stationary anisotropic Markov random field (MRF), a prob-

abilistic atlas is constructed based on the prior information of manual labels and geometry features of each corresponding point across all of subjects in the training set. After registering a new subject to the atlas, the labels on the new subject can be predicted using the MRF model. The result of automated parcellation for 36 areas on an individual subject is shown in Fig. 1.7d.

(a)   (b)   (c)

(d)
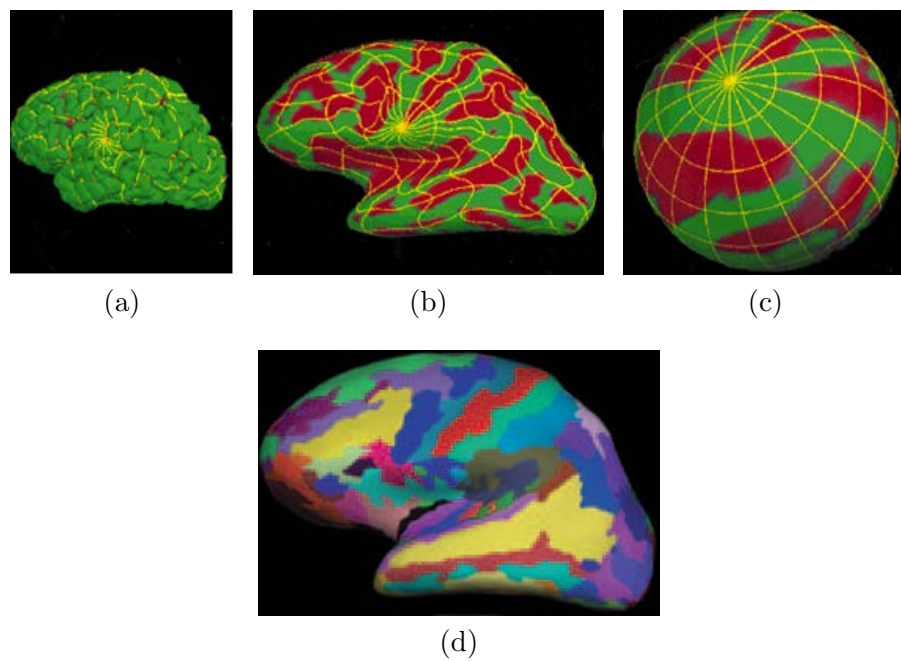
Figure 1.7: Surface representations of the cerebral cortex generated by FreeSurfer[65][103]. Red represents sulci and green represents gyri in (a), (b) and (c). (a) shows a pial surface generated from structural MRI of an individual subject. It is a surface between gray matter and CSF. (b) shows an inflated surface with convexity values on it. (c) shows an atlas generated on a sphere with the avarege folding pattern represented by convexity values. (d) shows the result of automated parcellation of 36 areas on the cortical surface of an individual subject.

Yeo, et al. proposed a fast and landmark-free surface registration method in

2010. It was applied in the automated cortical surface parcellation using MR scans of 39 subjects[108]. The detail of the algorithm is discussed in Chap. 2. Cortical surfaces of 39 left and right hemispheres were extracted from MR images. 36 regions on each cortical surface were manually labeled by a neuroanatomist. Each surface is mapped onto a sphere. Each vertex on the surface was associated with multiple geometry features: mean curvature of the cortical surface, mean curvature of the inflated cortical surface, and average convexity of the cortical surface. The multi-resolution diffeomorphic demons surface registration is performed to align cortical surfaces in the spherical domain. A probabilistic atlas is built iteratively while registering a subject to the atlas until all of the 39 subjects are co-registered. Each vertex of the probabilistic atlas contains the geometry information across 39 subjects at that location in the the mean and variance of each geometry feature across all of the subjects can be calculated. Then, 4-fold cross-validation of the automated parcellation is performed using the co-registered cortical surfaces. The Dice Index is calculated for each label to evaluate the overlapping of the automated and the manual parcellation.

Sandor and Leahy did a large-scale parcellation on the cortical surface based on the assumption that anatomically normal brains can be aligned with each other by global scaling and local deformations[109]. The MR image of a healthy subject is modeled with a B-spline surface model (Fig. 1.8). Anatomic labels are given to each point of the surface model. The B-spline surface model is first aligned to the surface of a new subject by scaling and translating to make it close to the subject's surface. Then, the B-spline surface model is deformed by minimizing an energy function to

further match with a subject's surface. Manual labels of brain lobes (frontal, pari-
etal, and temporal lobes) and large sulci labels (central, interhemispheric, and lateral
sulcus) are then transferred from the atlas to the subject, as shown in Fig. 1.9. San-
dor and Leahy's method is based on elastic deformation of an approximate cortical
surface. It used global scaling instead of a real image registration to align the atlas
with the subject, so it can only be used to delineate large-scale partitions, such as
brain lobes and major sulci. In addition, they use a single subject atlas, which is not
capable of covering the inter-individual variability of brain structures.
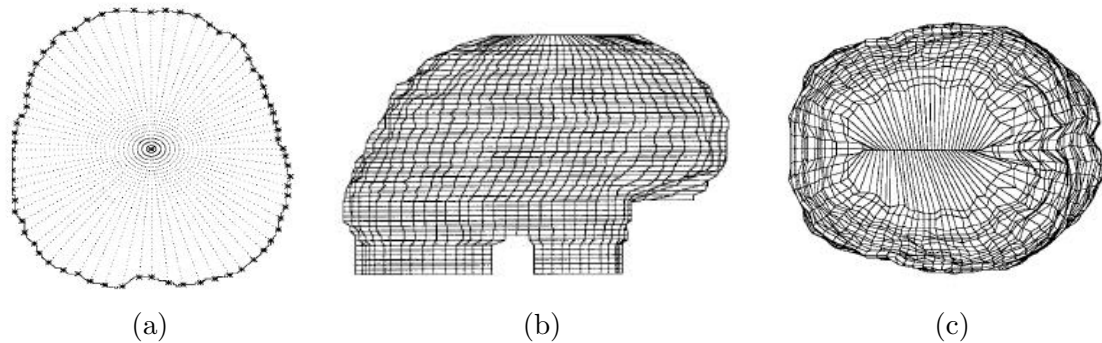
Figure 1.8: The control mesh used in the B-spline surface registration[109]. (a)
Sample points are shown as the asterisks in one slice of a closed brain image. (b) and
(c) are the lateral and top view of B-spline control mesh.

The surface atlas plays a critical role in the surface parcellation. The word
"atlas" means a collection of maps. The human brain atlas provides a reference for
anatomical structures in the human brain. Since MR images can capture details
of anatomical structures inside of human brains, it is common to generate an atlas
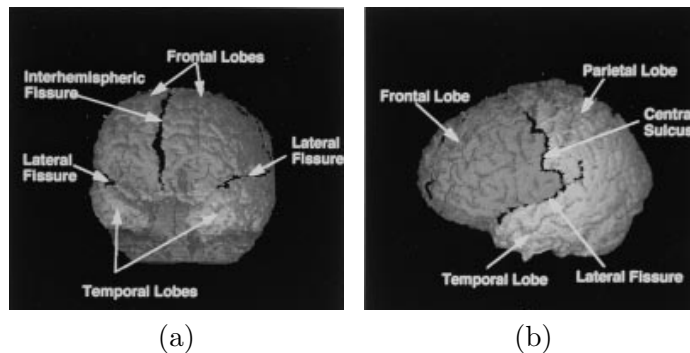
Figure 1.9: The parcellated labels generated by the B-spline surface registration[109]. (a) A frontal view. (b) A lateral view.

from MRI scans of a group of subjects or from the MRI scan of a single subject to study the structure of the cerebral cortex. Both of the approaches have strengths and weaknesses. Sec. 1.3 has reviewed methods of the MR image-based brain atlas generation. Van Essen gave a comprehensive review on generating surface-based atlases for the visualization and analysis of the cerebral cortex[110].

Sandor and Leahy used a single subject as the atlas[109]. The MR image of a male normal brain was chosen to be the atlas in their method. A smoothed brain surface was generated for each subject, with major sulci on it. The atlas' surface was labeled using major sulci as borders. Then, the brain surface of the atlas was treated like a deformable model which can warp onto a subject's surface. The model was represented by 3D B-Splines and an energy function was designed to help align sulci on the atlas surface with the ones on the subject surface. After the atlas was converged onto the subject's surface, labels from the atlas can be propagated onto the subject. The single subject atlas has the advantage of keeping sharp features, as well

as anatomical details but it is biased by that particular subject's folding pattern and therefore lacks the inter-individual variability for the population study[88][111][110].

Van Essen published a population-average, landmark- and surface-based (PALS) atlas which was generated on spheres[112]. The atlas was generated from structural MRI scans of 12 healthy adults. Cortical surfaces of 24 hemispheres were generated and mapped onto spheres. A set of six landmark contours were manually drawn on each of the cortical surfaces. They were the calcarine sulcus, the central sulcus, the Sylvian fissure, the anterior half of the superior temporal gyrus, the dorsal and ventral parts of the medial wall boundary. An initial atlas was generated by directly projecting and averaging landmark contours from 24 individual spheres on a regular atlas sphere. The regular sphere on which the PALS atlas was generated consists of 73,730 nodes. Then, individual cerebral cortex of the same group of people was registered to the initial atlas by the landmark-based surface registration, so that all 24 cortical surfaces were aligned. Data files can be attached with the atlas nodes to represent probabilistic priors of cortical shape and cortical geography. The atlas also includes the deformation mapping which can be used to map further data information from training subjects to the atlas.

FreeSurfer developed a surface atlas for the morphometric study of Alzheimer's disease (AD)[103]. It is a generalized atlas generated from 40 subjects with wide range of age and clinical status. After cortical surfaces were generated from MRI scans of training subjects, all surfaces were mapped onto spheres. The spherical surfaces were aligned with each other by FreeSurfer's multi-scale surface registration[99]. The align-

ment was performed by choosing one subject as the target surface and registering the rest of surfaces to the target surface. An atlas was thus generated on a sphere by averaging scalar values representing fold patterns across 40 subjects. Then, the training subjects were registered to the average atlas again and the scalar values on the atlas were updated. The process continues until the atlas converged. All 40 subjects were manually labeled into 34 regions on their surfaces[103]. The probabilistic information about parcellation labels was also incorporated on the atlas. The Markov random field in the first order anisotropic neighborhood was used to model the label and spatial information[65]. The spherical atlas was composed of two icosahedra spheres in different resolution level. The priors of label information are saved on a high resolution sphere with 163,842 vertices, while the curvature density at each vertex for each label is saved on a low resolution sphere with 2,562 vertices.

Lyttelton et al. presented an iterative, hemisphere-unbiased atlas generation based on the deformable surface registration[111]. The initial group average template was generated by calculating the average value of a surface feature field across 111 training subjects, 222 hemispheres, so the surface feature field on the template was coarse at the beginning. The template's surface feature evolved after each level of alignment. There are 5 hierarchy levels to finish the generation of the atlas from the initial template. The number of polygons (triangles) are 320, 1280, 5120, 20480 and 81920. The same feature field was used to align 222 hemispheres in each level. After each registration level, the surface feature of each training subject was warped onto the original template and the surface feature of the template for the next registration

level was generated by averaging the warped surface features from training subjects. Lyttelton et al. also did a study about the iterative template stability verses the number of training subjects. It shows that the template is stable at a training size of 30-50 subjects[111].

For the purpose of better understanding the structures and functions of the human brain, we propose a comprehensive framework of the surface parcellation on the human cerebral cortex, which includes:

- An automated pipeline for the surface generation on the boundary of the white matter and the gray matter based on the T1- and T2- weighted MR images.

- An automated pipeline to generate a probabilistic atlas from a group of subjects using the surface registration in a spherical domain.

- A complete solution to automatically parcellate the cerebral cortex based on the subject's MR images.

The goal of our study is to provide a fast, precise, and reproducible scheme for cortical surface generation and parcellation using MR images, and the ultimate goal of this study is to use this scheme to help us understand better how various psychiatric and neurological disorders affect the cerebral cortex.

CHAPTER 2
METHODS

This chapter presents the details of each step in the parcellation framework. It starts from the preprocessing of the T1- and T2- weighted images (see Sec. 2.2). Next, it explains how to generate the topology corrected cortical surface on the boundary of the white matter and the gray matter (see Sec. 2.3). Then, it describes what types of geometry features we calculated from the surface (see Sec. 2.4) and how to perform the surface registration (see Sec. 2.6). Sec. 2.7 describes how to propagate the labels from a single subject atlas to the subject surface. The last two sections of the chapter, Sec. 2.8 and Sec. 2.9 describe details about the surface parcellation using an atlas.

2.1   Data Acquisition

49 subjects were enrolled voluntarily into an MR imaging protocol with written consent obtained in accordance with the institutional review board at the University of Iowa. The MR protocol acquired three image sets: a T1- and T2- weighted scan. The images were obtained on a GE Signa 1.5 T MR scanner. The T1- weighted scan was acquired using a 3D spoiled recalled gradient echo sequence with the following scan parameters: TE = 5 ms, TR = 24 ms, flip angle = 40°, NEX = 2, FOV = 26 x 19.2 x 18.6 cm, matrix = 256 x 256 x 192 . The T2- weighted scans were acquired using a fast spin-echo sequence with the following parameters: TE = 28/96 ms for the T2 image, TR = 3000 ms, slice thickness/gap = 3.0 to 4.0 mm / 0.0 mm, NEX = 1, FOV = 26 cm, matrix = 256 x 192, ETL = 8.

2.2 Preprocessing

This step is to take the T1- and T2- weighted images from the MRI scan of one subject and to produce the tissue classified image for that subject. The tissue classified image is a parametric image which combines the original T1- and T2- weighted images and encodes the white matter, the gray matter and the CSF with certain ranges of intensity values in a standard coordinate system. The AutoWorkup in BRAINS (Brain Research: Analysis of Images, Networks, and Systems[77][113]) image analysis software is used to do the preprocessing[114]. The flowchart of the preprocessing is shown in Fig. 2.1 and the details are given below.

The first step of the preprocessing is the "AC-PC alignment". Anatomical landmarks such as the anterior commissure (AC) point and posterior commissure (PC) point are detected by an automated landmark constellation detection program in BRAINS[115]. The program is able to detect the AC point and the PC point in T1-weighted image and output the AC-PC aligned image, the transformation matrix from the input image space to the output image space, and the landmark files in both image spaces.

The second step is the "Multi-modal registration". The AC-PC aligned T1- and T2- weighted images are co-registered together using a rigid body registration based on the mutual information[116][117].

Then, "Brain segmentation and bias field correction" is implemented to segment the brain using a brain mask generated for each subject. The brain segmentation is performed on the co-registered T1- and T2- weighted images, and intensity inho-
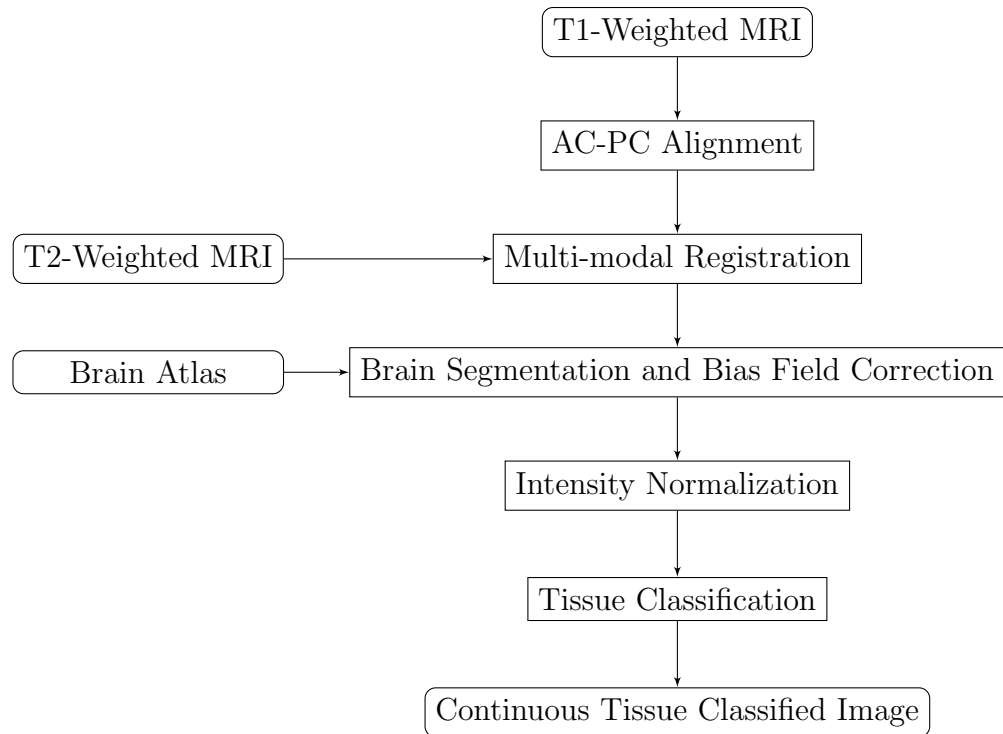
Figure 2.1: The flowchart of the preprocessing for the T1- and T2- weighted images in BRAINS AutoWorkup[114]. It is assumed that an atlas that represents anatomical structures in human brain is provided.

mogeneities caused by variations in coil sensitivity and B1 uniformity are corrected simultaneously in both modalities. Because of the inhomogeneity in images (it is also called "bias field"), the same tissue could have different gray level across the MR images. The brain segmentation based on image intensities fails to produce satisfactory results with the existence of bias field effects in the image. At the same time it is hard to remove the bias field artifacts without knowing the tissue types. Therefore, we choose the Expectation Maximization Mean Field Approximation Local Prior (EM-MF-LP) algorithm proposed by Pohl, et al.[118]. The EM-MF-LP method does the brain segmentation and inhomogeneity correction iteratively. First,

a synthesized average template of human brain[119] is registered to the subject us-
ing a B-Spline registration. Then, the probability maps of the brain tissues (gray
matter, white matter, and CSF) for the atlas are warped to the subject using the
transformation calculated by the registration. Following probability map warping, an
EM-MF loop is repeated iteratively to segment brain tissues for the subject and to
normalize the input T1- and T2- weighted images simultaneously until it converges.
The EM-MF algorithm consists of two steps: the Expectation-Step (E-Step) and the
Maximization-Step (M-Step). The E-Step calculates the weight for each voxel as the
likelihood of tissue classes and the M-Step estimates the bias field. A brain mask is
generated for the subject by combining the segmented tissue classes of the gray mat-
ter, the white matter, and the CSF. Morphological operations are used to generate a
closed brain mask.

The intensities in images of all modalities are rescaled to 0 to 255 after the
removal of extreme intensities which are in the top and bottom 0.05% of the histogram
(this is called as the "Intensity normalization" in Fig. 2.1). Fig. 2.2a shows the
outline of the resulting brain mask from "Brain segmentation and bias field correction"
superimposed on the intensity normalized T1 image of the same subject after the
"Intensity normalization".

The normalized T1- and T2- weighted images are then input to a discriminant
tissue classification to create a continuous classified image to represent the white
matter, the gray matter, and the CSF[120]. The training samples or plugs (these two
terminologies are used interchangeably in this proposal) are chosen randomly from
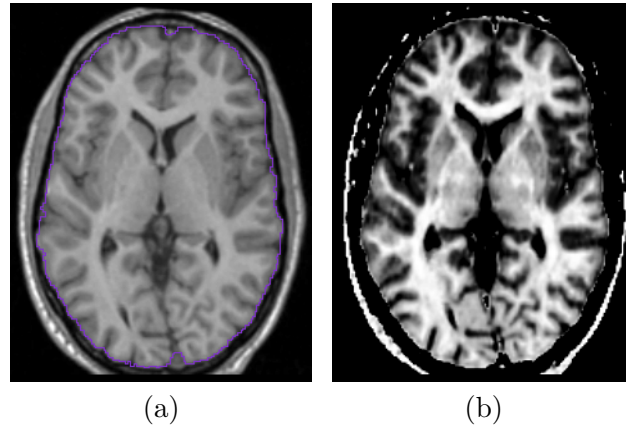
Figure 2.2: The brain mask and a tissue classified image. (a) An axial slice of the outline (in purple) of a brain mask generated by the EM-MF-LP algorithm superimposed on the T1 image. (b) An axial slice of the tissue classified image with continuous intensities for different types of brain tissues.

the estimated brain region of interest based on the T1- and T2- weighted images. The brain region is defined by the brain mask created in the "Brain segmentation and bias field correction" step. Each plug is a small block of voxels comprising $2 \times 2 \times 2mm$ region. To ensure the "purity" of the training plugs, only those plugs with intensity variances below a certain threshold are accepted. A variance threshold is set for T1 and T2 respectively at the beginning of the tissue classification based on the experienced estimation. After the variance thresholding, "Plug picking" is performed iteratively with 4000 plugs picked K-means clustering is used to assign each plug into one of the three tissue classes (white matter, gray matter, or CSF). Iterations keep going until two conditions are satisfied: One is that the minimum number of plugs assigned to each class exceed the designated parameters: 2000 white matter plugs, 4000 gray matter plugs, and 200 CSF plugs; The other condition is that the designated

minimum spatial coverage of the brain region for each class is at or above the following parameters: 85% of the extent in each direction. After the "plug picking" is done, the blood plugs are picked in a region within 5mm of the border of the brain mask. The plugs that have mean intensities in between 60% to 80% of the gray matter mean in T1 image and lower than 20% of the gray matter mean in T2 image are selected as blood samples. A fuzzy classification is used to generate a continuous tissue classified image as a result. Unlike discrete classified image, continuous classified image takes account of partial volume effects. The intensity of the resulting image represents the likelihood of the tissue belonging to a particular tissue class (Fig. 2.2b). For example, the intensity of 10 in our tissue classified image represents the CSF, 130 for gray matter, and 250 for white matter. Likewise, the voxel with the intensity of 190 means it is 50% likely to be the white matter and 50% to be the gray matter. Blood is represented by an intensity of 1 and other tissues are represented by 0 in the resulting image.

2.3   Surface Generation

Topologically correct cortical surfaces of the left and right hemispheres can be generated from the tissue classified image using BRAINS AutoWorkup[114]. The flowchart of the surface generation is shown in Fig. 2.3.

First, the normalized T1 image generated from the "Intensity normalization" is clipped using the brain mask generated from the "Brain segmentation and bias field correction" (Fig. 2.1). The T1 clipped image is displayed as "T1_clipped" in Fig. 2.4

for a hypothetical subject. Then, the skull-stripped (clipped) T1 image of the brain atlas[119] (shown as "Atlas_clipped" in Fig. 2.4) is registered to the "T1_clipped" image of the subject using a diffeomorphic demons registration[121] initiated by an affine registration. The brain masks of the left and right hemispheres, ventricles, and the cerebellum are warped from the atlas to the subject using the deformation field generated by the registration.

Atlas-to-Subject Registration and Warping

Filling up Ventricles and Subcortical Regions

Hemisphere Segmentation

Image Smoothing

Image Binarizing

Topology Correction

Surface Generation

Surface Decimation

Surface Smoothing
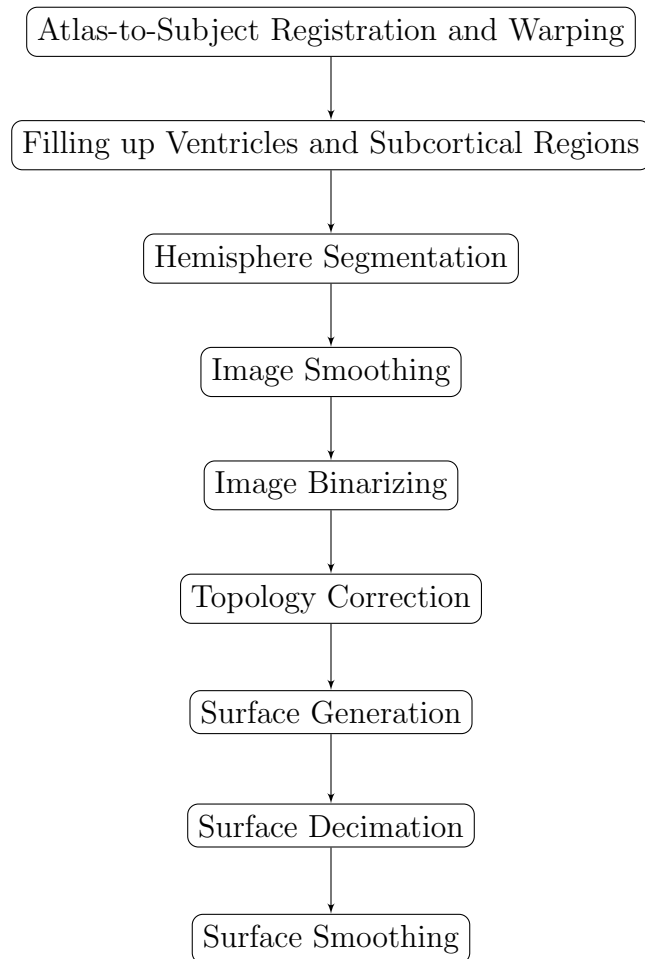
Figure 2.3: The flowchart of the surface generation based on tissue classified image.

After the atlas-to-subject registration and warping, the ventricles and subcortical structures such as the caudate, putamen, and thalamus are filled up using an intensity value of 250 in the tissue classified image ("Filling up ventricles and subcortical regions" in Fig. 2.3). The ventricle masks for each subject are generated using atlas-to-subject warping methods mentioned above to warp the ventricles atlas estimated with the Talairach atlas for each subject. An artificial neural network based algorithm is used to define the subcortical regions (caudate, putamen, and thalamus) for each subject[122]. Fig. 2.5a shows the label map of ventricles and subcortical regions overlapped on the tissue classified image of the same subject.
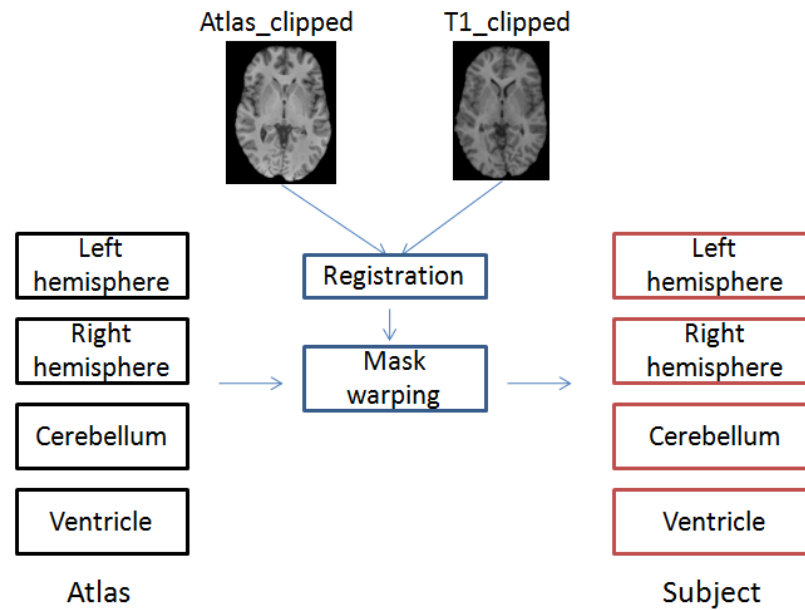
Figure 2.4: The process of the brain structure segmentation based on the image registration.

The left and right hemisphere are separated using the whole brain mask generated by the "Brain segmentation and bias field correction" step in Fig. 2.1 and the left/right hemisphere mask generated from the "Atlas-to-subject registration and warping" step in Fig. 2.3. Apply the whole brain mask and a mask of one hemisphere to the filled tissue classified image together, so that the cortical surface of each hemisphere can be generated independently ("Hemisphere segmentation" as shown in Fig. 2.3). Fig. 2.5b shows an example of the resulting left hemisphere of this step. In the meanwhile, the cerebellum is excluded from all of the segmented hemispheres using the warped mask of cerebellum. There are three steps that have been taken in order

(a)   (b)   (c)   (d)
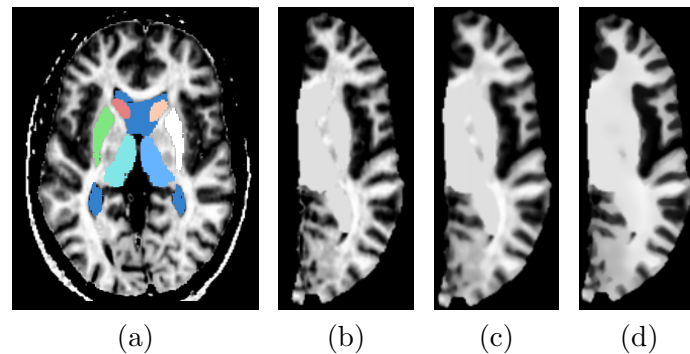
Figure 2.5: An example of applying image smoothing filters before surface generation. (a) The axial view of the label map of regions that need to be filled up overlapped on the tissue classified image. (b) The extracted tissue classified image of the left hemisphere with filled ventricles and subcortical regions. (c) The resulting image of a median filter on (b) with a radius of 1 voxel. (d) The resulting image of anisotropic diffusion filter on (c) with $t = 0.1$ in Eq.2.1 and $k = 1.0$ in Eq.2.4.

to get a smooth cortical surface. Two of them are applied to the grayscale image and

one is applied to the surface. The first step is the median image smoothing filter. The median filter is a non-linear image filter which is used to remove "impulse noise"[123]. Impulse noise is present in the tissue classified image because of the remaining skull voxels, or the errors caused by tissue classification. The median filter replaces the current voxel value by the median value in its neighborhood. It can remove the noise while preserves the edges of the input image. Fig. 2.5c shows the results of this filter on the image shown as Fig. 2.5b. Although the median filter preserves edges better than other smoothing filters, it is unable to preserve the "real" edge of our cortical surface. With edge preservation prioritized a second filter is applied to remove image artifacts while maintaining image edges. This is accomplished by applying the anisotropic diffusion filter, to further smooth the image while conserving image edges. The anisotropic diffusion filter is also a non-linear image smoothing filter which was derived from the multiscale description of image[124][125]. Traditionally, a Gaussian smoothing on a 2D original image $I_0(x, y)$ can be obtained by:

$$I(x, y, t) = I_0(x, y) * G(x, y; t) \tag{2.1}$$

where $I(x, y, t)$ is the derived image and $G(x, y; t)$ is a Gaussian kernel with the scale-space parameter t. Bigger t can be used to perform more smoothing on the image and at the cost of increased image blurring. Eq. 2.1 can be viewed as the solution of the heat equation[126]

$$\frac{\partial I(x, y, t)}{\partial t} = \Delta I = \nabla \cdot \nabla I(x, y, t) \tag{2.2}$$

with the initial condition $I(x, y, 0) = I_0(x, y)$. Δ is the Laplacian operator and ∇ is

the gradient operator. The anisotropic diffusion filter introduces a conduction term to consider the local structures of the image by applying different conduction term values to pixels in the interior of a region and to pixels at boundaries. In order to encourage smoothing within a region and not at the boundary, the conduction term is limited by the gradient magnitude, as

$$\frac{\partial I(x, y, t)}{\partial t} = \nabla \cdot c(|\nabla I|)\nabla I \tag{2.3}$$

In this study, $c(|\nabla I|)$ is set to be a function that reduces the value of c when the gradient magnitude is high:

$$c(|\nabla I|) = e^{-(\frac{(\|\nabla I\|)}{k})^2} \tag{2.4}$$

where k is the conductance parameter, which controls the sensitivity of the filter to process the edge. Fig. 2.5d shows the result of the anisotropic diffusion smoothing when applied to the median filtered image in Fig. 2.5c.

As mentioned in Sec.2.2, the intensity of the continuous tissue classified image represents the likelihood of the voxel being a specific tissue type, for example an intensity of 130 represents pure gray matter and 250 represents white matter. An isovalue of 190 is used to generate the cortical surface in this study, in order to locate the surface at the interference between white matter (130) and gray matter (250). To demonstrate the effects of smoothing filters applied on the volume voxels to surface generation, cortical surfaces generated with isovalue of 190 that is not smoothed (Fig. 2.6a), that is smoothed with the median filter (Fig. 2.6b), and that is smoothed with the median filter followed by the anisotropic diffusion filter (Fig. 2.6c) are shown in Fig. 2.6.
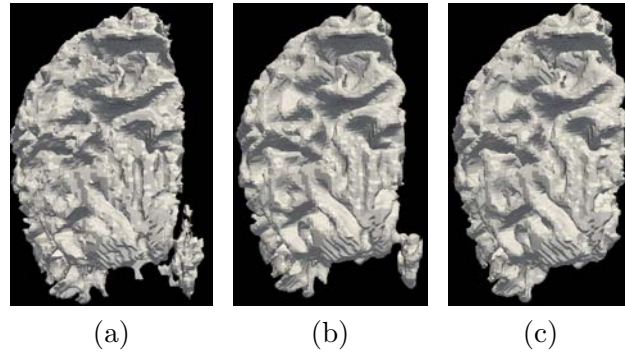
Figure 2.6: The effects of image smoothing filters on the surface generation. All of the figures are generated at the boundary of the white matter and the gray matter.

Although the median filter coupled with the anisotropic diffusion filter can remove most of the noise in tissue classified image, a triangulated surface generated directly from the smoothed image is not topologically correct (genus zero). The remaining noise (after image smoothing), the partial volume artifacts, and the remaining image intensity inhomogeneities (after bias field correction) can still cause holes or handles on the surface. The number of holes and handles on a triangulated surface can be calculated as the number of genus (g in Eq. 2.5) which can be derived from the Euler characteristic χ of the surface:

$$\chi = V - E + F = 2 - 2g, \tag{2.5}$$

where V represents the number of vertices, E the number of edges and F the number of faces on the surface. A cortical surface free from holes or handles is topologically equivalent to a sphere. The Euler characteristic of such a surface is 2 or the genus of it is 0. However, Eq. 2.5 can only be used to calculate the number of holes and handles; it does not provide any information about the size or location of them.

A tremendous amount of work has been dedicated to the automated topology correction of brain segmented images but only few methods can generate the genus zero surface in a fast and stable way. Three kinds of approaches have been tested in our study. The following paragraphs give brief description of the basic theory behind those three approaches and also analyze the strengths and weaknesses of them.
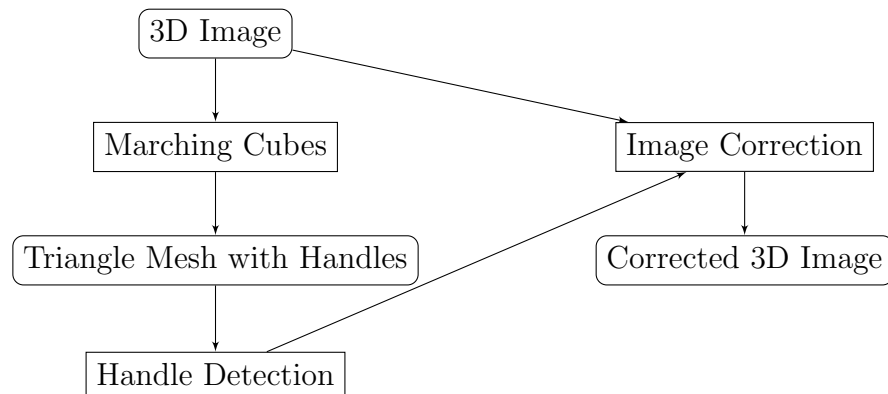
Figure 2.7: The main steps of open topology. The flowchart is adapted from[127].

Open Topology is an open-source toolkit developed upon the Visualization Toolkit (VTK)[128] for the brain isosurface correction[127]. The main steps of this method are shown in Fig. 2.7. It detects defective locations on the triangulated surface and determines if the defect is a hole or a handle. The correction is done either by filling a hole or by cutting a handle in the volumetric image. The method is fast but not robust. It is capable of finding the defected place on the surface but it has trouble figuring out whether the defect is a hole or a handle. Fig. 2.8 shows an example of a defection on the cortical surface. it is classified as a handle by open topology, while

in reality it is a small hole (circled in blue). The potential miss-classification of open topology could lead to unnecessary large modifications on the data. As shown in Fig. 2.8, Open Topology tends to cut the big handle near the hole in blue, instead of filling the hole.
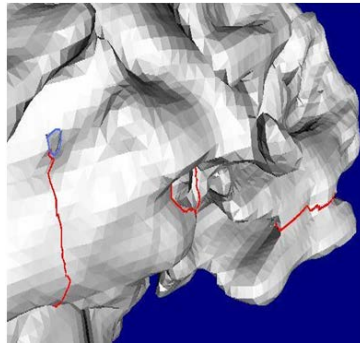
Figure 2.8: The defects detected by open topology on one cortical surface (circled in red).

Shattuck and Leahy[129] proposed an automated non-linear graph-based topology correction method of 3D brain segmentations (binary image). Two weighted graphs are built based on the binary image to represent the foreground and the background connectivities. The binary image is modified by flipping the foreground or background voxels. The surface generated from the binary image using graph-base topology correction will be a genus zero surface if both the foreground object and the background object are wholly connected. There are three types of connectivity of one voxel with its neighbors to define the foreground or background graph, 6-, 18-, and 26-connectivity.

6-connectivity: two voxels share a face (see Fig. 2.9a).

18-connectivity: two voxels share a face or an edge (see Fig. 2.9b).

26-connectivity: two voxels share a face or an edge or a corner (see Fig. 2.9c).

(a)   (b)   (c)
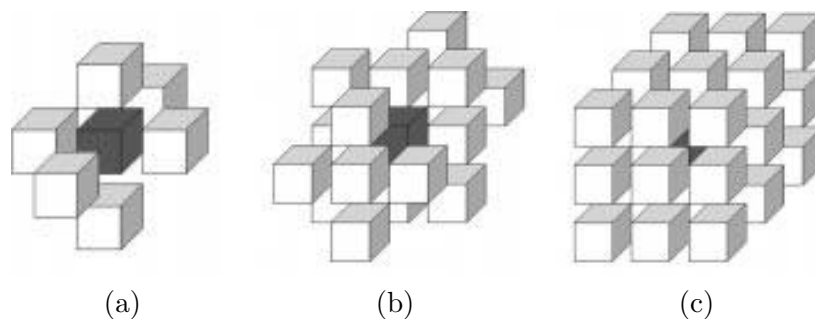
Figure 2.9: Types of the connectivity of a voxel (shaded) with its neighbors.

In Shattuck and Leahy's approach, the 6-connectivity and 18-connectivity are used to analyze the foreground and background respectively. The topology correction is implemented based on the conjecture that if the foreground and the background graph both are trees (with no cycles), the object surface generated at the boundary of the foreground and the background is genus zero. Han et al. improved Shattuch and Leahy's method using a morphology opening operation to build the graph[130]. However, both of the approaches are proposed to correct the binary image of white matter segmentation, in which most of the defects can be corrected by modifying less than 10 voxels. When we applied this approach to correct the topology of the inner surface (at the boundary of the white matter and the gray matter), it became very

slow and unable to remove all of the defects on the surface.

The third method that was tested in this study is the genus zero image filter. It was shown to be a fast and efficient method to remove topological defects from the surface. The genus zero image filter can be download from NeuroLib, the C++ library for open and close source software projects developed by the Neuro Image Research and Analysis Laboratories of the Department of Psychiatry at the University of North Carolina. The genus zero image filter also analyzes the connectivity of the foreground and background in the brain segmentation image but the correction is operated in either the foreground or the background (not both). Users have to choose whether to "cut loops" in foreground or "patch holes" in background before running the program and it is recommended by the authors to make the decision based on which types of defects is dominant on the input surface. Cortical surfaces generated at the interface between white matter and gray matter usually exhibits more holes than handles (Fig. 2.10). Therefore, we decided to "patch holes", which means the correction is operated in the background. The program takes 3D binary segmentation images as input and produces the output image which has a wholly connected foreground with 6-connectivity and a wholly connected background with 18-connectivity.

The 3D image after "Image smoothing" in Fig. 2.3 is binarized first using the isovalue representing the expected surface. The topology correction is then performed on the 3D binary image. When it is to "patch holes", the foreground object is extracted using the biggest connected component with 6-connectivity. Next, a distance transform for each voxel in the image is calculated as the squared Euclidean distance
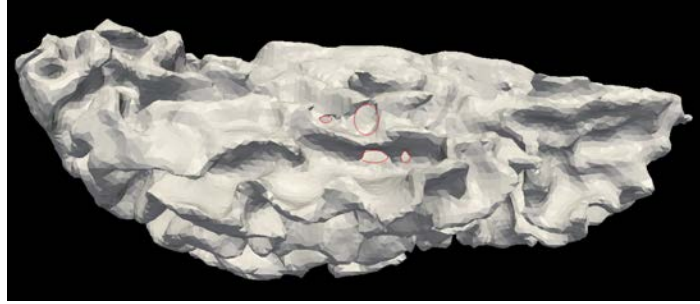
Figure 2.10: The holes found by the genus zero image filter (marked by the red circles). The surface is viewed from the inferior to the superior of the cerebral cortex, with holes located at the temporal lobe.

to the nearest object (foreground) voxel, so the distance values of object (foreground) voxels are all zeros and the distance values of background voxels are nonzeros. The topology correction is implemented in a region growing model in background starting from the voxels that are furthest (longest distance) to the object (deepest in background) and the region in process marches in a fixed step toward the object iteratively. In each iteration, the region in process includes all of the voxels which are no closer to the object at a certain distance value(level). The squared Euclidean distance between two voxels (x_1, x_2, x_3) and (y_1, y_2, y_3) is given by:

$$d(\vec{x}, \vec{y}) = d(\vec{y}, \vec{x}) = (x_1 - y_1)^2 + (x_2 - y_2)^2 + (x_3 - y_3)^2 \qquad (2.6)$$

To be more precise, the voxel size (in mm) is accounted to calculate the exact distance between these two voxels in Euclidean space:

$$d(\vec{x}, \vec{y}) = d(\vec{y}, \vec{x}) = d_1^2(x_1 - y_1)^2 + d_2^2(x_2 - y_2)^2 + d_3^2(x_3 - y_3)^2 \qquad (2.7)$$

where d_1, d_2, and d_3 are the voxel size along the corresponding axis in the 3D Euclidean space. The implementation of the distance transform can be decomposed into three

1D transformation[131]. Specifically, in our case, the distance transform for each 3D image is calculated along z axis first and then updated along y axis and x axis in each slice.
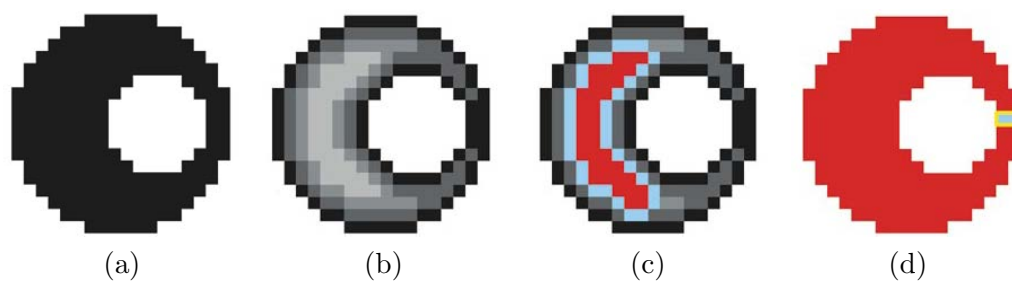
Figure 2.11: The ring that could exist in a 2D binary image. (a) A 2D binary image with the ring in background. (b) The distance transform from the background to the foreground. (c) The region growing (red) starts from the furthest region in background calculated by distance transform. (d) The final result of the region growing which left out the thinnest part of the ring to "patch the hole".

Source: Kriegeskorte and Goebel's paper[132].

At each distance level, the local connectivity (18-connectivity) is analyzed for each background voxel that has not been visited before and the connected components that have been created among visited voxels are combined optimally in the neighborhood of the current voxel. The "hole" on the surface is localized as a closed ring of background and cut at the thinnest part of the ring (Fig. 2.11), which minimizes the number of voxels needed to correct the image. "Patching holes" can be done by avoiding self-touching during the procedure of region growing in the background and the "left out" voxels in the background are then flipped to be the foreground

voxels. Self-touching (R, v) of region R growing at voxel v can be true if and only if two among 18 neighbors of v are assigned to the same connected component but not actually connected other than through v.

Table 2.1: The Result of the Genus Zero Image Filter Used in Our Study

Volume (No.)	Initial Genus	Final Genus	Pct. of Changed Voxels(%)
1	8	0	2.68
2	1	0	0.10
3	3	0	0.45
4	7	0	0.29
5	6	0	0.10
6	3	0	0.18

The results of the topological correction for 6 example surfaces are shown in Table 2.1. It shows the initial numbers of genus are all corrected to be zeros by the genus zero image filter and the percentage of changed voxels to the initial volume. As we can see, the amount of changes are pretty small. Apart from that, it takes seconds to finish the correction for one surface. Compared with Shattuck and Leahy's approach which takes hours to finish one surface, this filter is very efficient.

After the topological correction, the genus zero surface can be generated using marching cubes[133]. The surface is generated at the boundary of the foreground and the background in the 3D binary image, which is located at the inner boundary of the gray matter (gray-white transition, see Fig. 2.12). However, the surface generated by
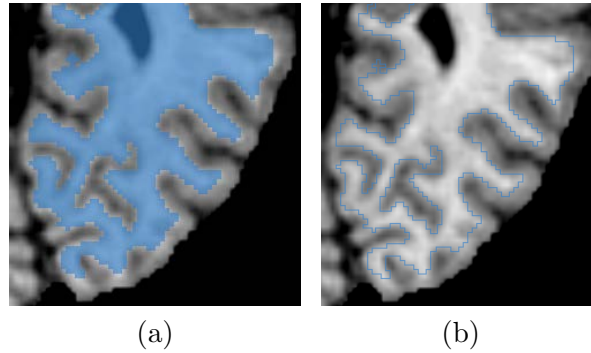
Figure 2.12: The location of the cortical surface. (a) The topologically corrected segmentation for the surface generation overlapped on a clipped tissue classified image in an axial slice. (b) The outline of the segmentation in (a) overlapped with the same axial slice.

marching cubes typically has too many triangles, which are far more than necessary to represent the cerebral cortex but just to increase the processing time for subsequent steps. Surface decimation algorithms can remove vertices, edges and triangles, while retain the surface topology. The surface decimation is also called surface simplification. Several surface decimation approaches have been proposed to cut the number of elements (vertices, edges, or triangles) on a surface, which can be classified into 3 categories – vertex clustering, resampling, and incremental decimation.

The basic idea of vertex clustering is simple[134]. The bounding regions of input surface is divided into cells with the diameter smaller than a given tolerance. Each cell is represented by a vertex and any triangle that has 2 to 3 corners can be removed and replaced by this vertex. The algorithm is fast and robust but it can easily cause topology change for the input surface. Resampling is another commonly used algorithm for surface decimation[135]. First, the input surface is represented by linear

surface geometries in piecewise. Then, the linear geometry is resampled by vertices that are less distributed. It is mostly used to build multi-resolution representations for the original surface. This algorithm does not work on highly folded surfaces like human cerebral cortex.

Incremental algorithms iteratively remove one vertex at a time. The vertex to be removed is determined by local geometric optimality criteria specified by the user. When one vertex is removed, all of the triangles that it belongs to are removed with the vertex. The hole is patched using a local triangulation. The removal repeats until a termination criterion is met. This algorithm can be implemented in different ways according to what kind of criterion is chosen to remove the vertex. Different examples of criterion variation in incremental algorithms include implementations based on distance or angle criterion, like the one in VTK[136], or implementations based on edge collapsing, etc. We have applied both of these implementations with the details and the comparison of them given below.

The VTK implementation is composed of 3 steps:

1. Classify the local vertex

2. Evaluate the decimation criteria

3. Patch the hole

Each vertex is classified into one of five classes, as shown in Fig. 2.13. The five classes are: simple, complex, boundary, interior, and corner vertex. The "simple" vertex is the one that is surrounded by a complete cycle of triangles. The "complex" vertex is the one that is surrounded by a complete cycle of triangles but it has at
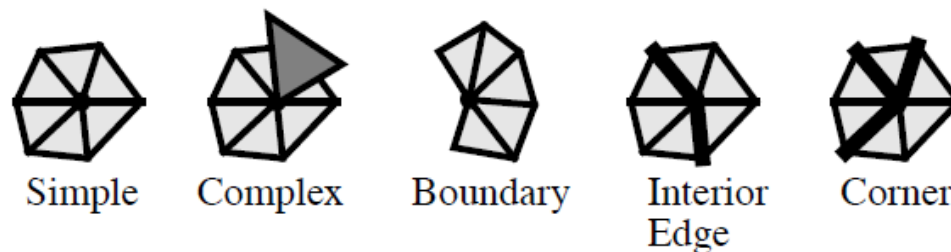
Figure 2.13: The types of surface vertices[136]. Feature edges are shown as thick lines.

least one edge that is shared by more than two triangles. The "boundary" vertex is the one that is surrounded by a semi-cycle of triangles so it has at least two edges that belong to only one triangle. The "interior" vertex has exactly two feature edges , and the "corner" vertex has more than two feature edges. A feature edge is identified when the angle between the normals of two triangles is bigger than a specific "feature angle". Simple, interior, and corner vertices are similar with each other, except that interior and corner vertices have feature edges. All kinds of vertices except the complex and the corner vertices are candidates for removal in the process of surface decimation. The complex and corner vertices are excluded because surfaces generated by marching cubes do not contain any complex vertex and the removal of corner vertices could cause unwanted change.

After each vertex is classified, it is decided to be removed or not according to its type. For a "simple" vertex, the distance from the vertex to an average plane is calculated (see Fig. 2.14a). If it is within a certain tolerance, the vertex is removed. For a "boundary" vertex or interior vertex, the distance to an edge is used as a
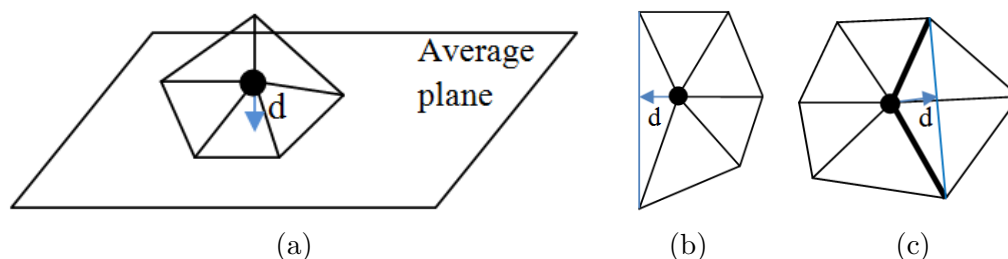
Figure 2.14: The distance calculation for the "simple", "boundary", and "interior" vertices. d in (a) shows the distance from the "simple" vertex to an average plane. (b) the distance from a "boundary" vertex (the round black point in the center) to an edge and (c) the distance from an "interior" vertex to an edge. The thickened edges are feature edges.

criterion. If the distance is smaller than a tolerance, the vertex is removed and replaced by the edge (see Fig. 2.14b and Fig. 2.14c). As outlined above, the purpose of the criteria here is to delete as many of vertices as possible while minimizing changes made to the topology of the original surface. When a vertex is removed, all of the triangles that share this vertex are removed. The hole created by vertex removal is patched by re-triangulating the surface using split planes. During decimation, the progressive meshes[137] are used in VTK implementation for transmission and updating. The decimated surface resulting from the VTK approach is shown in Fig. 2.15a. The problem of this approach is that it is very sensitive to the value of "Feature Angle", which is used to define the feature edge. An example of that is shown in Fig. 2.15. When the "Feature Angle" is increased from $35°$ to $40°$, the number of triangles on the resulting surface are reduced from $85,192$ to $32,480$. It is difficult to control the result of the decimation.
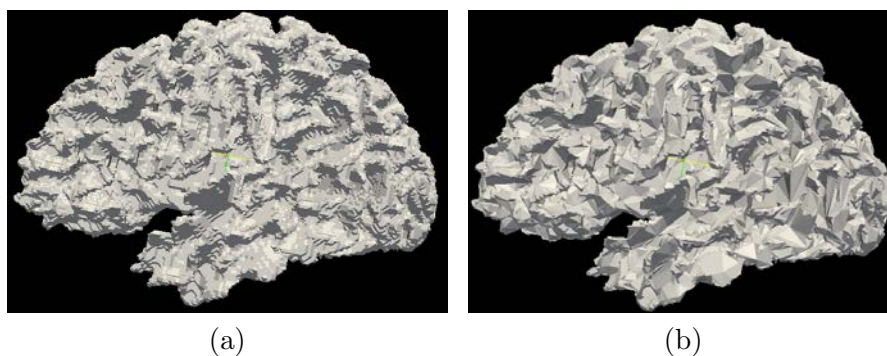
Figure 2.15: The test of the surface decimation filter in VTK. The input surface is the surface generated by marching cubes as shown in Fig. 2.17a. The parameters are set to be the same for (a) and for (b) except that the "Feature Angle" is 35° in (a) and 40° in (b). The number of triangles on the surface in (a) is 85,192 while it is 32,480 on the surface in (b).
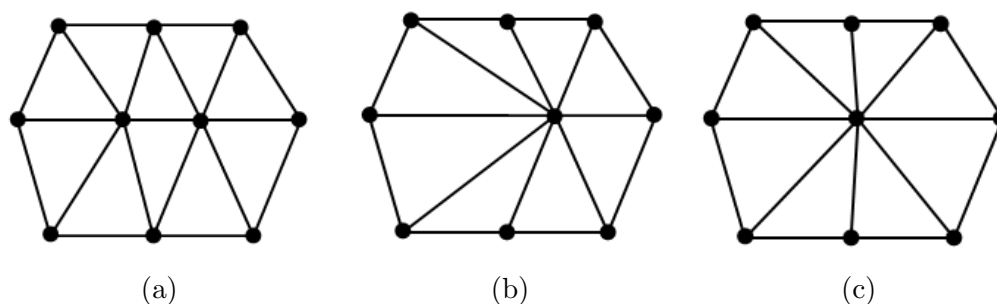
Figure 2.16: The edge collapsing during decimation. (a) The initial configuration. (b) The central edge is removed. (c) The result after relocating the remaining vertex of the removed edge.

Another incremental surface decimation method was proposed by Gelas, et al.[138]. It deals with surfaces represented by the quad edge mesh, a 2-manifold data structure in ITK[139]. This method removes vertices on a surface by collapsing its edges iteratively, as shown in Fig. 2.16. In each iteration, the shortest edge is collapsed

(a)   (b)   (c)
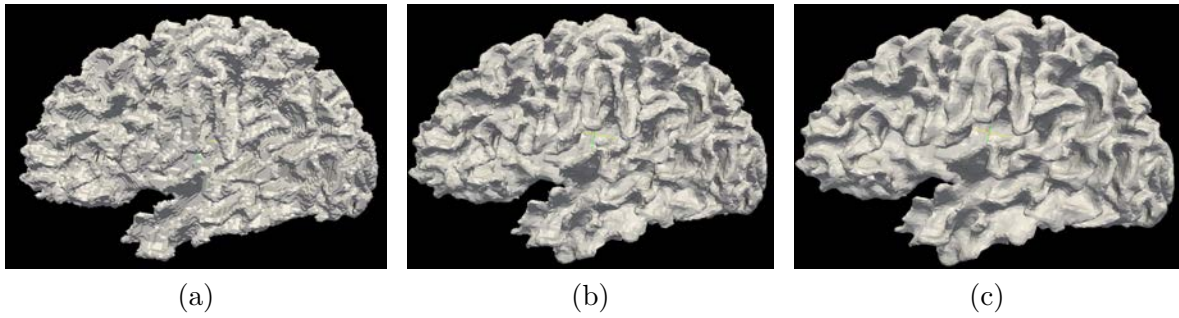
Figure 2.17: The effects of decimation and smoothing on the cortical surface. (a) The raw surface generated from marching cubes. There are 246,340 triangles and 123,172 vertices on it. (b) The decimated surface of (a) using the incremental surface decimation based on edge collapsing. The remaining number of triangles is set to be 70,000 and the remaining number of vertices is 35,002 after the surface decimation. (c) The result of surface smoothing on the decimated surface in (b). Laplacian-based smoothing method is applied with 5 iterations and the relaxation factor (λ) to be 0.1.

and the triangle that is affected by the collapsing is updated. We think this method is a better solution to decimate surfaces in our data because edges with the shortest length are guaranteed to be removed first. Triangles with extremely short edges can be problematic in the surface registration (please see details in Sec. 2.6) because their vertices could cross each other to produce flipped triangles in the process of deformation. In addition, this method has a handy feature that allows us to specify the number of triangles to remain on the resulting surface without sacrificing the topology of it. The resulting surface generated by the surface decimation is shown in Fig. 2.17b.

The last step of the surface generation process is to remove the high frequency noise from the surface and improve the appearance by applying smoothing or re-laxation filters ("Surface smoothing" in Fig. 2.3). Surface smoothing filters adjust

locations of vertices and make them more evenly distributed, so theoretically they do not affect the geometry topology of the surface. The output surface should have the same number of triangles, edges, and vertices with the input surface in this step.

The most common surface smoothing methods are based on Laplacian smoothing. The simplest version of Laplacian smoothing is to move each vertex to the average coordinate of its neighboring vertices. Neighboring vertices are those with which the center vertex shares an edge. The vertex p and its neighboring vertices $\{q_1, q_2, ..., q_n\}$ are shown in Fig. 2.18a. The calculation for updating the location of vertex p in each iteration is given below. All vertices of the surface are updated in each iteration, so more iterations will cause more smoothing on the surface.
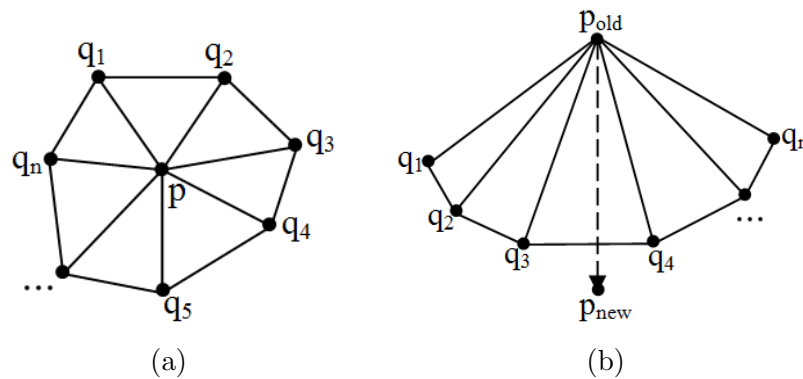
Figure 2.18: The Laplacian surface smoothing. (a) The neighbors of vertex p, $\{q_1, q_2, ..., q_n\}$. (b) A particular situation when vertex p moves out of the region defined by q_1 to q_n.

The displacement of vertex p can be calculated using coordinates of its neigh-

bors shown in Fig. 2.18a, $\{q_1, q_2, ..., q_n\}$:

$$u(p) = \frac{1}{n} \sum_i q_i - p \qquad (2.8)$$

where $u(p)$ denotes the displacement of p; p and q_i represent the current coordinates of vertex p and its neighboring vertices q_i; n is the number of neighbors for vertex p. Then, the new location of p can be calculated as:

$$p_{new} \leftarrow p_{old} + \lambda u(p_{old}) \qquad (2.9)$$

where $0 \leq \lambda \leq 1$ is the relaxation factor. A bigger value of λ causes more aggressive displacement for the vertex p. In extreme case as shown in Fig. 2.18b, aggressive displacements could produce flipping triangles, so a smaller λ is recommended in implementation to result a stable smoothing.

Eq. 2.8 and Eq. 2.9 are repeated iteratively until a certain criterion is reached. Commonly, the stop criterion is set to be the number of iterations. More iterations produce more averaging/smoothing on the surface, as shown in Fig. 2.19.

From Eq. 2.8 we can also see that the surface tends to shrink toward the centroid when the number of iterations is getting bigger. To prevent shrinking the surface, but to obtain a smooth surface, we recommend to use 5 iterations with a slightly bigger relaxation factor: $\lambda = 0.1$, as shown in Fig. 2.17c. However, the surface in Fig. 2.19b looks smoother and better than the surface in Fig. 2.17c. We then calculated the shortest edge length of both surfaces. It is 0.19 mm on the surface shown in Fig. 2.19b, and 0.32 mm on the surface shown in Fig. 2.17c. Since a very short edge could potentially cause problems in the surface registration, we prefer to

(a) (b) (c)
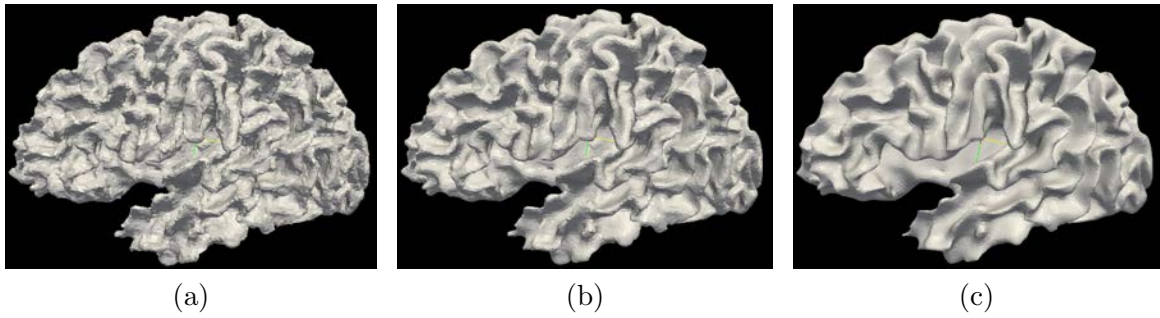
Figure 2.19: The results of the surface smoothing. The surface shown in Fig. 2.17b is smoothed with 5 iterations (a), 100 iterations (b), and 500 iterations (c). λ equals to 0.01 in all of the three cases.

use the small number of iterations with a slightly bigger relaxation factor.

2.4   Geometry Features

The cerebral cortex is a highly convoluted anatomical structure. The folding pattern defined by sulci and gyri is a complex pattern that is heterogeneous across subjects. The heterogeneity has made the automated labeling of this structure into its constituent components a challenge in the field of neuroimaging. In our study, surface registration based on diffeomorphic demons algorithm[108] is used to align two cortical surfaces together. It is a scalar value based surface registration algorithm that is similar to the intensity based image registration. It requires a scalar assignment to each vertex of surfaces to be registered. We calculated four types of scalar values based on intrinsic geometry features of the human cortical surface:

DistanceToPCIS: The Euclidean distance from the surface vertex to the PC point in the inferior-to-superior direction

DistanceToPCAP: The Euclidean distance from the surface vertex to the PC point in the anterior-to-posterior direction

DistanceToHull: The Euclidean distance from the surface vertex to a convex hull of it

MeanCurvature: The mean curvature at the surface vertex
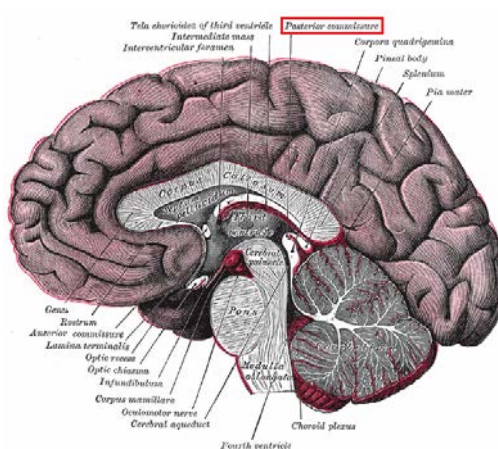
Figure 2.20: The location of the posterior commissure. It is as median sagittal section of the human brain. The "posterior commissure" is outlined in red.

Source: the book of "Henry Gray's Anatomy of the Human Body"[140].

Both of "DistanceToPCIS" and "DistanceToPCAP" are based on the location of the PC (posterior commissure) point. It is an anatomical marker, as shown in Fig. 2.20, that can be identified automatically by the BRAINS constellation detector program[115]. "DistanceToPCIS/AP", "DistanceToHull", and "MeanCurvature" represent the geometry features of a cortical surface from coarse to fine, which is

consistent with the characteristic of multi-resolution registration framework, so it is reasonable to feed those four types of geometry features into different level of resolution from coarse to fine to drive the surface registration.

<div align="center">(a)   (b)</div>
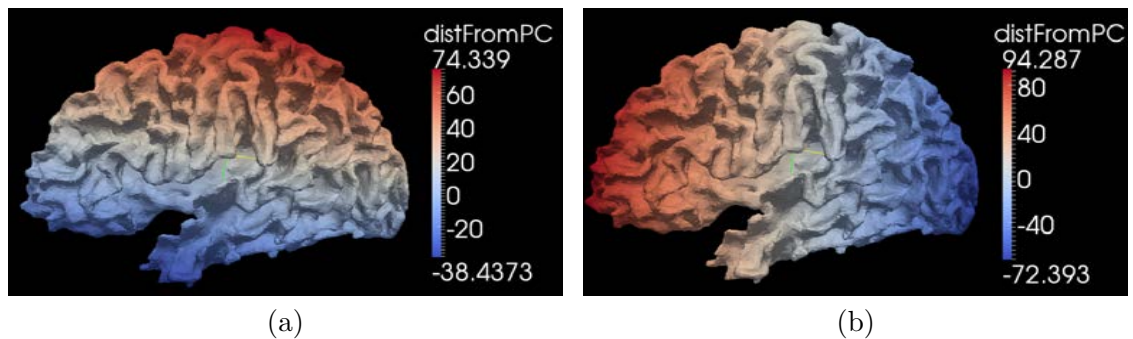
Figure 2.21: The "DistanctToPCIS/AP" on a cortical surface. The surface of the left hemisphere is shown in a lateral view. The surface vertices are associated with the signed distance values of "DistanceToPCIS (a) and "DistanceToPCAP" (b). The scalar values are colored using the legends on the right.

"DistanceToPCIS" and "DistanceToPCAP" are both signed Euclidean distances. As shown in Fig. 2.21a, the most positive value of the "DistanceToPCIS" helps us identify the superior pole of the cerebral cortex which often locates at the most superior part of the central sulcus. The most negative value of the "DistanceToPCIS" helps us to identify the tip of the temporal lobe. Likewise, the most positive and the most negative value of the "DistanceToPCAP" help us to identify the frontal and occipital poles. "DistanceToPCAP" also helps us to identify the central sulcus, since the PC point is close to the central sulcus in the anterior-posterior direction (see Fig. 2.21b).

The convex hull is generated by applying a 3D Delaunay triangulation to all of the vertices on the surface and extracting the outmost surface of it. As shown in Fig. 2.22a, the convex hull provides a shrink wrapping of the brain surface. By calculating the Euclidean distance from the surface vertex to the hull, vertices on major gyri have the values close to zero while deep sulci have larger values. The deepest regions on the surface such as insula have the largest value.

(a)   (b)
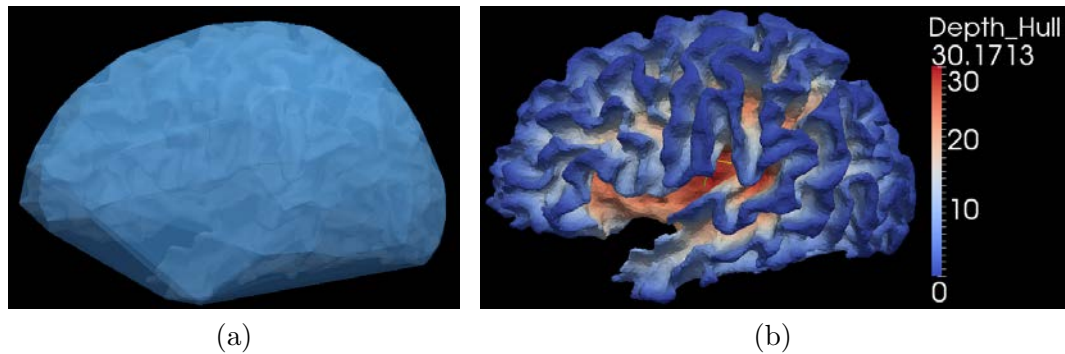
Figure 2.22: The "DistanceToHull" on a cortical surface. (a) The convex hull with the cortical surface inside of it. (b) The surface associated with the scalar values of "DistanceToHull". The color legend is shown on the right of the cortical surface.

The last type of the geometry feature is the "MeanCurvature". Curvature of a curve is the amount by which it deviates from a straight line. The curvature of a smooth curve is calculated as the reciprocal of its osculating circle at each point, as shown in Fig. 2.23a.

$$k = \frac{1}{r} \tag{2.10}$$

where r is the radius of the osculating circle at point p as shown in Fig. 2.23a and k is the curvature of the point. If the unit tangent vector at point p rotates counterclockwise, $k > 0$. If it rotates clockwise, $k < 0$.

(a)

(b)
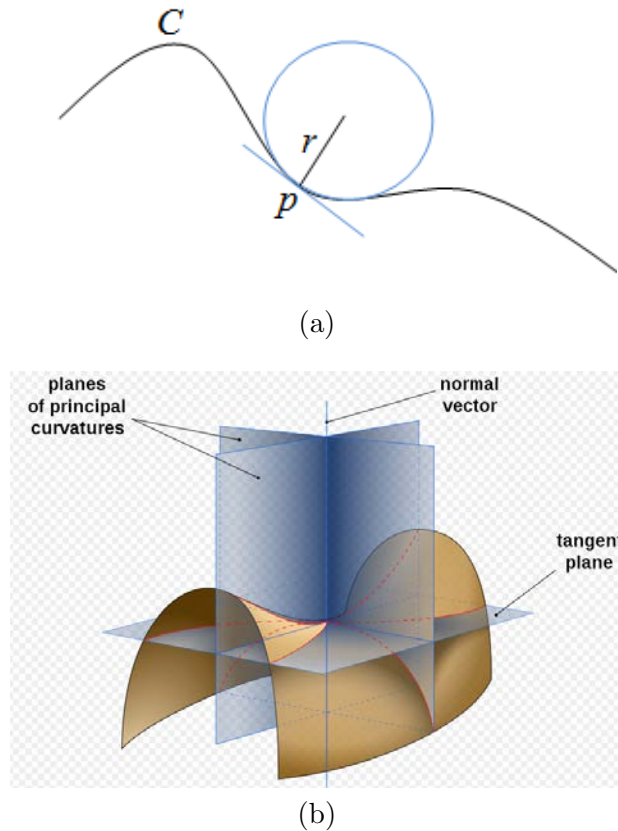
Figure 2.23: The calculation of the curvature at a point. (a) The osculating circle at point p on a curve C, where r is the radius of the circle. (b) The normal planes at the principle curvatures (adapted from the Wikimedia Commons file "File:Minimal surface curvature planes-en.svg").

For a 2-manifold surface S embedded in $\mathbb{R}^3$, curvature measures the local bending of the surface. As demonstrated in Fig. 2.23b, any plane containing the

normal vector at vertex p of the surface is called the normal plane. One normal plane intersects the surface to form one plane curve, so different normal planes have different plane curves on the surface and they all have different curvature at vertex p. The principle curvatures at p, k_1 and k_2, are the maximum and minimum curvatures among all of the plane curves. There are two kinds of calculations for curvatures of surface vertices, Gaussian Curvature and Mean Curvature. Gaussian Curvature of vertex p on a surface is the product of the principal curvatures, k_1 and k_2, $K = k_1 k_2$, so the Gaussian Curvature is positive for spheres, negative for one-sheet hyperboloids, and zero for planes. The Mean Curvature of vertex p on a surface is the mean value of the principle curvatures k_1 and k_2, $H = (k_1 + k_2)/2$.

The Gaussian Curvature determines whether a surface is locally a peak or a valley (when K is positive) or locally saddle (when K is negative). It is an intrinsic curvature which means the sign of it is independent of the embedding of the surface and it is not affected by the choice of the unit normal of the surface. The Gaussian Curvature for the vertices of our cortical surface is shown in Fig. 2.24a. As we can see, Gaussian Curvature is shown to be positive both at the local peak and local valley, so it cannot help in distinguishing the folding patterns (sulci and gyri) of the cortical surface. On the other hand, the Mean Curvature is an extrinsic curvature which means that its sign depends on the choice of the unit normal of the surface. The mean curvature gives us a smoother and more meaningful curvature evaluation in the sense of sulci and gyri patterns on the cortical surface, as shown in Fig. 2.24b. Assuming the surface normal is pointing outwards, the folding structures bending

along the direction of the normal vectors have positive Mean Curvatures (gyri), while the folding structures bending away from the direction of the normal vectors have negative Mean Curvatures (sulci).
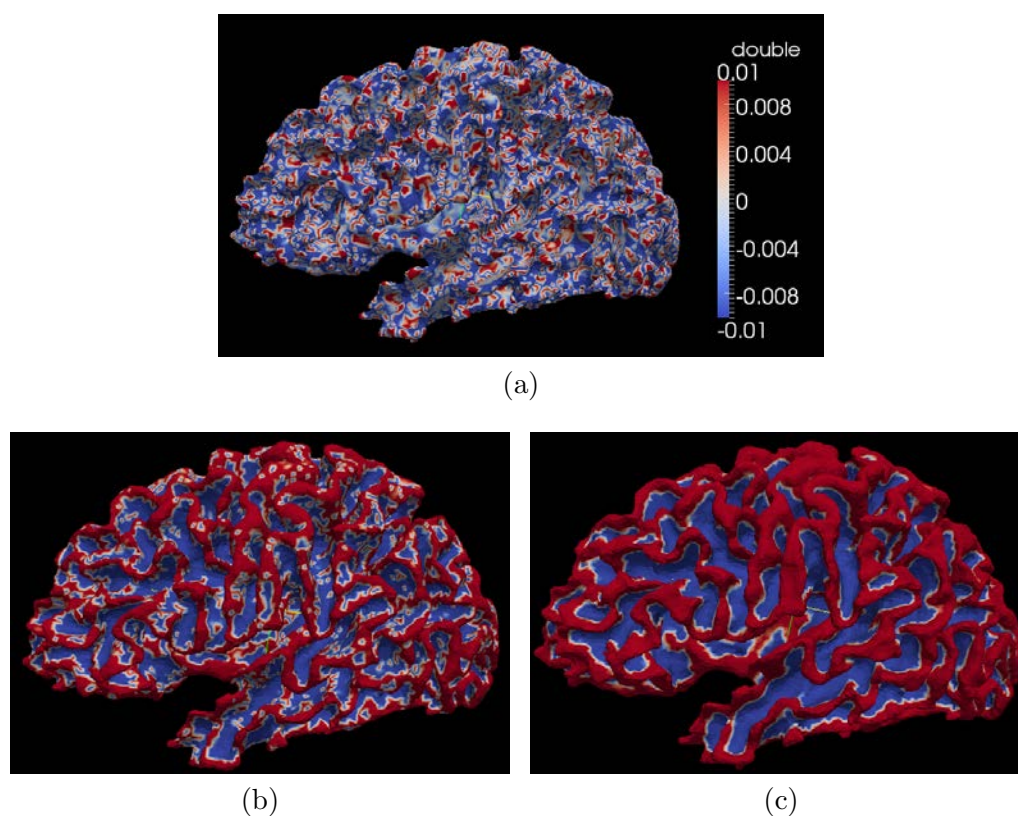
Figure 2.24: The curvatures on the cortical surface. (a) The cortical surface associated with Gaussian Curvature of vertices. (b) The "Mean Curvature" associated with the same cortical surface. (c) The smoothed "Mean Curvature" values on (b). All of the curvature values are rescaled to [-0.01,0.01] and the color legend is shown on the right side of the surface in (a).

The original "Mean Curvature" on the cortical surface shown in Fig. 2.24b is noisy. A simple scalar value smoothing method was proposed by Yeo, et al. in

his surface registration paper[141]. It was implemented with ITK by Ibanez[142]. The method smooths the scalar value at each vertex (central vertex) on the surface iteratively. A new scalar value is calculated by averaging the scalar value at the central vertex and its neighborhood. Different weights are assigned to the scalar value of the central vertex and to scalar values of its neighboring vertices, though neighboring vertices share the same weight. The weight for the central vertex is calculated using Eq. 2.11, and the neighboring vertices are weighed by the value calculated using Eq. 2.12.

$$\omega_i^0 = \frac{1}{1 + |N_i| \exp\left(-\frac{1}{2\lambda}\right)} \tag{2.11}$$

$$\omega_i^n = \frac{\exp\left(-\frac{1}{2\lambda}\right)}{1 + |N_i| \exp\left(-\frac{1}{2\lambda}\right)} \tag{2.12}$$

where ω_i^0 is the weight for the center vertex; ω_i^n is the weight for its neighboring vertices; λ is a constant parameter that applies to the entire surface; N_i is the number of neighboring vertices of the ith vertex. Table 2.2 shows the weights of the central vertex and of its neighboring vertices with different values of λ. For a better illustration, Table 2.2 values are plotted in Fig. 2.25 when the λ changes its value along the x axis. As demonstrated from Table 2.2 and Fig. 2.25, the weight of the central vertex plays a dominant role when $\lambda \leq 1.0$ (subtle smoothing) and it is slowly getting close to the weights of its neighbors when λ becomes bigger (strong smoothing). The number of iterations is another parameter to control the strength of smoothness that is expected on the input surface scalars. More iterations causes more smoothing on surface scalars. The result of the smoothing on the Mean Curvature shown in Fig. 2.24b is shown in Fig. 2.24c with $\lambda = 1.0$ and 5 iterations.

Table 2.2: The Weights of the Central Vertex and Its Neighborhood

λ	Neighbor Weight	Central Weight
0.03125	0.00000	1.00000
0.06250	0.00033	0.99799
0.12500	0.01650	0.90099
0.25000	0.07469	0.55187
0.50000	0.11470	0.31179
1.00000	0.13074	0.21556
2.00000	0.13729	0.17628
4.00000	0.14019	0.15886
8.00000	0.14155	0.15068

Source: Ibanez's publication[142].
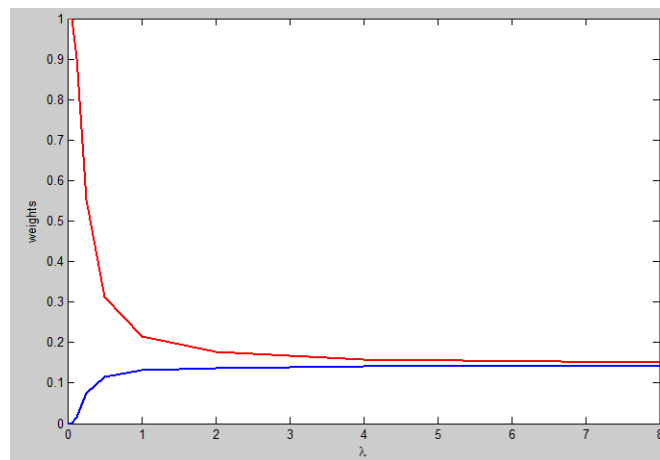
Figure 2.25: The plot of the smoothing weights, as shown in Table 2.2. The neighbor weights in the second column of Table 2.2 is plotted as the blue line and the central weights in the third column is plotted as the red line.

In summary, we calculated four types of geometry features on the cortical surface as shown together in Fig. 2.26. The cortical surface is generated from one hemisphere of a human brain. These features represent geometry characteristics of the cortical surface from coarse to fine levels. The first two, "DistanceToPCIS"

(a) DistanceToPCIS   (b) DistanceToPCAP

(c) DistanceToHull   (d) MeanCurvature
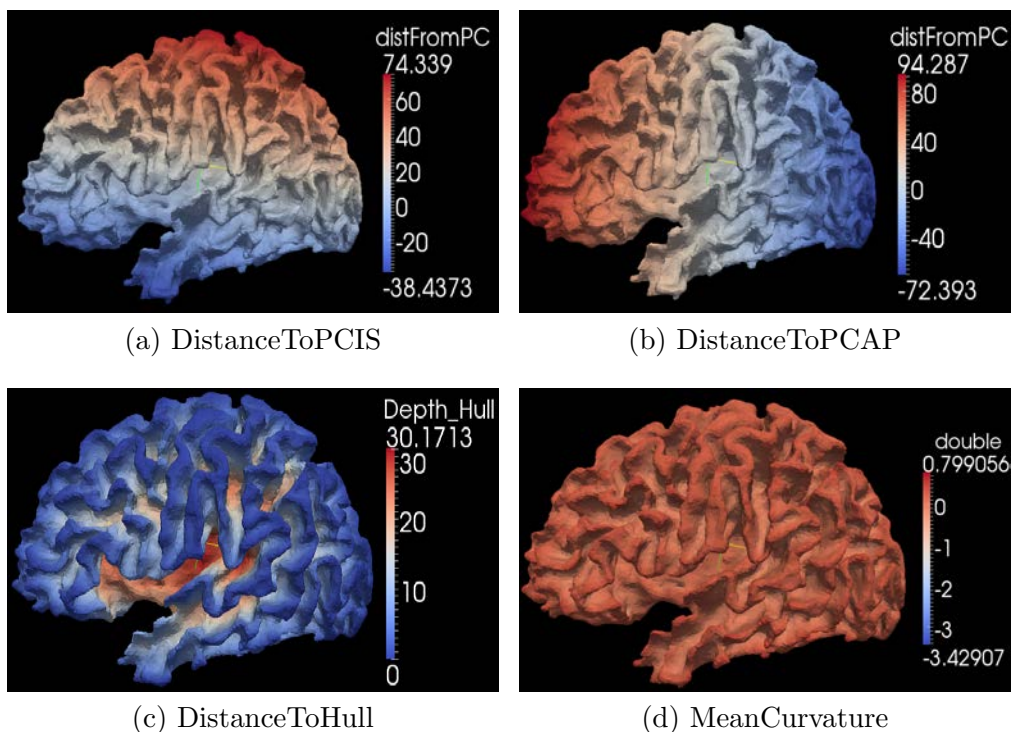
Figure 2.26: The geometry features calculated on the cortical surface. The scalar values of the geometry features are colored with the legend on the right of each surface.

and "DistanceToPCAP", contain more global information in showing polar points of the surface with extreme values, while "MeanCurvature" focuses more on local convexities, and "DistanceToHull" helps to identify overall deep fissures of the cortical surface. We did a study about the effectiveness of using these geometry features in surface registration[143], which led to the conclusion that since the geometry features have the properties of representing cortical surfaces from coarse to fine in the order of "DistanceToPCIS/AP", "DistanceToHull", and "Mean Curvature", if we apply them to the corresponding resolution levels of the multi-resolution registration, we can get better results of surface parcellation (please also see the detail in reference[143]).

2.5   Surface Flattening

Surface flattening is the concept we use to map vertices, edges, and triangles from the highly folded original cortical surface to a parametric surface, such as a complex plane or a sphere. With this technique, it is possible to register two cortical surfaces together by transforming one surface to the other in their parametric representations. Then, the labels from one surface can be propagated onto the other surface using the transformation calculated by the surface registration. For the sake of surface parcellation, the surface flattening is required to be bijective (one-to-one correspondence), so that the propagated labels on the parametric surface can be mapped back onto the original cortical surface. Another purpose of the surface flattening is to have an alternative option to visualize the brain surface, since all of the information hidden in the sulci will be exposed to the surface after it is flattened.

According to Eq. 2.5, the Euler characteristic of the genus zero cortical surface is 2, which is the same as the Euler characteristic of the spherical polyhedron. We can say that the triangulated genus zero cortical surface has the same topology as a triangulated sphere. For two surfaces with the same topology, there exists a bijective (onto and one-to-one) mapping between them[144]. We would like to use that property of the genus zero cortical surfaces generated in Sec. 2.3 to parameterize them with spherical coordinates so that the surface registration can be performed in the spherical domain.

Independent of the method applied, mapping a highly folded surface like the surface of a human cerebral cortex cortical onto a (unit) sphere always introduces

distortions at either angles of triangles or areas of them. We have tried two different approaches to flatten the genus zero cortical surface generated in our study (please see Sec. 2.3 for details). Both of the approaches try to minimize the distortion in different ways and try to guarantee that triangles do not flip in the process of surface flattening.

One of the approaches is based on the Laplace-Beltrami operator[145][146]. It is claimed to be bijective and conformal. A conformal map can preserve angles and shapes of triangles on the surface, but not necessarily the size (area) of them. The algorithm derives from differential geometry. According to the theory, a regular surface in $\mathbb{R}^3$ can be obtained by taking pieces of a plane and deforming them until smooth[147]. If $\Sigma \subset \mathbb{R}^3$ represents the cortical surface to be flattened, it is assumed that Σ is a smooth manifold. A surface in $\mathbb{R}^3$ can be represented by a function, for example, the function using Euclidean coordinates (x, y, z) as $f(x, y, z)$. Mathematically, the surface is considered to be smooth (differential) if it has derivatives of all orders at all points. Assume p is a fixed point on the surface to be flattened, and it is supposed to be mapped to the polar point of the resulting sphere. Let S^2 denote the unit sphere in $\mathbb{R}^3$ and $\mathbb{C}$ be the complex plane. The conformal mapping z can be written as $z : \Sigma \setminus \{p\} \to S^2 \setminus \{\text{north pole}\}$, where "\" means "with".

However, the Laplace-Beltrami operator based surface flattening method has some critical problems. First, the mapping is highly dependent on the selection of the polar point (cell). Angenent et al. recommend selecting the polar point (cell) from a flat area on the original surface[145]. In that case either we need an extra program to

search for the flat area on the surface or it will not be fully automated. Furthermore, a tiny shift of the location of polar cell can produce a completely different mapping onto the sphere. For example, Fig. 2.27b and Fig. 2.27c are spheres mapped from the same surface using two polar cells that are next to each other on the original surface. Second, big distortions (long and thin triangles) are found in the area close to the south polar of the resulting sphere. This may result in poor registration within this region resulting from highly variable geometric features being placed within a relatively small area on the sphere, as the triangle shown in Fig. 2.28.

(a)	(b)	(c)
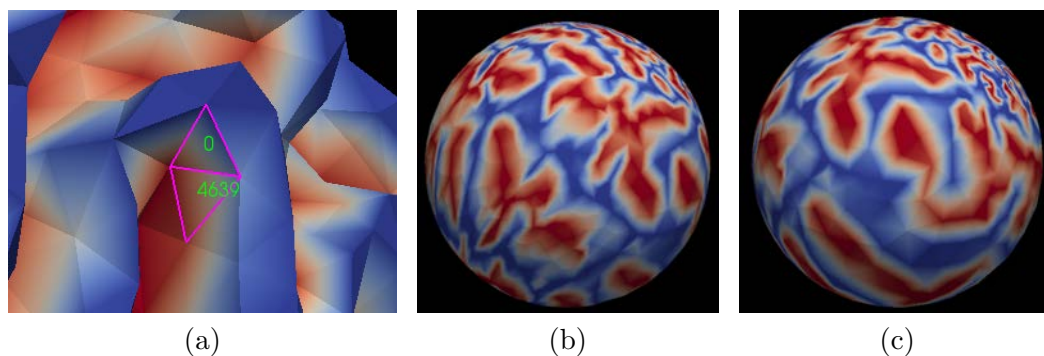
Figure 2.27: The effects of choosing the polar cell in the Laplace-Beltrami Operator Based Surface Flattening. (a) Two polar cells are outlined in purple and the numbers in green denote the cell IDs of them. (b) The resulting sphere using cell 0 as the polar cell. (c) The resulting sphere using cell 4639 as the polar cell. All of the other parameters are the same for both of the results, and the screen shots of them were taken from the same angle.

Gelas and Gouaillard[148] proposed a more general framework of the surface parameterization based on the data structure of a quad edge mesh in ITK[139]. Unlike

(a)   (b)
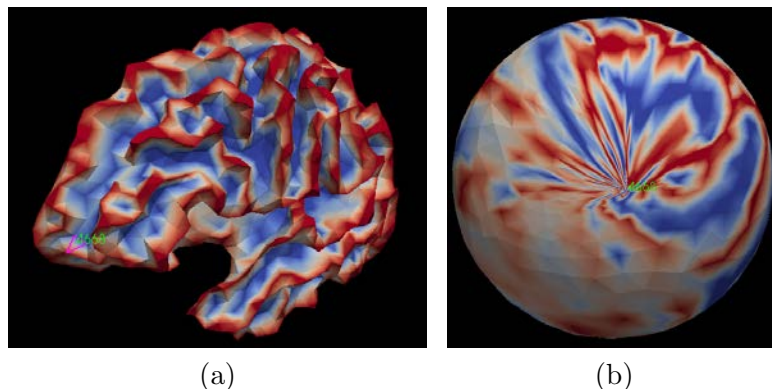
Figure 2.28: The distortion caused by the Laplace-Beltrami operator based surface flattening. (a) shows the location of cell 4668 on the input surface. It locates at the anterior part of the left hemisphere while the polar cell in this case is chosen at the posterior part of the same hemisphere. (b) shows the location of the cell 4668 on the resulting sphere. The triangle is so tiny (almost missing) because of the distortion of the surface flattening.

the Laplace-Beltrami operator based method which is derived from the assumption of a continuous function but uses the finite-element approximation to apply it on the discrete surface, the surface parameterization is proposed intrinsically for discrete surfaces. It calculates a bijective mapping between two topologically equivalent surfaces using the linear parameterization with fixed boundaries. The input surface is not limited to be genus zero. It can be a single connected surface of any genus. The flowchart of using this method to flatten a genus zero surfaces is shown in Fig. 2.29.

To deal with a surface without any boundary, a dual Fast Marching method is used first to split the original genus zero surface into two "half" surfaces with a shared boundary, as shown in Fig. 2.30. The Fast Marching method (FMM) is similar to Dijkstra's method, which is well known for finding the shortest path in a network.

```
                    ┌─────────────────────────────┐
                    │  Genus Zero Cortical Surface │
                    └─────────────────────────────┘
                                  │
                    ┌─────────────────────┐
                    │  Surface Splitting   │
                    └─────────────────────┘
```
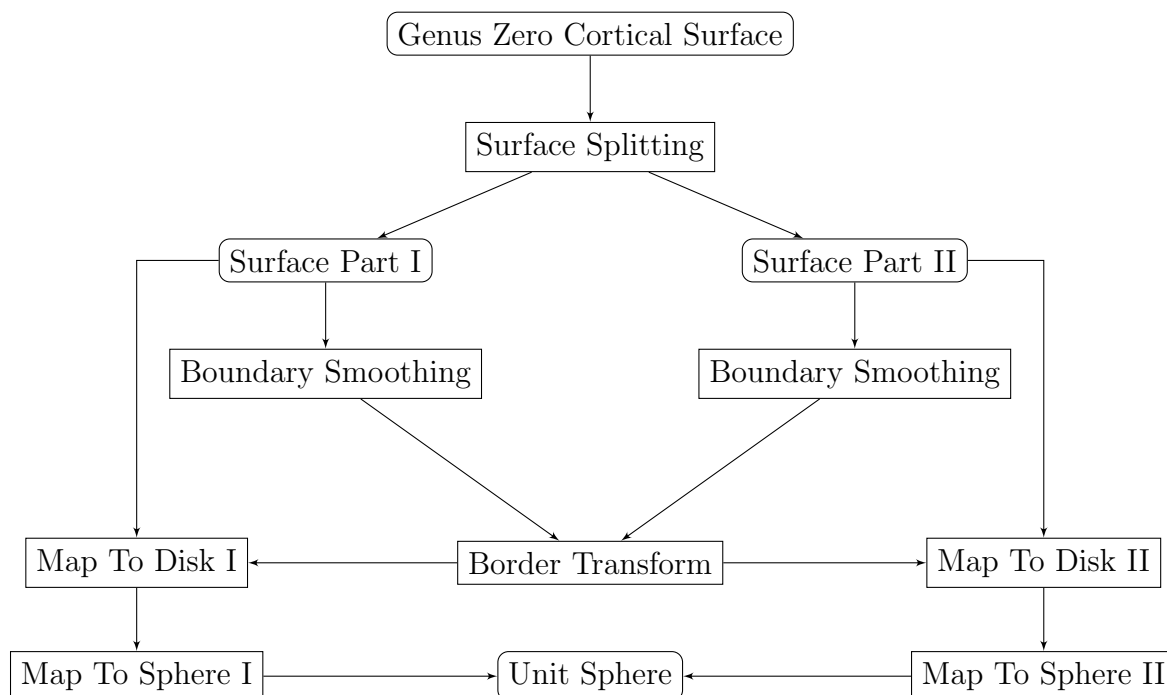
Figure 2.29: The flowchart of surface flattening. The steps of surface flattening using the linear parameterization with fixed boundaries to deal with genus zero surfaces without boundaries.

The implementation of FMM on surface splitting is to build up two clusters. Each cluster is used to keep "half" of the surface (see Fig. 2.30). The FMM goes through the original surface to classify cells of it into two clusters. The classification is based on the distance between the cell to the seed cell of the cluster. The cell is classified to one cluster if its seed cell has a shorter distance to the cell than the seed cell of the other cluster. In our study, the seed cells are chosen using the bounding box of the surface (see Fig. 2.31). In order to make them locate at similar positions among different subjects, we decided to use the cells that have points with extreme (maximum and minimum) coordinates along the "Y" axis (the anterior-posterior direction, as shown

in Fig. 2.31). Once two seed cells have been chosen, a dual FMM starts to march from them simultaneously. The distance from a cell on the surface to either of the seed is computed as the arrival time in the algorithm of FMM[149]. The minimal priority queue is used to save the shortest distance to make sure that the cell with the shortest distance on the "front" is processed (classified into one of the two clusters) first, so that an "unprocessed" cell will always be recruited into the cluster that is closer to it. As the result, all of the cells on the original surface are assigned to one of the clusters, so the whole surface is split into two "half" surfaces with a shared boundary (Fig. 2.30).

(a)   (b)   (c)
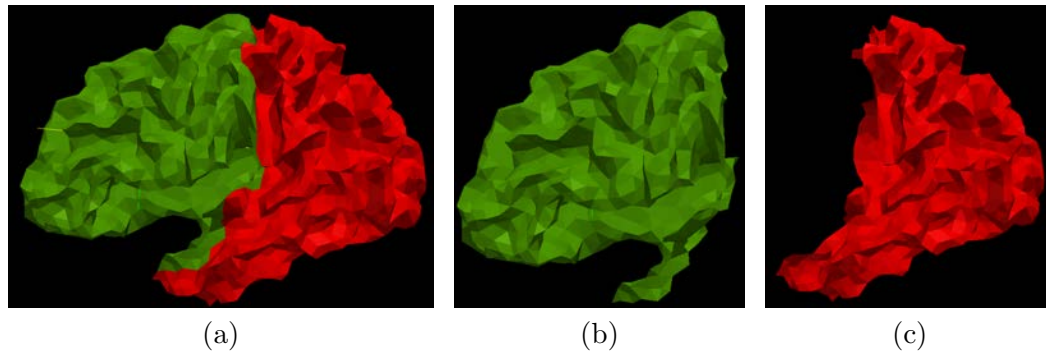
Figure 2.30:   The splitting of the genus zero cortical surface. The original surface shown in (a) can be split to two parts as shown in (b) and (c). After the splitting, both parts of the original surface share a common boundary so that the original surface equals to the sum of them.

The boundaries of two "half" surfaces are composed of edges of triangles on the border. To minimize distortions on the flattened surface, the boundaries need to be
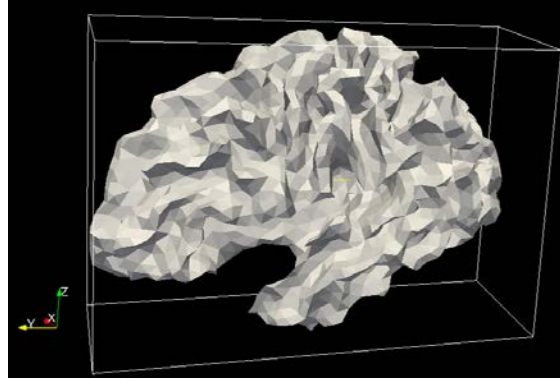
Figure 2.31: The bounding box of the surface to be flattened.

(a)   (b)   (c)
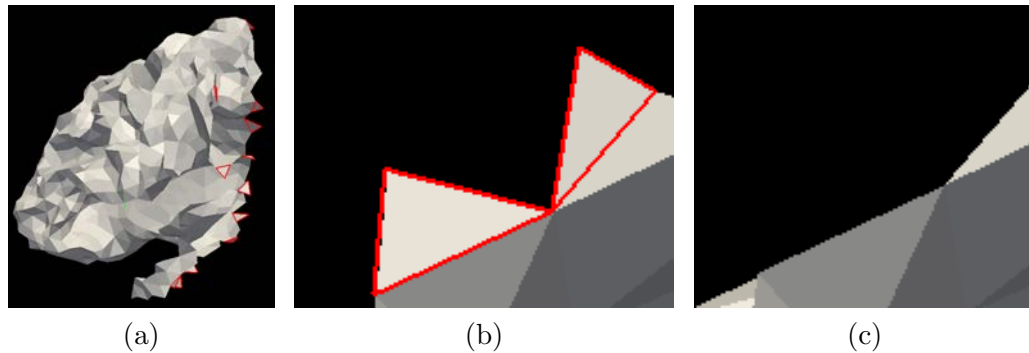
Figure 2.32: The boundary smoothing after the surface splitting. (a) shows a part of the boundary of one of the "half" surfaces with sharp shapes in red. (b) gives a closer look at some region on the boundary in (a) and (c) shows the same region after the boundary smoothing.

smoothed to remove the saw-tooth pattern on the boundary ("Boundary Smoothing" in Fig. 2.29). The smoothing process searches for any triangle that has two of its edges exposed at the boundary (as shown in Fig. 2.32a. If that kind of triangle is found, it flips the triangle to the other side of the boundary to join the other "half" of the surface. The process is performed iteratively until no such triangles can be

flipped. The result of smoothing the boundary in Fig. 2.32b is shown in Fig. 2.32c.

The linear parameterization with fixed boundaries can be seen as a spring and mass model in which each vertex of the surface is a mass and each edge of the triangles is a spring[148]. If the boundary of this triangulated surface is fixed, the interior of this spring network will relax energetically, then the parameterization of the surface can be computed by minimizing the overall spring potential energy:

$$E = \frac{1}{2} \sum_{i=1}^{N} \sum_{j \in \mathcal{N}_i} \frac{1}{2} D_{ij} \left\| \mathrm{u}_i - \mathrm{u}_j \right\|^2 \qquad (2.13)$$

where each edge of the triangle is assumed to be an ideal spring, i.e. the rest length is zero and the potential energy is $\frac{1}{2}Dl^2$, in which D is the spring constant and l is the length of the spring. $\mathrm{u}_i = (u_i, v_i)_{i=1,\ldots,N}$ is the desired parameter points for vertices and N is the number of vertices on the surface with a fixed boundary. $\mathcal{N}_i$ is the neighborhood of the vertex p_i, and $D_{ij} = D_{ji}$ is the spring constant for the edge connecting vertex p_i with p_j. $\frac{1}{2}$ appears at the beginning of Eq. 2.13 because the energy of each edge would have been counted twice without it.

To minimize E in Eq. 2.13 with a fixed boundary, we can do a partial derivative of E with respect to u_i:

$$\frac{\partial E}{\partial \mathrm{u}_i} = \sum_{j \in \mathcal{N}_i} D_{ij} \left(\mathrm{u}_i - \mathrm{u}_j \right) \qquad (2.14)$$

and then look for a u_i which makes $\frac{\partial E}{\partial \mathrm{u}_i} = 0$. We have the parameter point u_i for each interior vertex p_i, defined by its neighbors

$$\mathrm{u}_i = \sum_{j \in \mathcal{N}_i} \lambda_{ij} \mathrm{u}_j \qquad (2.15)$$

with the coefficients

$$\lambda_{ij} = D_{ij} / \sum_{j \in \mathcal{N}_i} D_{ik} \qquad (2.16)$$

The boundary vertices are not calculated using Eq. 2.15. Boundary vertices are mapped onto a circle in the parametric space, so the parameter coordinates of the boundary vertices are known and the calculation of parameter points for interior vertex u_i can be separated using interior vertices and boundary vertices in its neighborhood. Eq. 2.15 can be rewritten as:

$$u_i = \sum_{j \in \mathcal{N}, j \leq n} \lambda_{ij} u_j + \sum_{j \in \mathcal{N}, j > n} \lambda_{ij} u_j \qquad (2.17)$$

where it is assumed that there are M vertices in p_i's neighborhood and that p_j is an interior vertex when $j = 1, ..., n$ and is a boundary vertex when $j = n + 1, ..., M$.

We can see that calculation of the parameter point $u_i = (u_i, v_i)$ can be obtained by solving the linear systems

$$A \cdot U = \bar{U} \text{ and } A \cdot V = \bar{V} \qquad (2.18)$$

where $U = (u_1, ..., u_n)$ and $V = (v_1, ..., v_n)$ are the column vectors of unknown parameter coordinates for interior vertices; $\bar{U} = (\bar{u}_1, ..., \bar{u}_n)$ and $\bar{V} = (\bar{v}_1, ..., \bar{v}_n)$ are the column vectors with coefficients

$$\bar{u}_i = \sum_{j \in \mathcal{N}_i, j > n} \lambda_{ij} u_j \text{ and } \bar{v}_i = \sum_{j \in \mathcal{N}_i, j > n} \lambda_{ij} v_j \qquad (2.19)$$

And $A = (a_{ij})_{i,j=1,...,n}$ is the sparse $n \times n$ matrix with elements

$$a_{ij} = \begin{cases} 1 & \text{if } i = j, \\ -\lambda_{ij} & \text{if } j \in \mathcal{N}_i, \\ 0 & \text{otherwise.} \end{cases} \qquad (2.20)$$

There are multiple ways to set the value of spring constant D_{ij} between vertex p_i and its neighbor p_j[148], but for our study, we just chose them to be 1.0. Further, we know that if all weights (λ_{ij}) are positive and the parameter points of the boundary vertices form a convex shape, no triangles will overlap with each other after the surface parameterization, which means the mapping will be bijective[150].
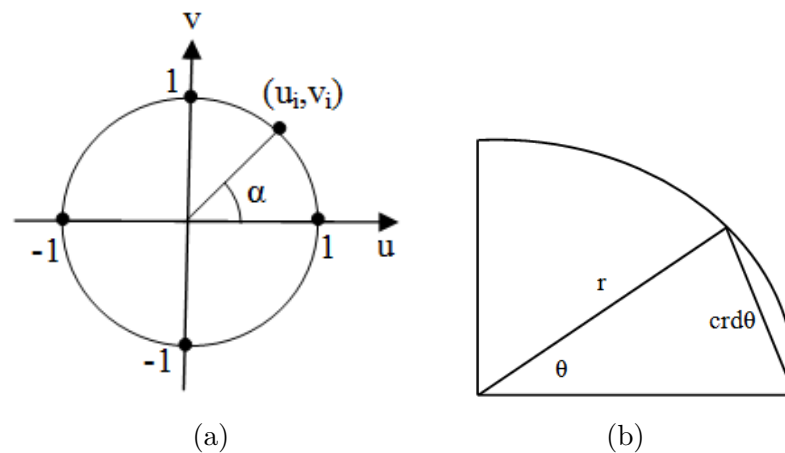
Figure 2.33: The geometries of the border transform. (a) the 2D coordinates of points on a unit circle, u_i and v_i can be calculated using the polar angle α and radius as 1.0. (b) the relationship of a chord crdθ and its angle θ in a circle with radius r. The calculation is given in Eq. 2.22.

As mentioned above, the boundary vertices need to be projected onto a circle before interior vertices are mapped, such that the right sides of linear systems in Eq. 2.18 can be determined. Because "half" surfaces shown in Fig. 2.30 share the same boundary, we only need to project the boundary once. This is the "Border Transform" step in Fig. 2.29. "Border Transform" is a method to distribute boundary

vertices around a unit circle. As shown in Fig. 2.33, the 2D coordinates of any point on a unit circle can be calculated using the polar angle α:

$$
\begin{aligned}
u_i &= cos\alpha \\
v_i &= sin\alpha
\end{aligned}
\tag{2.21}
$$

Projecting boundary vertices onto a unit circle (radius $= 1.0$) can be performed by placing each of them onto the circle using the calculated polar angle α. First, we mapped all of the edges on the boundary one by one along a big circle, as shown in Fig. 2.34a. The circle needs to be big enough to contain all of the boundary edges as its chords without overlapping. Assume the radius of the big circle is r, which is calculated as 1.5 times the maximum distance from boundary vertices to the mass center of the surface that has the boundary. Each chord of the big circle has a corresponding polar angle θ calculated by Eq. 2.22, when θ is not bigger than $\frac{\pi}{2}$. Then, each edge i is projected onto a unit circle while the ratio of its polar angle θ_i to the sum of $\sum_{i=n+1}^{M} \theta_i$ remains the same as $\sum_{i=n+1}^{M} \theta_i$ is projected to 2π in the unit circle, allowing the mapped polar angle of each boundary vertex $p_i, i = n + 1, ..., M$ on the unit circle to be calculated using Eq. 2.23. The resulting parameter points on the unit circle are illustrated in Fig. 2.34b.

$$
\text{crd}\theta = 2\sqrt{\frac{1 - cos\theta}{2}}
\tag{2.22}
$$

$$
\alpha_i = \sum_{k=n+1}^{i} \theta_k \cdot 2\pi / \sum_{k=n+1}^{M} \theta_k
\tag{2.23}
$$

where α_i is the polar angle for vertex p_i on the mapped boundary (unit circle). θ_k is the polar angle of vertex p_i's edge in the big circle with radius r.
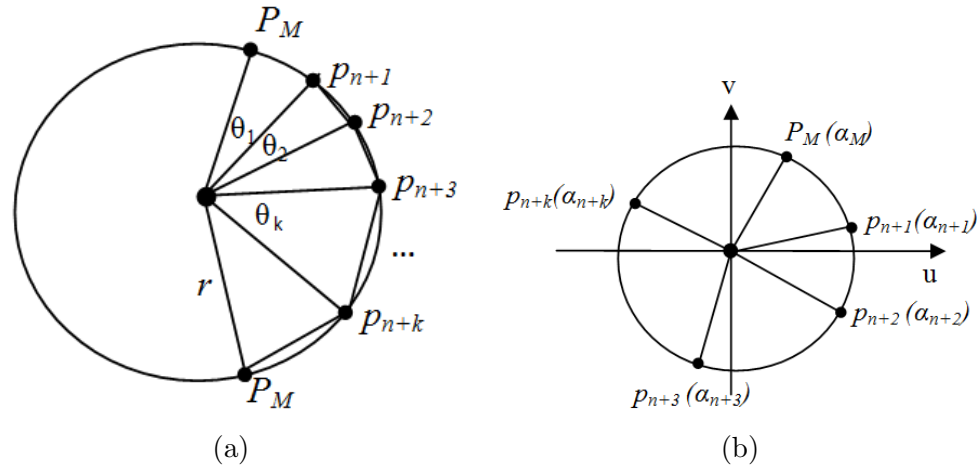
Figure 2.34: The mapping of the boundary vertices and edges. p_M is the last vertex of the boundary. It shows up twice here because the boundary is supposed to be a closed curve. θ_k is calculated using the angle and chord relationship given by Eq. 2.22.
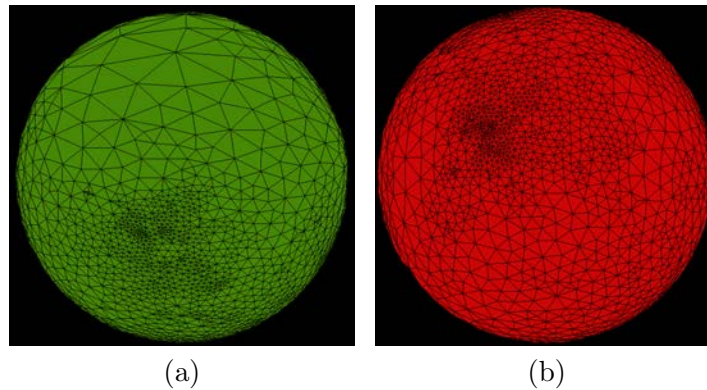
Figure 2.35: Parameterization of "half" surfaces into unit disks. (a) Unit disk mapped from the "half" surface in Fig. 2.30b. (b) Unit disk mapped from the "half" surface in Fig. 2.30c. Both of the disks share the same unit circle mapped from the boundary generated from the "Surface Splitting".

The boundary mapping method mentioned above makes sure that there is no overlapping between edges and points on the boundary after they are mapped onto the unit circle. Once the new coordinates of all of the boundary vertices are known, the

surface with the boundary can be mapped into the plane of the unit disk by solving the linear systems in Eq. 2.18. Half surfaces shown in Fig. 2.30b and Fig. 2.30c are both mapped onto an unit disk shown as Fig. 2.35a and Fig. 2.35b. Then, inverse stereographic projection is used to project each disk onto a hemisphere, as shown in Fig. 2.36a and Fig. 2.36b respectively. The formula of inverse stereographic projection for each of the disk is given as:

$$(x, y, z) = (r \cdot \frac{2u}{1 + u^2 + v^2}, r \cdot \frac{2v}{1 + u^2 + v^2}, r \cdot \frac{-1 + u^2 + v^2}{1 + u^2 + v^2}) \qquad (2.24)$$

$$(x, y, z) = (r \cdot \frac{2u}{1 + u^2 + v^2}, r \cdot \frac{2v}{1 + u^2 + v^2}, r \cdot \frac{1 - u^2 - v^2}{1 + u^2 + v^2}) \qquad (2.25)$$

where (u, v) is the 2D Cartesian coordinates of the point on the unit disk and r is the radius of the resulting sphere. (x, y, z) is the 3D Cartesian coordinates of the points after mapping. It is easy to prove that $x^2 + y^2 + z^2 = r^2$, verifying that all of the points are on a sphere with radius r. Eq. 2.24 is used to map any point (u, v) within the unit circle ($-1 \leq u \leq 1$, $-1 \leq v \leq 1$) onto a hemisphere with $-r \leq z \leq 0$, while Eq. 2.25 is used to map (u, v) onto a hemisphere with $0 \leq z \leq r$. Connecting both of the hemispheres together, we can get the surface parameterization of the original input genus zero surface (see Fig. 2.36c).

The result of mapping the same surface shown in Fig. 2.28a using the surface parameterization described above is shown in Fig. 2.37. The cortical surface is mapped onto a unit sphere shown in Fig. 2.37b. No flipping triangle is found on the resulting sphere and the procedure is fully automated with the seed cells being chosen automatically. Unlike the polar cell selection in the Laplace-Beltrami based method, the seed cell does not need to be chosen from a flat area. Since this method only maps
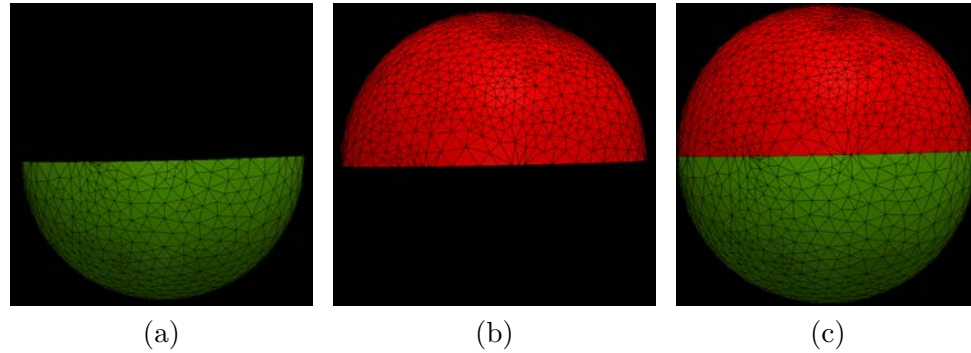
Figure 2.36: The final result of surface parameterization by connecting two hemispheres together. (a) The hemisphere mapped from the unit disk in Fig. 2.35a. (b) The hemisphere mapped from the unit disk in Fig. 2.35b. (c) The final result by simply putting (a) and (b) together.

half a hemisphere, large distortions have been avoided. However, certain amount of distortions are still unavoidable in the surface parameterization. The largest distortion in surface parameterization has been found on the cutting boundary. Boundary smoothing helps to reduce the distortion but cannot completely remove it. The resulting spheres with and without boundary smoothing are given in Fig. 2.38 just for visual comparison.

In summary, the surface parameterization method provides a better mapping from surface onto the sphere for the following reasons:

1. It does not need the user to specify the north polar cell. The user still needs to decide how to split the surface but the final result would not be affected too much as long as the seed cells in this method stays at the ends of the same axis

2. It is guaranteed that there is no flipped triangle during the flattening

3. There are less "missing" triangles (distortion shown in Fig. 2.28) caused by the
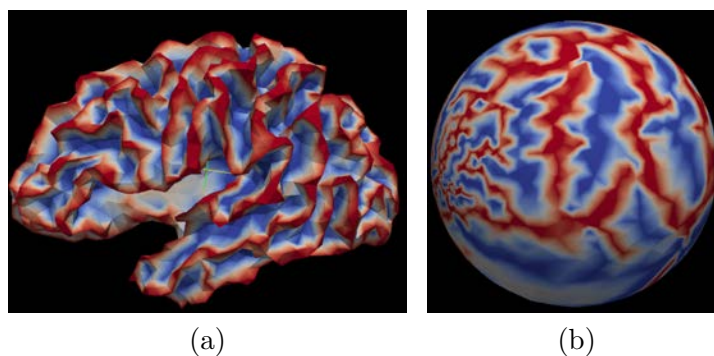
Figure 2.37: The result of surface parameterization of the genus zero surface. (a) The input surface. (b) The resulting sphere. The color associated on both of them are coded by the mean curvature.
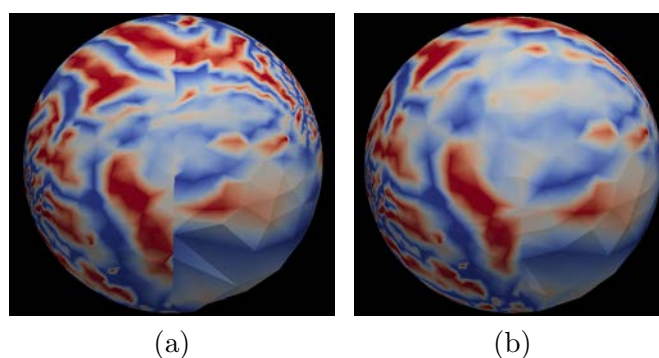
Figure 2.38: The effects of the boundary smoothing on the final mapped sphere. (a) The resulting sphere without the boundary smoothing. (b) The resulting sphere with the boundary smoothing.

surface parameterization than those caused by the Laplace-Beltrami operator based method

4. There are less amount of distortion caused by the surface parameterization method than by the the Laplace-Beltrami operator based method

However, the geometry distortion is unavoidable. It is helpful to realize where

and to what extent distortions mostly happen on the cortical surface, because the surface registration is performed only on the spherical representation of the cortical surface. We propose two metrics to analyze the areal distortion (compression and expansion) caused by the surface flattening.

(a)   (b)
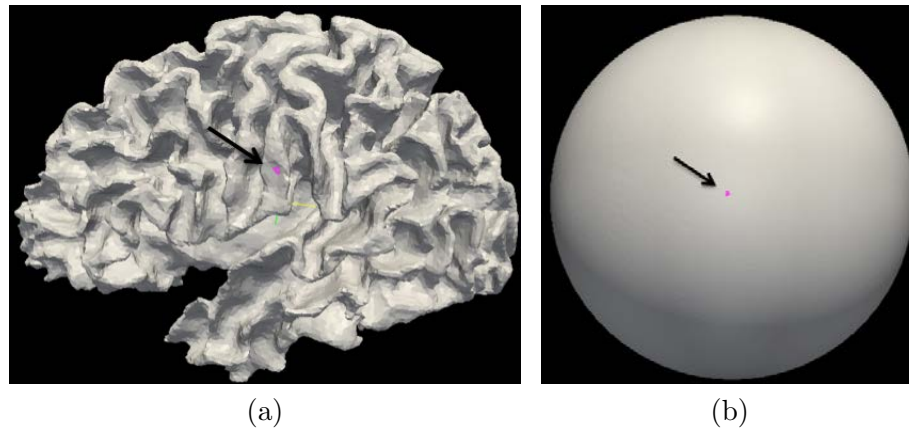
Figure 2.39: A triangle mapped from the cortical surface to a sphere. The triangle pointed by the arrow in (a) is mapped to a sphere shown in (b). The radius of the sphere is 100 mm.

The first type of areal distortion analysis is given to each triangle on the cortical surface of one subject. For each triangle on the original cortical surface, pointed with an arrow in Fig. 2.39a, it has a corresponding triangle on the sphere resulted by the surface flattening, point with an arrow in Fig. 2.39b. The areal distortion of individual triangle is calculated by:

$$D_i = \frac{A_i'/A'}{A_i/A} \tag{2.26}$$

where A_i' is the area for triangle i on the sphere; A' is the total surface area of the

sphere; A_i is the area of triangle i on the original surface; A is the total surface area of the original surface.

The other type of areal distortion analysis is to study the distortion at each parcellation label. Assume there are n parcellation labels. The average surface area of each labeled region is calculated across N testing subjects, denoted as $A_l, l \in [0, n-1]$. The ratio of the surface area of each label to all labels is calculated as:

$$R_l = \frac{A_l}{\sum_{l=0}^{n-1} A_l} \tag{2.27}$$

2.6 Spherical Surface Registration

After the genus zero cortical surface is flattened successfully, the vertices, edges and triangles on the highly folded cortical surface have been mapped onto a sphere with limited distortions. In the spherical coordinate system, surfaces are represented by 2D coordinates (θ, ϕ) when the radius r is fixed, so it is possible to match two cortical surfaces using surface registration method in the spherical domain and the deformation field can be generated having its vectors point to tangent directions. Next, the deformation field can be used to warp labels from one surface to the other to perform surface parcellation automatically. Yeo, et al. proposed the spherical demons registration method for two spherical images[141][108]. It is a fast and landmark-free surface registration method, which is extended from Diffeomorphic Demons image registration in Cartesian coordinates onto spheres. A little review of the background of Demons registration below will help us to understand better about the extended method.
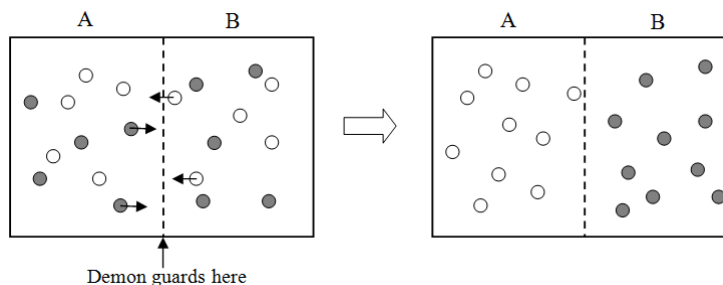
Figure 2.40: The Maxwell's demons thought experiment. The white dots represent the cold gas and the dark dots represent the hot gas.

The demons registration was first proposed by Thirion in 1998[151], inspired by Maxwell's "Demons". Maxwell first described a thought experiment in 1867 to discuss how to break the second law of thermodynamics. Assume there is a container that can be divided into two parts, A and B (see Fig. 2.40). At the beginning, both parts have the same gas in them. Among the same gas, there are faster-than-average molecules (hot gas) which move in higher velocities and slower-than-average molecules (cold gas) which move in lower velocities. Imagine a demon standing at the door between A and B. If the demon only allows hot gas to pass from A to B and cool gas to pass from B to A, in the end, A will only have the cold gas and B will only have the hot gas, which is contradictory to the second law of thermodynamics.

Thirion introduced the "demon" into the image registration. Assume we are about to register a moving image M to a fixed image F, where M is a deformable model. O is an object in F, which has a contour. A demon is situated at point P of the contour of object O. It acts locally to push M toward inside of O if the local part of M is labeled "inside", and toward outside of O if it is labeled "outside". It

is assumed here that the correspondence, as the "inside/outside" label, between M and F is known. The actual registration between M and F is implemented in an iterative scheme. The goal of the demons registration is to find a deformation field $T \in \mathcal{T}$ between the space $\mathcal{M}$ of the moving image M and the space $\mathcal{F}$ of the fixed image F. $\mathcal{T}$ is a set of possible transforms. T is updated iteratively starting from T_0 until the user specified number of iterations are finished.

There can be a group of demons guarding along the contour of object O. Demons can be selected in different ways. The simplest way is to select all of the pixels in F to be demons[152], so each image is treated as a set of iso-intensity contours. As mentioned above, T is updated iteratively by calculating the displacement for each point in F. In each iteration, the displacement can be considered as the effect of the force of each demon at point P in F. The calculation of the displacement is derived from the velocity of optical flow:

$$\vec{v} = \frac{(m - f)(\vec{\nabla} f)}{(\vec{\nabla} f)^2 + (m - f)^2} \tag{2.28}$$

where $\vec{v}$ is the velocity or displacement of P; m is the intensity of the current corresponding point of P in M; f is the intensity of P in F; $\vec{\nabla} f$ is the intensity gradient of P in F. After the current displacement is calculated (per iteration) as δT, the current deformation field T_i for the space of the fixed image F is thus updated by warping T_i with δT: $T_{i+1} = \delta T \circ T_i$. Then, a Gaussian filter is applied to smooth the deformation field of the whole image, T_{i+1}.

In general, the demons registration starts with an initial deformation T_0, which can be an identity transform or a rigid transform resulted from the previous registra-

tion. At the iteration i, the current transform T_i needs to be updated. It consists of two steps (see Fig. 2.41):

1. For each demon $P \in D_f$, compute the demons force as $\vec{v}$ in Eq. 2.28

2. Update T_i to T_{i+1} using the displacement field for all of the demons in D_f

where D_f is a group of demons in the fixed image F.
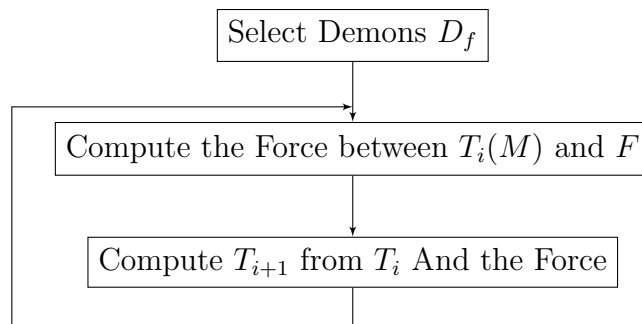
Figure 2.41: The iterations in the demons registration. Each iteration consists of two steps.

Source: adapted from Thirion's paper[152][151].

Cachier et al. described the problem of image registration mathematically using an energy function[153]. They introduced a hidden variable in the image registration: the correspondence C, which is a set of pairing between the two points. Each point P_f in the fixed image F has a corresponding point P_m in the moving image M that attracts P_f, so the correspondence of each point P in F is given by a vector in C. Thus the two steps described above can be viewed as: the first step is to search for a correspondence C between pixels in F and M, and the second step is to

search for a transformation T that approximates the correspondence obtained from the first step using any type of regularization method. Vercauteren et al. explained the method further based on Cachier's description to consider the demons registration as the minimization of a global energy function[154], which consists of two variables, the correspondence C and the transformation T:

$$E(C,T) = \frac{1}{\sigma_i^2} Sim(F, M \circ C) + \frac{1}{\sigma_x^2} dist(T,C)^2 + \frac{1}{\sigma_T^2} Reg(T) \qquad (2.29)$$

Typically $Sim(F, M \circ C) = \|F - M \circ C\|^2$ is the similarity function between the fixed image F and the warped moving image $M \circ C$, $dist(T,C) = \|C - T\|$ is the distance between the transformation T and the correspondence C, and $Reg(T) = \|\nabla T\|^2$ calculates the gradient of the transformation. Here, the correspondence C is considered as the approximate realization of transformation T. C can be calculated in step one above, while T is the desired transformation between F and M. T can be approximated by the calculation of C plus some regularizations. As for the parameters, σ_i accounts for the noise in the image intensity, σ_x accounts for the spatial uncertainty of the correspondence, and σ_T controls the amount of regularization of the transformation T, i.e. the smoothness of it.

The optimization of Eq. 2.29 can be obtained by searching over C and T alternatively in two steps. The first step is to search for a correspondence C by optimizing $\frac{1}{\sigma_i^2} Sim(F, M \circ C) + \frac{1}{\sigma_x^2} dist(T,C)^2$, with a given transformation T. The second step is to search for a transformation T to optimize $\frac{1}{\sigma_x^2} dist(T,C)^2 + \frac{1}{\sigma_T^2} Reg(T)$, with a given C. It has been shown that if $Reg(T) = \|\nabla T\|^2$, the second step can be solved by convoluting C calculated from the first step with a Gaussian kernel or

other vectorial regularization[155].

For the first step, C is calculated as adding a small deformation (displacement) field on the given transformation T, and Vercauteren et al. showed that composition is more geometrically meaningful than simple addition[151][121], so $C \leftarrow T \circ \delta T$. For a given transformation T, computing a correspondence equals to computing a small displacement field δT by minimizing

$$E_T(\delta T) = \|F - M \circ T \circ \delta T\|^2 + \frac{\sigma_i^2}{\sigma_x^2} \|\delta T\|^2 \qquad (2.30)$$

Then, Vercauteren et al. showed that Eq. 2.30 can be solved using a Taylor series expansion and the Sherman-Morrison formula[154]. They also showed that the minimization of Eq. 2.30 could be consistent with Thirion's rule by choosing a specific form of σ_i, and in that case, σ_x controls the maximum step length as: $\|\delta T(P)\| \leq \sigma_x/2$.

In his PhD thesis, Vercauteren analyzed various calculations of the demons forces that could be explained by different optimization strategies[156]. One of Vercauteren's most interesting contributions to the study of demons forces is that instead of using the intensity gradient from the fixed image only, the symmetric forces that use the intensity gradients from both of the fixed and the moving images could be linked to the efficient second-order minimization (ESM). It was also shown in the practical experiments, the symmetric forces could provide better result in the image segmentation using Demons registration[121].

However, the optimization of Eq. 2.30 in the entire space of spatial transformation does not guarantee that the transformations are invertible. From the known invertible nature of diffeomorphic transformations, Vercauteren et al. proposed the
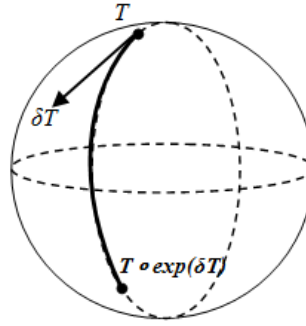
Figure 2.42: The illustration of the exponential map, as shown in Eq. 2.31. The current transformation T is in a Lie group and if the update of it is calculated on the Lie algebra, then the updated transformation shown in Eq. 2.31 remains in the same Lie group.

diffeomorphic image registration to improve the Demons algorithm[154][121]. The idea is to constrain the calculation of the optimization in Eq. 2.30 in the space of diffeomorphisms. It is implemented as a Newton iteration on a general Lie group because the inverse mapping in any Lie group should also be a differentiable map[157]. Let G be a Lie group for the composition $\circ$. Any Lie group G defines an associated real Lie algebra $\mathfrak{g}$, whose underlying vector space is the tangent space of G at the identity element Id, which is supposed to capture the local structure of the group G. In the case of real matrix groups, $\mathfrak{g}$ and G are related with an exponential map $\exp : \mathfrak{g} \to G$. The exponential map is a diffeomorphism from a neighborhood of 0 in $\mathfrak{g}$ to a neighborhood of Id in G. With an update step δT on the Lie algebra calculated by minimizing the cost function in Eq. 2.30, the current transformation T on a Lie group for the composition $\circ$ can be updated through the exponential map

(see Fig. 2.42):

$$T \leftarrow T \circ \exp(\delta T) \tag{2.31}$$

It was derived in the paper [121] that the first two terms in Eq. 2.29 can be approximated by the first order expansion for the intensity difference function $Sim(F, M \circ C) = \|F - M \circ C\|^2$ and $\|\delta T\|$ for the distance between two diffeomorphisms $dist(T, T \circ \exp(\delta T))$. Then, the energy function for the first two terms in Eq. 2.29 has the same expression as the one for the classical Demons. So, $\delta T(P)$ for a pixel P can be calculated using the same formula as the displacement field in Demons registration (Eq. 2.30), except that δT is not considered as the displacement field here, it should be considered as a speed vector field[158]:

$$\delta T(P) = -\frac{F(P) - M \circ T(P)}{\|J^P\|^2 + \frac{\sigma_i^2(P)}{\sigma_x^2}} J^{Pt} \tag{2.32}$$

where $F(P)$ is the intensity of P in the fixed image and $M \circ T(P)$ is the intensity of P in the warped moving image; $J^P = -\nabla_P^t(M \circ T)$ with a standard Taylor expansion or $J^P = -\nabla_P^t F$ with Thirion's rule, or $J^P = -\frac{1}{2}(\nabla_P^t(M \circ T) + \nabla_P^t F)$ with an EMS-like update; $\sigma_i(P)$ estimates the local image noise at P and σ_x controls the maximum step as $\|\delta T(P)\| \leq \sigma_x/2$. t represents the transpose of matrix.

As mentioned at the beginning of this section, Yeo et al. showed that the Demons algorithm can also be applied to spheres[141][108]. Let v represent the speed vector field calculated by Eq. 2.32. Instead of being an arbitrary 3D vector as it is in image registration, v can only be tangent to the sphere. Spherical Demons is similar to classical demon registration, given that both processes seek the global minimization

of the energy function as shown in Eq. 2.29 iteratively. Similarly, each iteration of Spherical Demons will be two steps.
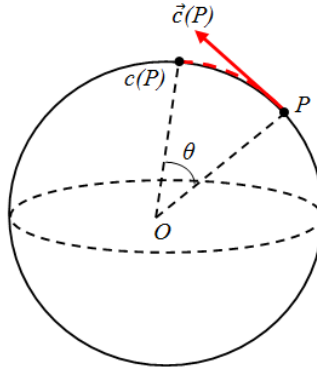
Figure 2.43: The transformation of a point on the unit sphere. Point P is mapped to $c(P)$ by correspondence C. The angle between P and $c(P)$ is θ. The tangent vector at P is pointing from P to $c(P)$.

Step one is to search for C to optimize the first two terms of Eq. 2.29, the similarity $Sim(F, M \circ C)$, and the distance between the correspondence C and the transformation T, $dist(T, C)$, using a given T. Since the transformation now only happens along the tangent vector on the sphere, both of the C and T can be represented by tangent vectors $\vec{c}$ and $\vec{t}$. A point $P \in S^2$ is mapped to point $c(P) \in S^2$ and point $t(P) \in S^2$ by transformations C and T (correspondence is also a kind of transformation). Let $T_P S^2$ be the tangent space at P and $\vec{c}(P) \in T_P S^2$ be the tangent vector at P. $\vec{c}(P)$ points along the biggest circle on the sphere which connects P and $c(P)$ (shown in Fig. 2.43). Let the length of $\vec{c}(P)$ be equal to the sine of angle between P and $c(P)$ (as θ in Fig. 2.43), then the tangent vector $\vec{c}(P)$ and the transformation

$c(P)$ have the one-to-one correspondence over $\theta \in [0, \pi)$. With this length choice, the tangent vector $\vec{c}(P)$ can be represented by vector products of point P and point $c(P)$ as:

$$\vec{c}(P) = -P \times (P \times c(P)) = -G_P^2 c(P) \tag{2.33}$$

where P and $c(P)$ are vectors starting from the center of the unit sphere, as shown in Fig. 2.43; G_P is a skew-symmetric matrix which is used to represent the cross-product of P with any vector so that $P \times c(P) = G_P c(P)$:

$$G_P = \begin{pmatrix} 0 & -P(0) & P(1) \\ P(2) & 0 & -P(0) \\ -P(1) & P(0) & 0 \end{pmatrix} \tag{2.34}$$

where $P(i), i = 0, 1, 2$ is the vector element in 3D coordinates of P.

Similarly, the transformation T can be represented by vector P and its mapped point $t(P)$. The distance between transformation C and T thus can be calculated using tangent vectors $\vec{c}$ and $\vec{t}$ defined as in Eq. 2.33 of all of the vertices $P_i, i = 0, ..., N-1$ on the sphere.

$$dist(T, C) = \sum_{i=0}^{N-1} \left\| \vec{t_i} - \vec{c_i} \right\| \tag{2.35}$$

With the choice of distance $dist(T, C)$ as in Eq. 2.35, the calculation of the speed vector field in iteration i, $\vec{v}^{(i)}$ in the first step of Spherical Demons can be

$$\vec{v}^{(i)} = \underset{\vec{v}}{argmin} \left\| \Sigma^{-1}(F - M \circ C) \right\|^2 + \frac{1}{\sigma_x^2} \sum_{j=0}^{N-1} \left\| \vec{t}_j^{(i)} - \vec{c}_j^{(i)} \right\|^2 \tag{2.36}$$

where F and $M \circ C$ are the scalar values associated with the vertices on the fixed sphere and on the warped moving sphere. They are $N \times 1$ vectors. Σ counts for the variability of a geometry feature at each vertex, which is a $N \times N$ diagonal matrix. σ_x counts for the spatial uncertainty of the correspondence.

From the diffeomorphic Demons registration, the correspondence C can be represented as the composition of T and $\exp(\vec{v})$, $T \circ \exp(\vec{v})$. And by substituting $\vec{c}_j^{(i)}$ with Eq. 2.34 and by substituting $c(P_j)$ with the composition of T and the exponential map of $\vec{v}$, Eq. 2.36 becomes

$$\vec{v}^{(i)} = \underset{\vec{v}}{argmin} \quad \sum_{j=0}^{N-1} \frac{1}{\sigma_j^2} \left(F(P_j) - M \circ \left\{ T^{(i)} \circ \exp(\vec{v}) \right\} (P_j) \right)^2$$
$$+ \frac{1}{\sigma_x^2} \sum_{j=0}^{N-1} \left\| \vec{t}_j^{(i)} + G_j^2 \left\{ T^{(i)} \circ \exp(\vec{v}) \right\} (P_j) \right\|^2 \qquad (2.37)$$

where σ_j^2 is the jth element on the diagonal of matrix Σ.

Each vector $\vec{v}$ of the tangent vector field $\vec{v}^{(i)}$ in Eq. 2.37 has to be a 3×1 vector in $\mathbb{R}^3$ tangent to the sphere at point P, so the problem in Eq. 2.37 is a constrained optimization. Yeo et al. proposed that $\vec{v}_P$ at point P on the sphere can be mapped from a tangent vector $\vec{z}_P$ at the origin of $\mathbb{R}^2$[108]

$$\vec{v}_P = \left[\vec{e}^{P1} \vec{e}^{P2} \right] \vec{z}_P = E_P \vec{z}_P \qquad (2.38)$$

where $\vec{e}^{P1}$ and $\vec{e}^{P2}$ are any two orthonormal 3×1 vectors tangent to the sphere at P; $\vec{z}_P$ is a 2×1 tangent vector at the origin of $\mathbb{R}^2$.

With Eq. 2.38, the problem in Eq. 2.37 becomes a unconstrained optimization with respect to $\left\{ \vec{z}_P^{(i)} \right\}$ for all of the vertices $\{ P_j, j = 0, ..., N-1 \}$ on the sphere at iteration i:

$$\left\{ \vec{z}_P^{(i)} \right\} = \underset{\left\{ \vec{z}_P^{(i)} \right\}}{argmin} \quad \sum_{j=0}^{N-1} \frac{1}{\sigma_j^2} \left(F(P_j) - M \circ \left\{ T^{(i)} \circ \exp(\{E_j \vec{z}_j\}) \right\} (P_j) \right)^2$$
$$+ \frac{1}{\sigma_x^2} \sum_{j=0}^{N-1} \left\| \vec{t}_j^{(i)} + G_j^2 \left\{ T^{(i)} \circ \exp\left(\{E_j \vec{z}_j\}\right) \right\} (P_j) \right\|^2 \qquad (2.39)$$

If we use $f_j(\vec{z})$ and $g_j(\vec{z})$ to represent the calculations for each point P_j in the first and the second term of Eq. 2.39, it can be written as

$$\left\{\vec{z}_j^{(i)}\right\} = \underset{\left\{\vec{z}_j^{(i)}\right\}}{argmin} \sum_{j=0}^{N-1} \frac{1}{\sigma_j^2} f_j^2(\vec{z}) + \frac{1}{\sigma_x^2} \sum_{j=0}^{N-1} \|g_j\|^2(\vec{z}) \qquad (2.40)$$

As one can see, it is a non-linear least-squares optimization problem which can be solved by the Gauss-Newton method. The $f_j(\vec{z})$ and $g_j(\vec{z})$ can be approximated by Taylor's expansions of them and reduce the non-linear least-squares optimization problem to be the linear least-squares problem:

$$\left\{\vec{z}_j^{(i)}\right\} \approx \underset{\left\{\vec{z}_j^{(i)}\right\}}{argmin} \sum_{j=0}^{N-1} \frac{1}{\sigma_j^2} \left(f_j(\vec{z}=0) + \nabla f_j \vec{z}\right)^2 + \frac{1}{\sigma_x^2} \sum_{j=0}^{N-1} \|g_j(\vec{z}=0) + \nabla g_j \vec{z}\|^2 \quad (2.41)$$

where ∇f_j is the gradient of $f_j(\vec{z})$ with respect to $\vec{z}$ at jth vertex; ∇g_j is the gradient of $g_j(\vec{z})$ with respect to $\vec{z}$ at jth vertex. The solution of this problem can give us the update at iteration i for $\vec{z}_P^{(i)}$ of each vertex independently[108]

$$\begin{aligned}
\vec{z}_P^{(i)} &= \frac{F(P) - M \circ T^{(i)}(P)}{\sigma_P^2} \\
&\cdot \left(E_P^T \left[\frac{1}{\sigma_P^2}\vec{m}_P\vec{m}_P^T + \frac{1}{\sigma_x^2}T_P(G_P^2)^T G_P^2 T_P^T\right] E_P\right)^{-1} E_P^T \vec{m}_P \qquad (2.42)
\end{aligned}$$

where $F(P)$ is the scalar value of point P on the fixed sphere; $M \circ T^{(i)}(P)$ is the scalar value of point P on the warped moving sphere; $T^{(i)}$ represents the transformation at the ith iteration. $E_P = [\vec{e}^{P1}, \vec{e}^{P2}]$ consists of two orthonormal 3×1 vectors tangent to the sphere at P; $\vec{m}_P^T$ is the 1×3 spatial gradient of the warped moving sphere $M \circ T^{(i)}$ at P; T_P^T is the 3×3 Jacobian of transformation $T^{(i)}$ at P; G_P is the skew-symmetric matrix given by Eq. 2.34; and the superscript T here means the transpose of the matrix. There are two parameters in Eq. 2.42, σ_P and σ_x. The former is actually the same as σ_j in Eq. 2.37, and the latter is the same as in Eq. 2.29.

And the speed vector at P, $\vec{v}_P^{(i)}$ can be calculated by substitute Eq. 2.42 to Eq. 2.38

$$\vec{v}_P^{(i)} = \frac{F(P) - M \circ T^{(i)}(P)}{\sigma_P^2} E_P$$
$$\cdot \left(E_P^T \left[\frac{1}{\sigma_P^2} \vec{m}_P \vec{m}_P^T + \frac{1}{\sigma_x^2} T_P (G_P^2)^T G_P^2 T_P^T \right] E_P \right)^{-1} E_P^T \vec{m}_P \qquad (2.43)$$

In reality, the Levenberg-Marquardt algorithm (Levenberg's contribution) is used to avoid the non-invertibility of the matrix $E_P^T \left[\frac{1}{\sigma_P^2} \vec{m}_P \vec{m}_P^T + \frac{1}{\sigma_x^2} T_P (G_P^2)^T G_P^2 T_P^T \right] E_P$. Levenberg's contribution is to introduce an additional term to the matrix such that Eq. 2.43 becomes

$$\vec{v}_P^{(i)} = \frac{F(P) - M \circ T^{(i)}(P)}{\sigma_P^2} E_P$$
$$\cdot \left(E_P^T \left[\frac{1}{\sigma_P^2} \vec{m}_P \vec{m}_P^T + \frac{1}{\sigma_x^2} T_P (G_P^2)^T G_P^2 T_P^T \right] E_P + \epsilon I \right)^{-1} E_P^T \vec{m}_P \quad (2.44)$$

where I is the 2×2 identity matrix and ϵ is the non-negative damping factor which is supposed to be adjusted at each iteration. The idea of adjustment for ϵ is that if the reduction of the cost function is small, ϵ can be increased, and if the reduction of the cost function is big enough, ϵ can be decreased to be a smaller value.

When we have the speed vectors $\vec{v}_P^{(i)}$ for all of the vertices on the fixed sphere at iteration i, the exponential function of the speed vector field $\vec{v}^{(i)}$, $\exp(\vec{v}^{(i)})$ can be calculated by "scaling and squaring"[158]. And the correspondence $C^{(i)}$ of iteration i is estimated as $C^{(i)} = T^{(i)} \circ \exp(\vec{v}^{(i)})$.

Step two of the Spherical Demons is to optimize the last two terms of Eq. 2.29, which are the distance between the correspondence C and the transformation T, and

the regularization with respect to transformation T using a fixed correspondence C

$$T^{(i+1)} = \underset{T}{argmin} \frac{1}{\sigma_2^x} dist\left(T, C^{(i)}\right)^2 + \frac{1}{\sigma_T^2} Reg(T) \tag{2.45}$$

where the distance function has been defined as in Eq. 2.35.

The purpose of Eq. 2.45 is to find a smooth vector field T after we get the correspondence C from step one. Yeo, et al. proposed an iterative smoothing approximation to solve Eq. 2.45. At the ith iteration, the smoothing at vertex j is to parallel transport the vectors from its neighbors and use the linear combination of them to be the new vector field for vertex j. The weights of the linear combination are calculated separately for the center vertex j and for its neighbor vertex k, which are the same as the weights used in scalar smoothing (Eq. 2.11 and Eq. 2.12). We rewrite them here just for convenience: $\omega(j, j) = \frac{1}{1+N_j \exp(-\frac{1}{2\lambda})}$ and $\omega(j, k) = \frac{\exp(-\frac{1}{2\lambda})}{1+N_j \exp(-\frac{1}{2\lambda})}$ for $j \neq k$, where N_j is the number of neighboring vertices of vertex j. The number of iterations and value of λ controls the effect of smoothing on the vector field. More iterations and larger λ produce a greater amount of smoothing. It is necessary to point out that the above approximation of the optimization in Eq. 2.45 is good on a uniformly distributed vertices of the sphere. This is one of the reasons that icosahedron resampling is performed before registration.

The summary of the Spherical Demons algorithm is given in Algorithm 2.1[108]. Normally the registration stops after fulfilling the number of iterations specified by the users, however we want to ensure the same level of global correspondence across subjects. Therefore, the sum squared distance (SSD) of scalar values in the fixed

---

Algorithm 2.1 The Spherical Demons Algorithm

Input: The fixed mesh F and the moving mesh M

Output: The deformation field C so that $M \circ C$ is close to F

Initialize $T^{(0)}$ to be an identity transformation or the transformation from a previous registration

repeat

  step 1. Given $T^{(i)}$,

    foreach vertex j **do**

      Compute $\vec{v}_P^{(j)}$ using Eq. 2.44

    end foreach

    Compute $C^{(i)}$ using "scaling and squaring"

  step 2. Given $C^{(i)}$,

    foreach vertex j **do**

      Compute $\vec{T}_j^{(i+1)}$ using the iterative smoothing

    end foreach

  until convergence

---

mesh and the warped moving mesh $\sum_{j=0}^{N-1} \left(F(P_j) - M \circ C(P_j) \right)^2$ was employed to stop the registration when the value of SSD does not change (judged by a small tolerance) for more than 5 iterations.

However, the surface registration that is used in practice is not simply to apply the algorithm of Spherical Demons directly onto the fixed and moving spheres mapped from the cortical surfaces of two human brains. It is a complex framework of scalar values normalization, mesh resampling, and rigid and non-rigid registrations. Fig. 2.46 shows the flowchart of the registration framework. Because it is used to align two cortical surfaces together, it is called as the "pair-wise surface registration framework". To use it to register two cortical surfaces together, both of the moving

surface and the fixed surface are required to carry various types of geometry features as scalar values associated with vertices on the sphere. In this study, four types of geometry features are required ("DistanceToPCIS", "DistanceToPCAP", "Distance-ToHull", and "MeanCurvature"). Please see Sec. 2.4 for details of calculating those geometry features. Since the registration is performed in the spherical domain, we assume both of the cortical surfaces to be registered can be mapped onto spheres. Please see Sec. 2.5 for details of the surface flattening in this study. Fig. 2.44 shows an example of the fixed sphere associated with geometry features and Fig. 2.45 shows an example of the moving sphere associated with geometry features. All of our cortical surfaces are mapped onto spheres with radius of 100, because with this radius, the shortest edge length on the original sphere and the shortest edge length on the highest resolution of icosahedrons meshes are similar to those on the original smoothed cortical surface. It can be realized by adding a scale value to the unit sphere generated by the surface parameterization.

The "pair-wise surface registration framework" is implemented in multi-resolution levels. The approximation of Eq. 2.45 proposed by Yeo, et al. is based on the assumption that both of the fixed and the moving spheres of the Spherical Demons have uniformly distributed vertices[108]. To provide a uniform sampling of the spheres prior to the registration, both of the fixed sphere and the moving sphere are resampled using icosahedral regular spheres with four resolution levels: IC4, IC5, IC6, IC7. IC4 represents the lowest resolution level with the smallest number of vertices and triangles, while IC7 represents the highest resolution level with largest number of
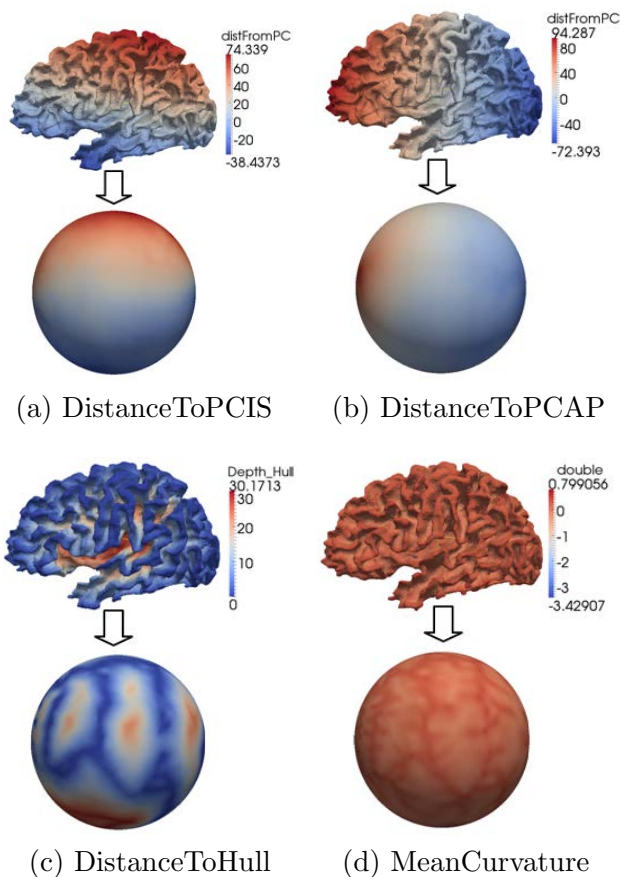
Figure 2.44: Scalar values from the cortical surface to the fixed sphere. These spheres are used as fixed spheres in the piece-wise surface registration.

vertices and triangles. In each resolution level, there has to be a type of scalar value that can drive the registration. As discussed in Sec. 2.4, the geometry features of "DistanceToPCIS/AP", "DistanceToHull", "MeanCurvature" are in the scale from coarse to fine, which is consistent with the characteristic of multi-resolution registration framework. They are used in the resolution levels that are also from coarse to fine as: "DistanceToPCIS" in IC4, "DistanceToPCAP" in IC5, "DistanceToHull" in IC6, "MeanCurvatue" in IC7.

(a) DistanceToPCIS   (b) DistanceToPCAP

(c) DistanceToHull   (d) MeanCurvature
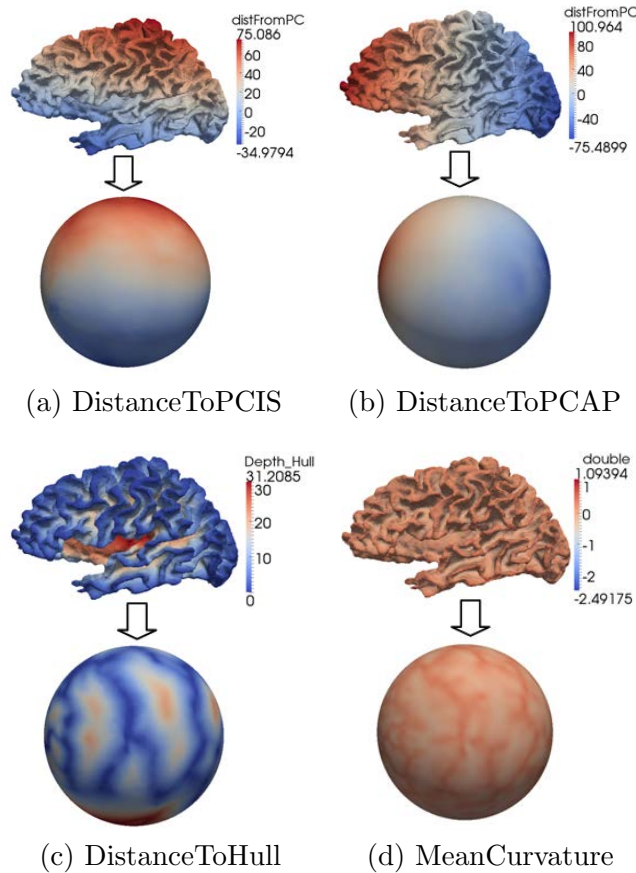
Figure 2.45: Scalar values from the cortical surface to the moving sphere. The spheres are used as the moving spheres in the surface registration.

The original icosahedron is one of the five Platonic solids. It has 20 identical equilateral triangular faces, 30 edges and 12 vertices (as shown in Fig. 2.47a). Starting from there, the regular meshes can be generated by subdividing the original icosahedron iteratively. The regular meshes used in our experiments are generated by 4, 5, 6, and 7 repeated subdivision. The number of triangles, the number of vertices, and the average edge lengths of them are given in Table 2.3. As the reference, the number of triangles on the cortical surface is 70,000; the number of vertices is 35,002;
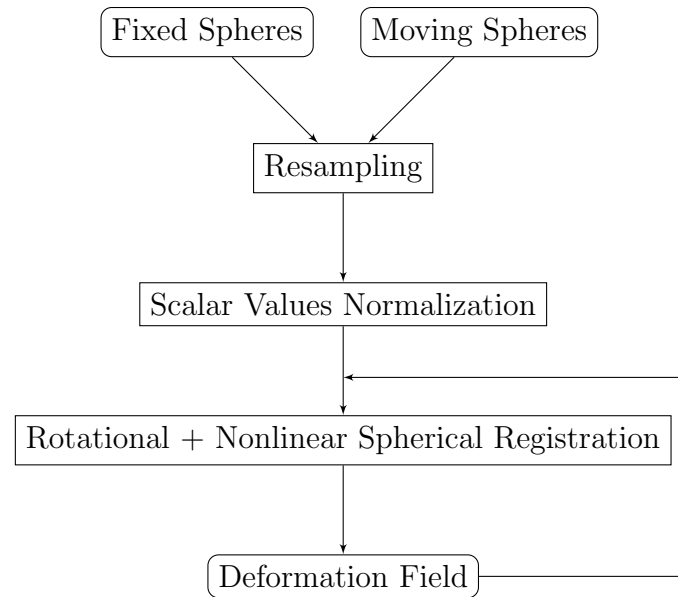
Figure 2.46: The framework of the pair-wise surface registration.

the shortest edge length is about 0.39mm.

The linear interpolation is used to assign scalar values to vertices of IC4, IC5, IC6, and IC7. For each vertex P on any regular mesh that is going to be used in pair-wise surface registration (IC7, IC6, IC5, and IC4 with radius 100.0), the triangle of the original sphere on which P is located must be found. Then, the scalar value of P is calculated by interpolating the scalar values of three triangular vertices. The key problem here is how to find this triangle. Ibanez et al. implemented it as searching for the closest points using a k-dimensional tree and then going through the triangles of all of the closest points and checking if P is "inside" of any of them or not[159]. Barycentric coordinates are used to determine whether P is "inside" of a triangle and to calculate interpolation weights for P. The idea of planar barycentric coordinates for a triangle in a plane is that the coordinates of P with respect to triangle ABC
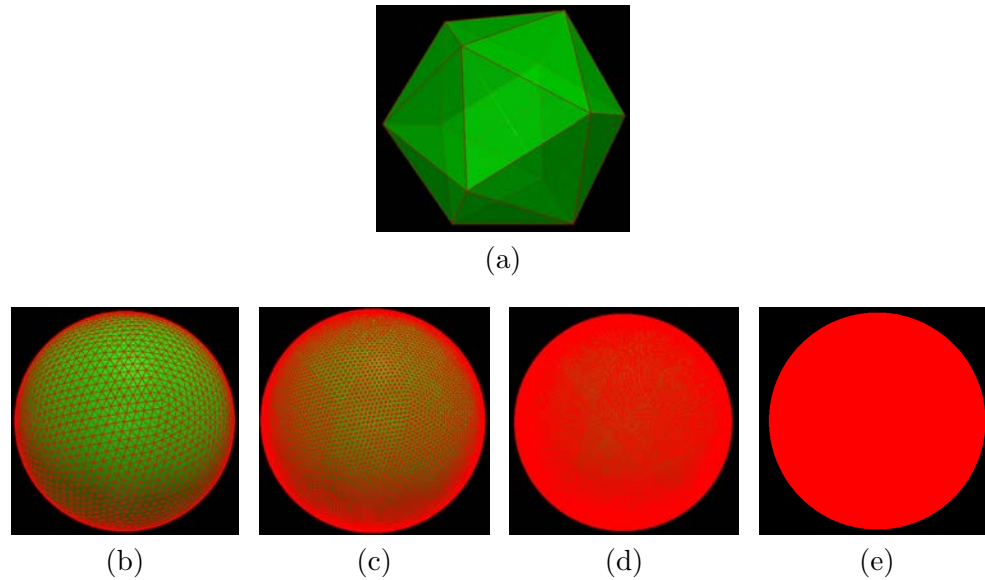
Figure 2.47: The icosahedron meshes. (a) is the original icosahedron with 20 triangles and then it can be subdivided iteratively into (b), (c), (d), and (e). The radius is 100.0mm.

(as shown in Fig. 2.48a) can be written as a weighted sum of coordinates of vertices A, B, and C as

$$\vec{P} = b_1\vec{A} + b_2\vec{B} + b_3\vec{C} \tag{2.46}$$

where b_1, b_2, b_3 are the signed area coordinates which subject to $b_1 + b_2 + b_3 = 1$. If P is "inside" of the triangle, b_1, b_2, b_3 should all be in $(0, 1)$, and if P is on an edge or a corner of the triangle, at least one of $\{b_1, b_2, b_3\}$ is zero and the rest are in $[0, 1]$. For the triangle in a plane, as shown in 2.48a, the barycentric coordinates of P can be calculated as the signed area of subtriangle PBC, PCA, and PAB divided by the area of the whole triangle ABC. 2.48b shows how we calculated the barycentric coordinates on the spherical triangle ABC. The tangent triangle $A'B'C'$ is generated in the tangent plane $(T_P S^2)$ at point P. The planar barycentric coordinates calculated

Table 2.3: The Regular Meshes Used to Resample the Original Cortical Sphere

Resolution Level	No. of Triangles	No. of Vertices	Average Edge Length (mm)
IC4	5,120	2,562	6.92
IC5	20,480	10,242	3.46
IC6	81,920	40,962	1.73
IC7	327,680	163,842	0.86

in $A'B'C'$ are used to interpolate scalar values of vertices A, B, and C to get the scalar value of P.
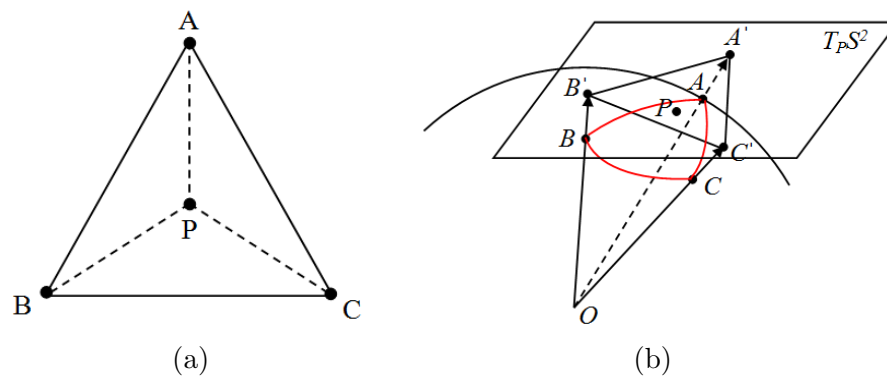
Figure 2.48: The illustration of barycentric coordinates on a plane and on a sphere. (a) The interpolation in a triangle. (b) The barycentric coordinates on the spherical triangle ABC.

Assuming there are no "large" triangles on our spheres, we constructed a triangle on the tangent plane ($T_P S^2$ in Fig. 2.48b) at P by prolonging the vertices on the sphere to the plane and use the planar barycentric coordinates calculated in the tangent triangle to approximate the spherical barycentric coordinates at P. Thus, if b_1, b_2, b_3 of the tangent triangle $A'B'C'$ are all in $[0,1]$, we would say P belongs to triangle ABC on the sphere and its scalar value can be calculated using the linear interpolation of scalar values of A, B, and C weighted by b_1, b_2, and b_3 respectively, as shown in Eq. 2.47.
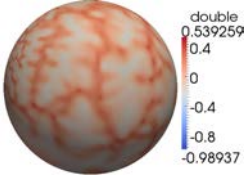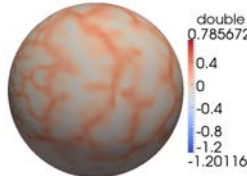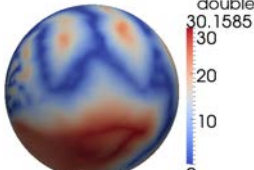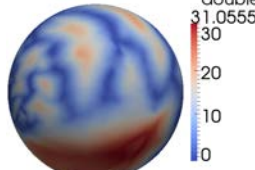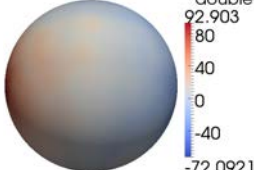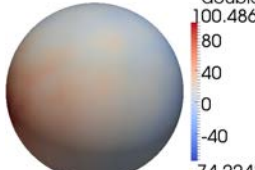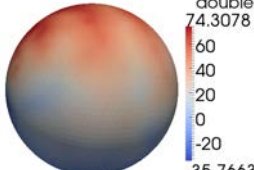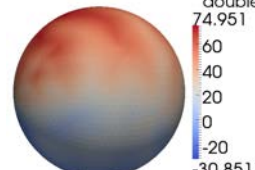
$$S_P = b_1 S_A + b_2 S_B + b_3 S_C \tag{2.47}$$

where S_A, S_B, and S_C are the scalar values of vertices A, B, and C respectively; S_P is the scalar value calculated from linear interpolation weighted by the barycentric coordinates.

Thus, the "DistanceToPCIS" of the original fixed and moving spheres (see Fig. 2.44a and Fig. 2.45a) are resampled by icosahedron IC4; the "DistanceToP-CAP" of the original fixed and moving spheres (see Fig. 2.44b and Fig. 2.45b) are resampled by icosahedron IC5; the "DistanceToHull" of the original fixed and moving spheres (see Fig. 2.44c and Fig. 2.45c) are resampled by icosahedron IC6; the "Mean-Curvature" of the original fixed and moving spheres (see Fig. 2.44d and Fig. 2.45d) are resampled by icosahedron IC7. The resampling results are given in Table 2.4.

Since the registration methods to be used to match two cortical surfaces are scalar value based method, scalar values normalization is crucial for the accuracy of the surface registration. We use different normalization strategies for the scalar

Table 2.4: The Resampled Fixed Spheres and Moving Spheres

Scalars	Resampled Fixed Spheres	Resampled Moving Spheres
MeanCurvature IC7		
DistanceToHull IC6		
DistanceToPCAP IC5		
DistanceToPCIS IC4		

values of different types of geometry features, which is summarized in Table. 2.5 and the detail of each normalization is given as the following.

The first geometry feature is the "DistanceToPCIS" (see Fig. 2.21a in Sec. 2.4). The maximum and minimum values of it vary among subjects because of the inter-subject variability of the brain size, so normalizing the distance values of "Distance-ToPCIS" can help us remove that kind of variability. We also want to keep the

Table 2.5: The Normalization of Scalar Values Before the Surface Registration

Scalars	Normalization
MeanCurvature (IC7)	Scalar Smoothing + Clamping
DistanceToHull (IC6)	Histogram Matching
DistanceToPCAP (IC5)	Piece-wise Linear Rescaling
DistanceToPCIS (IC4)	Piece-wise Linear Rescaling

anatomical meaning of the values at zero to conserve our model assumptions of the PC point at zero. Simple linear scalar rescaling lacks the capability to preserve the zero values since the original maximum and minimum values are not fixed among subjects. As shown in Fig. 2.49a, the input scalar values on the horizontal axis are mapped to [-1,1] on the vertical axis. The original zero values in two inputs are mapped to different values represented by P_0^1 and P_0^2 respectively, when the inputs do not share the same maximum ($max1$ and $max2$) and minimum ($min1$ and $min2$) values. In order to preserve the zero values of "DistanceToPCIS" during the rescaling (normalization), we use the piece-wise scalar rescaling (see Fig. 2.49b) to map the "DistanceToPCIS" into a fixed range of [-1,1]. "DistanceToPCAP" is the same kind of geometry feature which is also affected by the brain size and we also want to preserve its zero values to be where the central sulcus is located, so it is also nor-

malized by piece-wise rescaling into [-1,1]. The results of piece-wise linear rescaling of "DistanceToPCIS" and "DistanceToPCAP" on the spheres in the fourth and the fifth row of Table 2.4 are shown in Fig. 2.50.
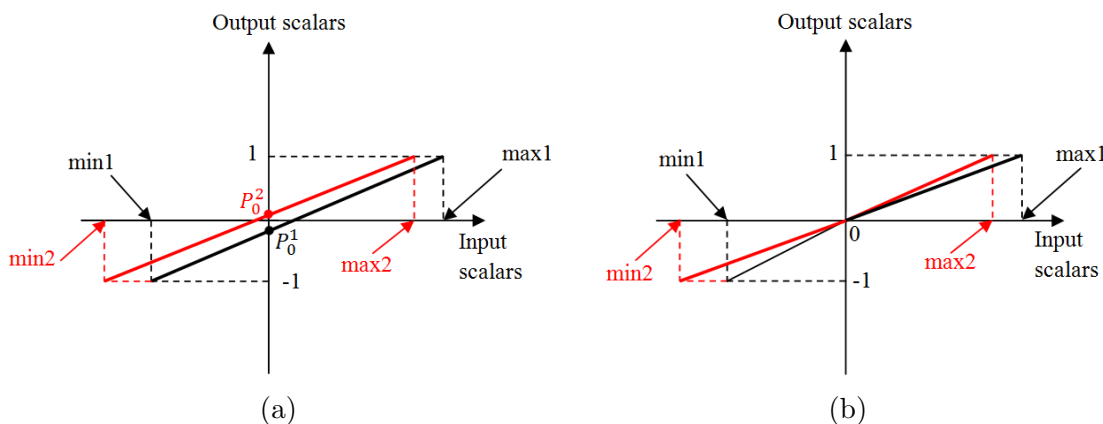
Figure 2.49: The illustration of some scalar rescaling methods. (a) The simple linear scalar rescaling. (b) The piece-wise linear scalar rescaling.

For the "DistanceToHull", we also want to match the histogram of the rescaled "DistanceToHull" on the moving sphere to the histogram of the rescaled "DistanceTo-Hull" on the fixed sphere because we believe the distributions of this kind of distance values should not vary among subjects. Histogram matching is one of the image processing techniques to change the pixel values of input image so that the histogram of it after the processing could approximate the histogram of a reference image. The basic theory and the implementation on grayscale images are shown in Gonzalez's image processing book[123].
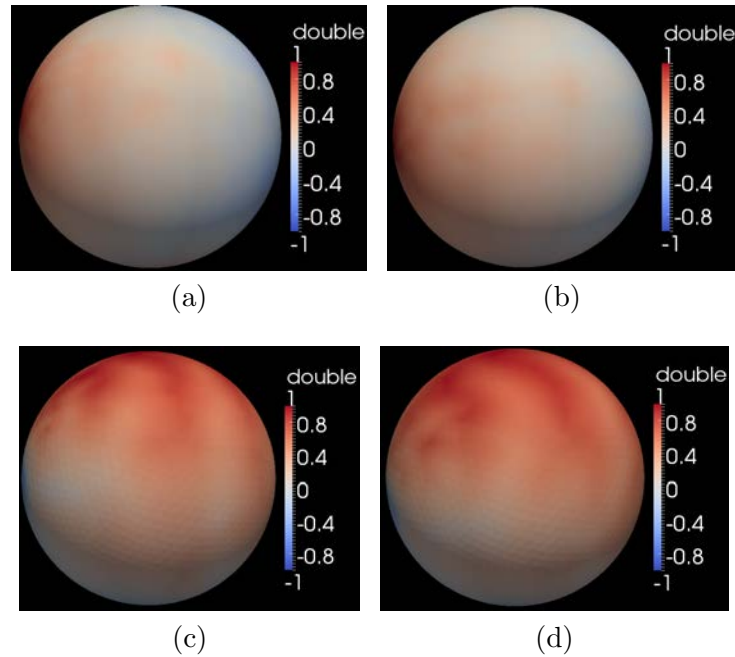
Figure 2.50: The normalization by the piece-wise linear rescaling. (a) and (b) The normalized "DistanceToPCAP" on IC5 of the fixed and the moving sphere. (c) and (d) The normalized "DistanceToPCIS" on IC4 of the fixed and the moving sphere. All of the scalar values are rescaled piece-wisely into [-1,1] and the spheres are colored by the legends on the right of them.

We extend the histogram matching to the scalar values of spheres[143]. First, the histograms of the scalar values on the input sphere (the moving sphere) and on the reference sphere (the fixed sphere) are generated by setting the number of bins (256), the maximum value (1.0) and the minimum value (0.0) between which the histogram is going to be generated, as shown in Fig. 2.51. Then, let $p_i(i)$ and $p_o(o)$ denote the continuous probability density function (PDF) of the input sphere and the output sphere (processed sphere) respectively. $p_i(i)$ can be generated from the input sphere using its scalar values. It equals to "frequency" in Fig. 2.51 divided by the
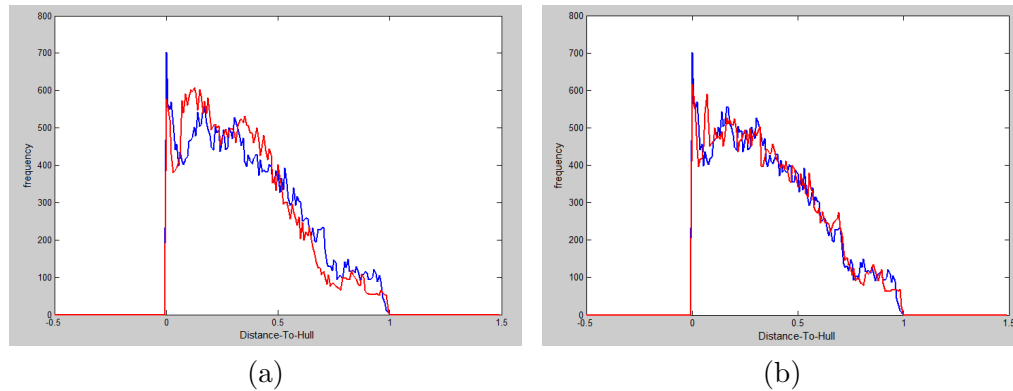
Figure 2.51: The histogram matching of the "DistanceToHull". (a) Before histogram matching. (b) After the histogram matching.

total frequency which is the total number of vertices on the sphere. $p_o(o)$ is unknown but is expected to follow the shape of the PDF of the reference sphere. Histogram matching is to find a transformation of each scalar value i to o so that $p_o(o)$ will be in a certain shape. The cumulative density function (CDF) is used to help finding such transformations. For the input sphere,

$$s = T(i) = \int_0^i p_i(w)dw \qquad (2.48)$$

where $\int_0^i p_i(w)dw$ is the CDF of the input sphere; w is the bound variable of the intergration; $T(i)$ is the transformation function at scalar value i; s is a random variable. Next, assume we can calculate the CDF of the output probability density function $p_o(o)$ as:

$$G(o) = \int_0^o p_o(t)dt = s \qquad (2.49)$$

where t is the bound variable of the integration; $G(o)$ is the transformation function

at scalar value o; and s is calculated by Eq. 2.48. So, the new scalar value of the output sphere o can be mapped from i of the input sphere as:

$$o = G^{-1}(s) = G^{-1}[T(i)] \qquad (2.50)$$

The results of histogram matching are shown in Fig. 2.51 as the change of histogram of "DistanceToHull" on the moving sphere before (Fig. 2.51a) and after (Fig. 2.51b) the matching. 2.51a shows the histograms of "DistanceToHull" on the fixed sphere (in blue) and the moving sphere (in red). 2.51b shows the histograms of the matched "DistanceToHull" on the moving sphere (in red) and the "Distance-ToHull" on the fixed sphere (in blue). The "DistanceToHull" on the fixed sphere is used as the reference of the histogram matching. As we can see, the histogram is brought closer to the one of the reference sphere (the fixed sphere) after the histogram matching.

The normalization of curvatures on the cortical surface consists of two steps. The first step is the scalar smoothing, which is demonstrated in Sec. 2.4. The second step is to further normalize the curvature value after the smoothing. As mentioned in Sec. 2.4, signs of the Mean Curvatures on the cortical surface have the meaning of recognizing the gyri and sulci, as positive for gyri and negative for sulci. If simply normalizing them into $[-1.0, 1, 0]$, it could cause the shift of curvature values so that the histogram of it is not centered at zero anymore (see Fig. 2.52).

In order to preserve the sign of curvatures, "MeanCurvatures" are simply normalized by clamping to remove extreme values. The clamping is illustrated in Fig. 2.53. Unlike rescaling, clamping does not do linear transform on the scalars. It
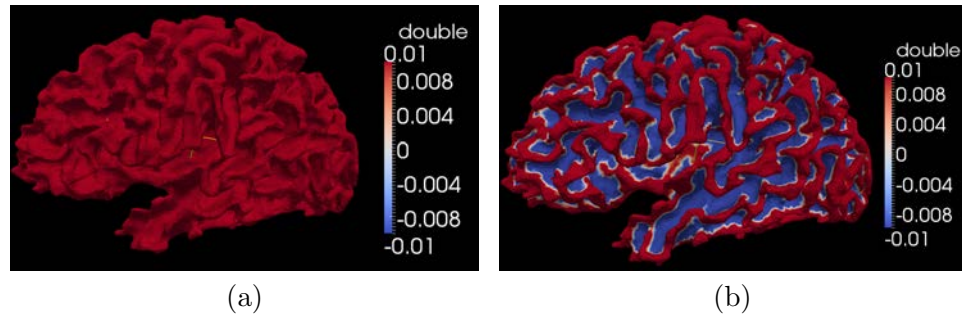
Figure 2.52: The comparison of two different ways of normalization for mean curvatures on the cortical surface. (a) Linear rescaling of mean curvatures on the cortical surface. (b) The surface with the clamped curvatures.

sets the scalar value of the input surface to be -1 if it is smaller than -1 and set it to be 1 if it is bigger than 1, and keeps the values in [-1,1] as the same on the output surface. Fig. 2.52b shows a cortical surface with the clamped curvatures.
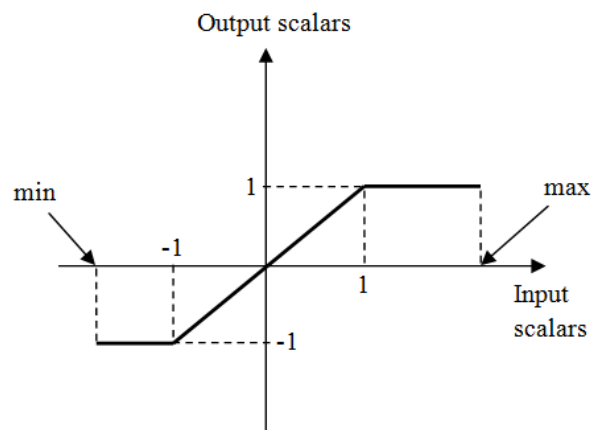
Figure 2.53: The illustration of the clamping on the input scalar values.

The linear interpolation used to resample the "MeanCurvature" by icosahe-
dron IC7 has the smoothing effects on it because the scalar value of the sample point
is the weighted average value of the vertices of the triangle that this sample point
is located in (see Eq. 2.47). It helps us smooth abnormally high curvatures with
absolute value bigger than 1.0 (see the value range of Fig. 2.44d and the resulted
range after the icosahedron resampling, first row in Table 2.4). Then, the clamped
"MeanCurvature" on the fixed and the moving spheres at resolution IC7 are shown in
Fig. 2.54. The scalar values in 2.54a does not change compared with the one shown
in Table 2.4 because they are already within [-1,1].

(a)   (b)
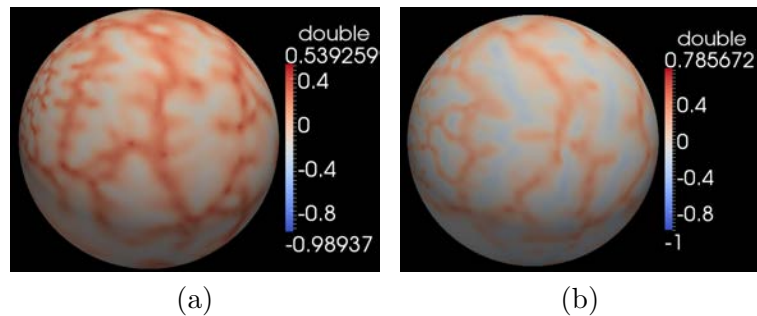
Figure 2.54: The normalized "MeanCurvature" on IC7. (a) The fixed sphere. (b)
The moving sphere. The legends on the right of the figures are used to code the colors
on the spheres with clamped scalar values.

After the normalizations, the registration can be performed to match vertices
on the fixed sphere and the moving sphere together using different geometry features
in a multi-resolution fashion, starting from the lowest resolution level, IC4. As shown

in Fig. 2.46, at each level, there is a rotational (rigid) registration followed by a spherical demons (nonrigid) registration. The deformation field from the space of the fixed sphere to the space of the moving sphere is what we expect from the whole process of registration. It is saved as a vector field on the sphere starting from zero vectors at the beginning of the process. The rotational transform obtained from the rigid transformation can be transferred as a deformation field on the fixed sphere and set as the initial deformation field to the spherical demons at the same level. Also, the deformation field from the previous level of resolution can be upsampled by the icosahedron sphere at the current level and be used as the initial deformation field for the current level and so on, until both of the rotational and the spherical demons registration at the last level of resolution is finished. The final deformation field is obtained by resampling the deformation field of IC7 with the original fixed sphere, so that the final deformation field can represent the transform from the original space of the fixed sphere to the original space of the moving sphere.

The surface registration is fully automated with a few parameters that can be used to tune the rigid and the nonrigid registrations. Table 2.6 and Table 2.7 list parameters for the rotational registration and the spherical demons registration respectively. The parameters can control the behavior of the cost function of either the rotational or the spherical demons registration. The actual values of parameters in both tables here need tremendous amount of work to decide according to the input spheres and scalar values on them, because using an inappropriate value could lead the registration into the local minima, running too many iterations to cost

Table 2.6: Parameters in Rotational Surface Registration

Name	Function	Recommended Value
Gradient Magnitude Tolerance	Stop the registration when the gradient magnitude of the cost function is smaller than this value	1e-6
Maximum Step Length	Initial step length for gradient descent optimization	0.01
Minimum Step Length	Stop the registration when the current step length is smaller than this value	1e-9
Relaxation Factor	To relax the current step length when gradient of cost function changes its direction	0.9
Number of Iterations	Maximum number of iterations to complete the registration	30

extra amount of running time, or running too few iterations where the registration has not yet converged. The recommended values in both of the tables are chosen based on evaluation of the multi-demonsional parametric space using data from our experiments. They can be changed by the user according to the data to be used.

The Versor Transform is used to apply a rotation to the space in the rotational sphere registration[159]. The mean squared distance between scalar values on the fixed sphere and scalar values on the warped moving sphere is used as the cost function. The initial step length in searching for the optimization of the cost function can be set using the "Maximum Step Length" shown in Table 2.6. The value of this

parameter is adjusted accordingly to the resolution level it is used. For example, the value of "Maximum Step Length" shown in Table 2.6 is the one used in level IC4 and the value is divided by 2, 4, 8 when it is used in level IC5, IC6, IC7. The rotational registration stops when either one of the following conditions is met. The first one is the "Minimum Step Length". If the current searching step is smaller than the value of it, the registration stops. The second condition is the "Number of Iterations". The registration stops when the number of iterations have reached the specific value.

Table 2.7: Parameters in Spherical Demons Surface Registration

Name	Function	Recommended Value
ϵ	Coefficient of the identity matrix in Eq. 2.44	$\frac{1}{\sigma_x^2}$
σ_x	Controls the maximum length of update velocity field	$\sqrt{8} \times \sqrt{\text{ShortestEdgeLength}}$
Self Regulated Mode	Adjust the value of ϵ and σ_x at each iteration when it is on	True
Minimum Metric Change	Stops the iterations when metric does not change significantly	0.05
Number of Iterations	Maximum number of iterations to complete the registration	500
λ	Controls the smoothing of deformation field	1.0
Number of Smoothing Iterations	Maximum number of iterations to smooth the deformation field	40

As for the spherical demons registration, parameters shown in Table. 2.7 are used to control the update of displacement at each vertex in each iteration, the regulation of the registration which is the smoothness of the deformation field in each iteration, and the criteria to stop the registration. There are three parameters in Eq. 2.44 that is used to calculate the update vector at each vertex on a sphere, σ_x, ϵ, and σ_P. σ_P accounts for the variability of a geometry feature at each vertex. Higher value of σ_P means the current vertex has higher variability of the geometry feature represent by the scalar value of it. We assume it is homogenous at all vertices and set the value of it to be 1. ϵ is introduced by Levenberg as a coefficient to multiply a 2×2 identity matrix. It has a negative impact on the displacement as the bigger ϵ is, the smaller the displacement will be. The value of σ_x^2 has the opposite effect as the bigger σ_x^2 is, the bigger the displacement will be. We connect them as $\epsilon = \frac{1}{\sigma_x^2}$ and require the user to only set $sigma_x$. As we can see from Eq. 2.44, the bigger value of ϵ or the smaller value of σ_x^2 would result in smaller update of the displacement. Following the advice of Yeo[108], we set the initial value of σ_x^2 at each level of resolution to be $8 \times$ shortestEdgeLength. However, in order to preserve the geometry topology of meshes (no flipping triangles) when we calculate the update for each vertex at each iteration in a certain resolution level, we have to monitor the magnitude of each updated displacement to make sure it does not cause flipping triangles. When "Self Regulated Mode" is turned on, it monitors the ratio of the magnitude of the displacement at each vertex to the shortest edge length across the sphere in each iteration. If the largest ratio among all vertices on the sphere is bigger

than 1.5, which means the biggest magnitude of the displacement calculated in this iteration is bigger than 1.5 times the shortest edge length on the sphere, it adjusts values of ϵ and σ_x^2 and reruns the iteration to lower the magnitude. Using the "Self Regulated Mode " may cause extra running time, but it is highly recommended to keep the registration process stable.

Setting the number of iterations for each resolution level could be tricky because we don't know how many iterations would be enough for the optimization to converge. We modified the implementation of Ibanez[160][161] by adding another condition to stop the registration except for the "Number of Iterations", "Minimum Metric Change". It is set to stop the iterations when the normalized metric change (see the equation below) at the current iteration is smaller than the value of "Minimum Metric Change".

$$\text{MetricChange}(i) = \text{abs}\left(\frac{\text{metric}(i) - \text{metric}(i-1)}{\text{metric}(i-1)}\right) \times 100 \qquad (2.51)$$

where metric(i) is the mean squared distance of scalar values between the fixed sphere and the warped moving sphere at the ith iteration, and metric(i) is the mean squared distance at the $(i-1)$th iteration. Once the "Minimum Metric Change" is activated, the "Number of Iterations" can be any reasonably big value, for example 500 in each resolution level, as shown in Table 2.7.

The last two parameters in Table 2.7 are for the regulation of the deformation field after updating it in each iteration. The smoothing is performed by assign the weighted average magnitude of the deformation field in the first order neighborhood of the center point. The weighted averaging is calculated independently in each

dimension but the weight is the same for all dimensions. λ is the parameter used to control weights for the center point and for its neighbors. Table. 2.2 shows the effects of λ on the scalar value smoothing but it has the same effects on the vector field smoothing. All neighbors share the same weight and neighbors here are the vertices in the first order neighborhood of the center vertex which means they share an edge with the center vertex. Bigger λ causes more smoothing on the deformation field. Another parameter for smoothing the deformation field is the "Number of Smoothing Iterations". More iterations cause more smoothing. It is set to be 10 for FreeSurfer's data[108]. We set it to be 40 and 40 for resolution level IC4 and IC5; 30 for IC6; and 20 for IC7, according to the scalar values we used for each level.

At last, the spherical demons registration requires the user to specify the sphere center as coordinates (x, y, z) and the sphere radius in millimeter (mm). It is important that all of the input spheres share the same center and radius.

2.7   Label Propagation

Once two cortical surfaces are aligned with each other using the surface registration (Sec. 2.6), labels from the moving mesh can be propagated onto the fixed mesh. An atlas with labels and geometry features is needed for the label propagation. The atlas can be a single subject chosen from the training set or the population atlas calculated from aligned subjects in the training set (see Sec. 2.8).

Fig. 2.55 shows the flowchart of steps taken in the label propagation. The atlas is registered to the subject in the spherical domain. The deformation field generated
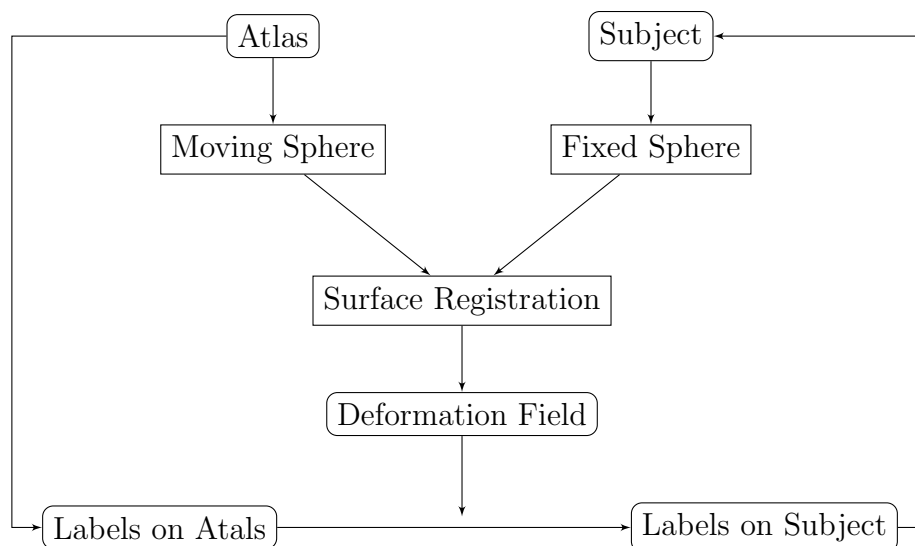
Figure 2.55: The framework of piece-wise surface registration.

from the registration is used to propagate labels from the atlas to the subject. A simple example of propagating lobar labels is shown in Fig. 2.56. A single subject is used as the atlas in the example. Labels on the atlas surface are given by mapping labels delineated by a rater in the image space to vertices on the atlas surface. The surface is parcellated into four (frontal, temporal, parietal, and occipital) brain lobes. Labels on the atlas' cortical surface (Fig. 2.56a) are mapped to corresponding vertices on its spherical representation (Fig. 2.56b).

The deformation field from the fixed (sphere) space to the moving (sphere) space is generated using the multi-resolution spherical registration mentioned in Sec. 2.6. The real deformation field generated by the multi-resolution registration is in the highest resolution level (IC7) but it can be resampled and correspond to vertices on the original fixed sphere. It is saved as a vector in the tangent plane of

each vertex on the fixed sphere, as shown in Fig. 2.56d. Using the deformation field, labels on the atlas sphere can be warped and applied to the subject sphere by the nearest-neighbor interpolation (see Fig. 2.56c), which is then mapped back onto the subject's cortical surface (see Fig. 2.56e). The subject's manual labels are shown in Fig. 2.56f for the sake of visual evaluation.

To evaluate the result, we compare the automated labels with the manual labels using similarity indices. There are two commonly used similarities indices, Dice and Jaccard. Both of them can be used to calculate the similarities of two sets of labels on cortical surfaces of our subjects. If a cortical surface is labeled both by the automated and manual labels, let A denote the surface area that is labeled as the "frontal lobe" according to the manual labels, and let B denote the surface area that is labeled as the "frontal lobe" according to the automated labels. Dice and Jaccard indices can give us a value between 0 and 1 to show how much the automated "frontal lobe" is similar with the manual "frontal lobe". The Dice index can be calculated as

$$D = \frac{2\,|A \cap B|}{|A| + |B|} \tag{2.52}$$

where D is the value of Dice index. And the Jaccard index is calculated as

$$J = \frac{|A \cap B|}{|A \cup B|} \tag{2.53}$$

where J is the value of Jaccard index.

In practice, A or B is evaluated using the surface area of polygons (triangles) of the cortical surface that is covered by a certain label. If only one point in a triangle is assigned by the certain label value, a third of the triangle's area is added up into
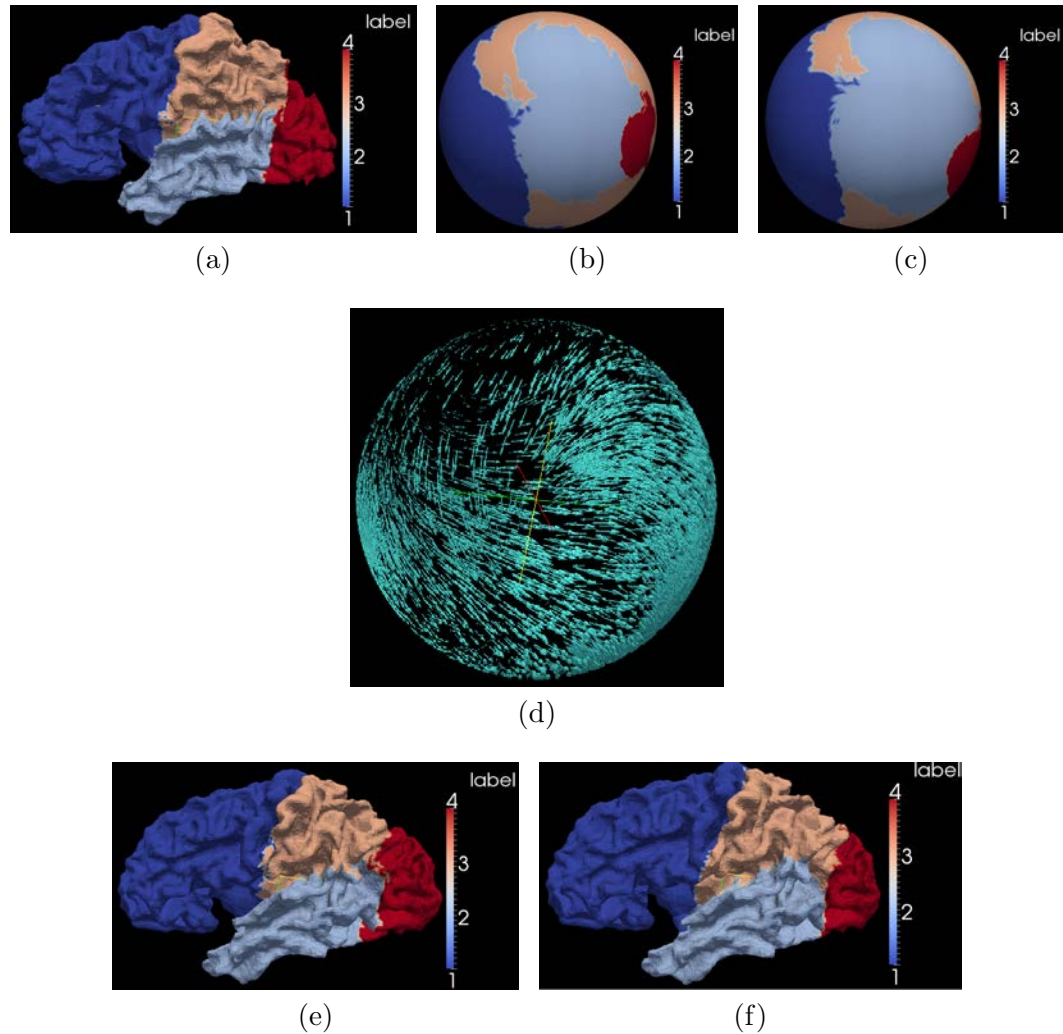
Figure 2.56: An example of label propagation. (a): Lobar labels on the atlas surface. (b): Lobar labels on the atlas sphere. (c): Warped atlas labels on the subject sphere. (d): The deformation field used to warp atlas labels onto the subject. (e): The propagated atlas labels on the subject surface. (f): The manual labels on the subject surface. Each label value represents a lobar region: 1 frontal lobe, 2 temporal lobe, 3 parietal lobe, 4 occipital lobe.

the sum of area belongs to that label. If there are two points, two third will be added.

In detail, $|A \cap B|$ is calculated as the area of triangles with its point(s) assigned by both of the automated and the manual method with this particular label. $|A| + |B|$

is calculated as the sum of the area of triangles with vertices assigned by the manual method plus the area of triangles with vertices assigned by the automated method. $|A \cup B|$ is calculated as the area of triangles with vertices assigned by the manual method or the automated method. Both Dice and Jaccard indices tell us how much two pieces of the surface, labeled with the same value, overlap each other. When there is no overlapping, Dice and Jaccard both are equal to 0.0 and when there is a completely overlapping, both of them are equal to 1.0. The relationship between Dice and Jaccard is $D = 2J/(1 + J)$ or $J = D/(2 - D)$. Since Dice and Jaccard is always interchangeable, we choose Dice to evaluate the similarity between manual labels and proposed automated labels.
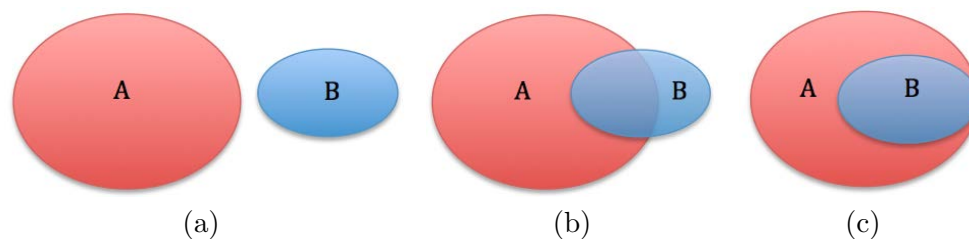
Figure 2.57: The situations of overlapping between A and B.

According to Eq. 2.52, when A and B have no overlapping, $A \cap B$ is empty as shown in Fig. 2.57a. The Dice index D is zero. When A and B partially overlap with each other as shown in Fig. 2.57b, the value of D is within $(0.0, 1.0)$. When A and B keep covering the same amount of area but with more overlapping, the denominator of

Eq. 2.52 keeps the same value but the value of the numerator (intersection) is bigger. In an extreme situation, when B is completely inside of A as shown in Fig. 2.57c, the value of D equals to $\frac{2|B|}{|A|+|B|}$. Although the value of D itself is incapable of recognizing whether A and B is partially overlapped or one is inside of the other, it still can give an idea about the similarity of A and B for the same label value from a set of manual labels and a set of automated labels.

Six subjects were enrolled voluntarily into an MR imaging protocol with informed written consent obtained in accordance with the institutional review board at the University of Iowa. The MR protocol acquired three image sets: T1, T2, and PD weighted scans. The images were obtained on a GE Signa 1.5T MR scanner. The T1 weighted scan was acquired using a 3D spoiled recalled gradient echo sequence with the following scan parameters: TE = 5 ms, TR = 24 ms, flip angle = 40°, NEX = 2, FOV = 26 x 19.2 x 18.6 cm, matrix = 256 x 192 x 124. The PD and T2 weighted scans were acquired using a fast spin-echo sequence with the following parameters: TE = 28/96 ms for the PD and T2 respectively, TR = 3000 ms, slice thickness/gap = 3.0 to 4.0 mm / 0.0 mm, NEX = 1, FOV = 26x26 cm, matrix = 256 x 192, ETL = 8.

All of the MRI data were analyzed using the BRAINS AutoWorkup pipeline, which included preprocessing (see Sec. 2.2), surface generation (see Sec. 2.3), and surface geometry features calculation (see Sec. 2.4). The first part is the image preprocessing. It adjusts the T1 image according to the AC-PC line that starts from the anterior commissure (AC) and ends at the posterior commissure (PC). When it

adjusts (rotates) the T1 image, it also resamples it into an isotropic image in all three dimensions (axial, sagittal, and coronal). The preprocessing also registers T2 image with T1, strips skull to keep only brain region, corrects the intensity inhomogeneity, rescales the intensity to 0 to 255, and generates the tissue classified image. The second part of AutoWorkup is to generate topologically corrected cortical surfaces for both hemispheres. In order to do that, it has to fill up ventricles and other subcortical regions to make sure the final surface is a closed surface. Then, the left and right hemispheres are separated using a left and a right hemisphere mask. The cortical surface of each hemisphere is generated after the topology correction is applied. The surface decimation is applied to the raw surface to reduce the number of vertices and triangles and the surface smoothing is applied following the decimation to generate a smoothed surface which is located at the boundary of the parametric ribbon of white matter and gray matter. Only the cortical surface of the left hemisphere is used to test the label propagation from a single subject atlas here.

Lobar labels were manually delineated in the volumetric image space by a rater. The labels were then mapped onto the cortical surfaces. The cortical surface of one of the subjects was selected as the atlas. The atlas was selected by having the median volume of the gray matter plus the white matter among six subjects. Labels from the atlas surface were propagated to the rest of subjects using the method described above in this section. The propagated (automated) labels were then evaluated using Dice indices to show their similarities with the manual labels. Results are given in Sec. 3.2.

2.8   Surface Atlas Generation

A cerebral cortex atlas that is useful in the cortical parcellation has to include at least two types of information: a standard coordinate system and a representation of anatomical structures that exists in a population. A standard coordinate system is need to align all cortical surfaces with the atlas and to do computational study among a large population of subjects; a good representation of anatomical structures are need to represent common structures (not biased by a single subject's structure) while keep the geometry values "sharp" enough to be able to drive the surface registration. The gradient of scalar values will be small if the average atlas is too smoothed. A review of methods that have been used by different groups to generate the cortical surface atlas was introduced in the Sec. 1.3 of Chap. 1.

To avoid the bias of using a single subject as the atlas, we generate the population atlas from a group of training subjects in an efficient way. The population average is generated by registering training subjects to a template, which is chosen randomly from the training set. Specifically, the first subject is chosen as the template. The multi-resolution pairwise surface registration framework proposed in Sec. 2.6 is used to register any other training subject (the moving surface) to the first training subject (the fixed surface) in the spherical domain. Each pair-wise registration produces a deformation field that deforms space (vertices) of the template (fixed) sphere to the space of the subject (moving) sphere by giving each vertex a displacement vector in the tangent plane along the sphere. The illustration of the deformation field is shown as Fig. 2.56d. Then, the deformation field is used to resample scalar values from the

training subject and map them onto the atlas space, in which the average scalar value is calculated. The whole process is shown as the flowchart in Fig. 2.58.
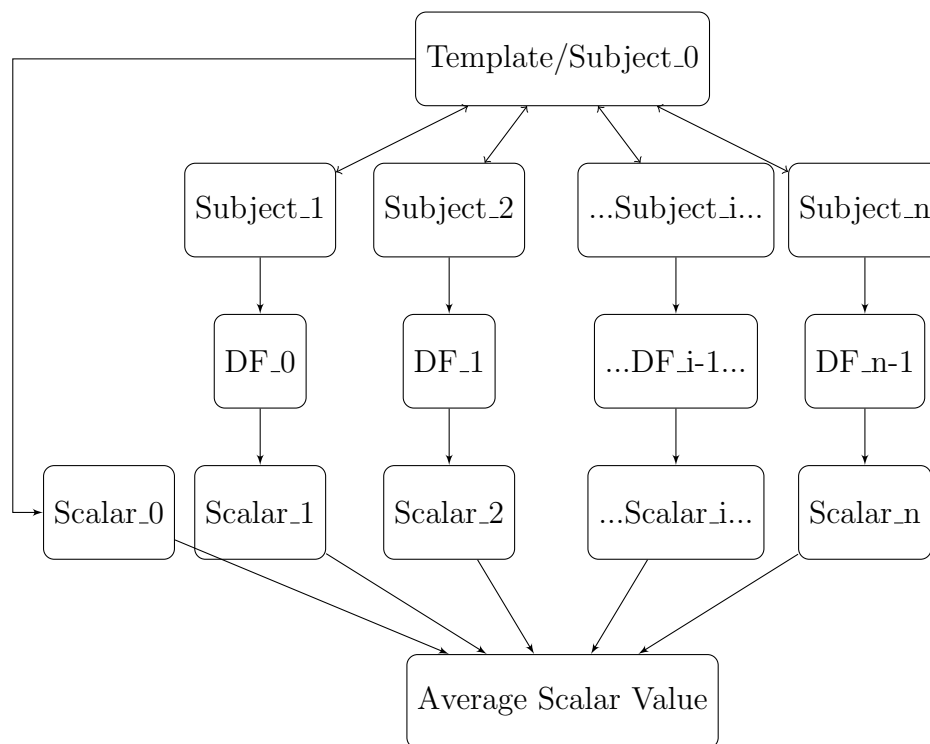
Figure 2.58: The flowchart of generating the average population atlas. "DF" stands for the "Deformation Field" and "Scalar" stands for scalar values on the corresponding subject.

35 training subjects were chosen randomly from 49 subjects enrolled voluntarily with informed written consent obtained in accordance with the institutional review board at the University of Iowa to generate the population atlas of the cortical surface. The MRI scans of them were acquired using the protocol mentioned in Sec. 2.1. In order to generate a generalized atlas which incorporates a wide range

of anatomical variance of cortical structures, we use a group of male subjects, with a wide range of age, and with different clinical status (healthy and unhealthy). The ages of 35 training subjects are between 12 and 41, with the average of 25.6 and the standard deviation of 6.3 years. Among 35 subjects, 19 are healthy controls, 14 are diagnosed as schizophrenia patients, 1 has delusion disorders, and 1 has major depression.

All MRI scans of 35 subjects are input into BRAINS AutoWorkup to automatically generate topologically corrected cortical surfaces for the left and right hemispheres respectively. Each vertex of the cortical surface is assigned with scalar values of geometry features such as "DistanceToPCIS", "DistanceToPCAP", "DistanceToHull", "MeanCurvature", and "CorticalThickness". The last geometry feature is not used in the surface registration described in Sec. 2.6 to align cortical surfaces together but it can be stored on the surface for the future analysis.

The process in BRAINS AutoWorkup that takes subject's MR images (T1- and T2- weighted) and generates the left and right hemisphere cortical surfaces includes three parts: preprocessing, surface generation, surface geometry calculation, as described in processing the subjects' data that have been used to test lobar labels propagation in the last section.

Then, 35 labeled cortical surfaces of left hemisphere are given to the BRAINS SurfaceAtlas to generate a surface atlas automatically. The BRAINS SurfaceAtlas is a program in BRAINS software that can be used to do automated surface analysis and parcellation. BRAINS SurfaceAtlas maps each cortical surface onto a sphere with

100 mm radius. All sets of scalar values (of geometry features and manual labels) are also mapped onto vertices of the sphere. Then, each surface sphere of 34 subjects are registered to the surface sphere of the first subject which is used as a template subject here. The framework of the multi-resolution surface registration on spheres are discussed on page 104 in Sec. 2.6. The parameters used in rigid and nonrigid surface registration are shown as Table 2.6 on page 117 and Table 2.7 on page 118.

As mentioned in Sec. 2.3, all cortical surfaces generated in this study contain 35,002 vertices which compose to 70,000 polygons (triangles). When the cortical surface is mapped onto a sphere with 100 mm radius, all vertices and triangles have the one-on-one correspondence between the original surface and the sphere, which means, there are also 35,002 vertices and 70,000 triangles on the sphere. After each pair-wise surface registration, a full mapping from each of the 35,002 template vertices onto the subject sphere is generated. Each template vertex will fall into the space of a triangle on the subject sphere. Each triangle has 3 vertices. As mentioned in Sec. 2.4, each vertex on a surface can be associated with scalar values of "DistanceToPCIS", "DistanceToPCAP", "DistanceToHull", or "MeanCurvature", which is generated by the last part of BRAINS AutoWorkup to generate the cortical surface from T1 and T2 MR images. Thus, the scalar value of the template vertex mapped into a triangle of the subject sphere can be calculated by interpolating the scalar values at 3 vertices of that triangle. The linear interpolation of a point located in a triangle using the scalar values of the triangle's vertices is shown as Eq. 2.47 in Sec. 2.6 using the barycentric coordinates. In this way, the scalar values on the subject sphere are resampled onto

the vertices of the template sphere. Each training subjects scalar values are resampled onto the template sphere and the average scalar values across all training subjects for each vertex on the template sphere can be calculated. The results of calculating the average scalar values of "DistanceToPCIS", "DistanceToPCAP", "DistanceToHull", and "MeanCurvature" on the template sphere are shown in Chap. 3 and since every cortical surface and its sphere has the one-on-one correspondence for vertices and polygons, the average scalar values can be mapped onto the original cortical surface of the template as well. Those results are shown together in Sec. 3.3 of Chap. 3.

Each cerebral hemisphere of 35 training subjects, was divided into 49 regions which were delineated by a rater. Details of the definition of those regions are given by a series of papers by Crespo-Facorro and Kim[69][68][67]. Each label is stored as an individual mask image overlapping in the same space of the T1 MR image. A filter published in the Insight Journal is used to combine individual labels into a label map image for each subject[162]. The filter gives each label an integer number so that all label values in the output are consecutive, and it is set to ignore any collision that could happen between two labels. The label map is applied onto vertices of the cortical surface of the left and the right hemispheres. For each vertex on the surface, the label of it is chosen to be the label of a pixel that is closest to the vertex in the physical space.

Then, we combine and redefine the labels mapped from 49 labels from the label map to be 24 labels and assign consecutive integers to the new labels as a set of scalar values associated with vertices of the cortical surface. Table 2.8 shows the

Table 2.8: The Definition of Surface Parcellation Labels

Label Value	Full Name	Abbreviation	Lobe
4	Anterior Cingulate Gyrus	ACiG	Frontal
5	Inferior Cingulate Gyrus	ICiG	Frontal
6	Inferior Frontal Gyrus	IFG	Frontal
11	Medial Frontal Gyrus	MFG	Frontal
13	Orbitofrontal Cortex	OFC	Frontal
14	Pre-central Gyrus	PreCG	Frontal
19	Superior Frontal Gyrus	SFG	Frontal
20	Straight Gyrus	SG	Frontal
3	Fusiform	FU	Temporal
9	Inferior Temporal Gyrus	ITG	Temporal
12	Middle Temporal Gyrus	MTG	Temporal
17	Parahippocampal Gyrus	PHG	Temporal
22	Superior Temporal Gyrus	STG	Temporal
23	Temporal Pole	TP	Temporal
1	Parietal	PA	Parietal
15	Posterior Cingulate Gyrus	PoCiG	Parietal
16	Pre-cuneus Gyrus	PreCuG	Parietal
18	Post-central Gyrus	PoCG	Parietal
2	Cuneus	CU	Occipital
7	Inferior Lateral Occipital Gyrus	ILOG	Occipital
10	Lingual	LG	Occipital
21	Superior Lateral Occipital Gyrus	SLOG	Occipital
0	Unknown	UN	None
8	Insula	IS	None

label value, full name, abbreviation, and location (as in brain lobes) of each label used as the refined label compared with the lobar label in this dissertation. The actual location of each label is shown in Fig. 2.59. In Table 2.8, the "Unknown" is for the region that does not really belong to the cerebral cortex and includes the ventricles and corpus callosum.

After a training subject is registered to the template (first) subject by the
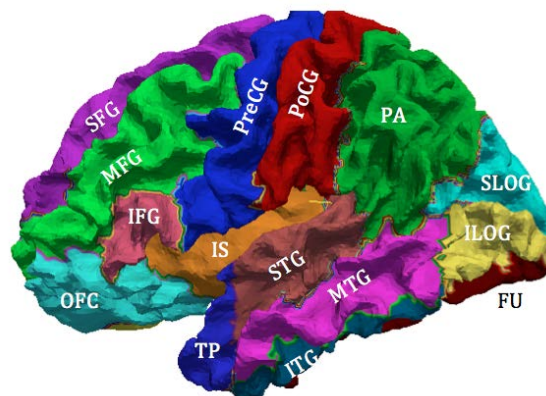
(a) The lateral view
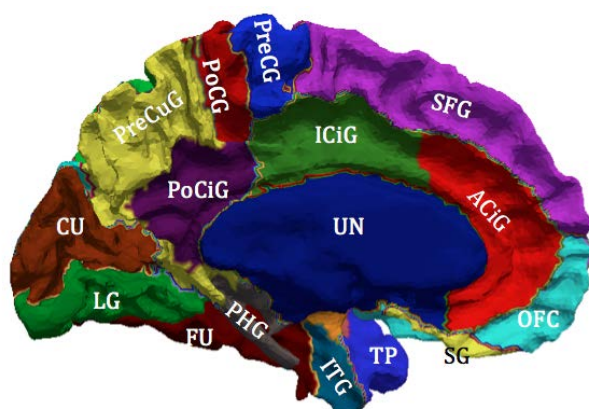
(b) The medial view

Figure 2.59: The refined parcellation labels on the cortical surface. Regions are marked with labels' abbreviations. Please refer to Table. 2.8 for the full names. The color code used for 24 labels with label value from 0 to 23 is given in Table. 2.9.

surface registration, a deformation field is generated to map vertices from the template space to the subject space as a function of coordinates in the template space. Please notice that the coordinates here are actually spherical coordinates because every vertex is mapped on a sphere. The deformation field can be used to map vertices on the icosahedron IC7 in the template space onto corresponding points in the subject space. Those points mostly fall into triangles on the subject sphere (the corresponding

Table 2.9: The Color Code for Refined Parcellation Labels

Label Value	Abbreviation	Red	Green	Blue
0	UN	0	0	153
1	PA	0	204	0
2	CU	153	51	0
3	FU	102	0	0
4	ACiG	255	0	0
5	ICiG	51	153	0
6	IFG	255	102	153
7	ILOG	255	255	102
8	IS	255	153	0
9	ITG	0	102	153
10	LG	0	153	0
11	MFG	0	255	0
12	MTG	255	51	255
13	OFC	51	255	255
14	PreCG	0	0	255
15	PoCiG	102	0	102
16	PreCuG	255	255	51
17	PHG	102	102	102
18	PoCG	204	0	0
19	SFG	204	0	255
20	SG	255	255	0
21	SLOG	0	255	255
22	STG	204	102	102
23	TP	51	0	255

point could be a corner or locate at an edge of a triangle as well). The nearest-neighbor interpolation is used to resample manual labels from the subject to vertices of the icosahedron IC7 in the template space. After all of the training subjects' labels are mapped onto the icosahedron IC7 in the template space. A probabilistic atlas can be generated using that IC7 regular sphere, so the atlas is a regular sphere with 163,842 vertices and 327,680 polygons (triangles). It is called as "AtlasIC7" in this

dissertation.

After all of training subjects' labels are mapped onto the icosahedron IC7 in the template space. The prior information of labels in training set can be saved on the AtlasIC7.

First, the prior probability of each label at each vertex on IC7 can be calculated as:

$$p(L_r = l_1) = \frac{\# \text{ of times label } l_1 \text{ occurs at vertex } r \text{ in the training set}}{\text{number of training subjects}} \quad (2.54)$$

where $p(L_r = l_i)$ denotes the probability of label l_1 occurs at atlas vertex r. So, if all training subjects are labeled as l_1 at atlas vertex r, the probability of $p(L_r = l_i)$ is 1.0. Likewise, if none of the subjects has label i at vertex r in the template space, the probability of $p(L_r = l_i)$ is 0.0.
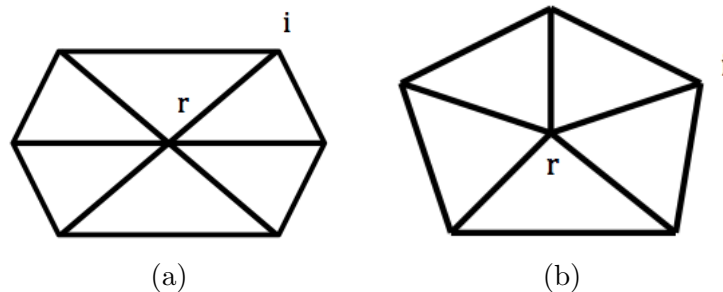
Figure 2.60: The types of neighborhood exist on icosahedron IC7.

In addition to the prior probability at a single vertex on the atlas, the prior information in the neighborhood can also be generated to help us fully use the man-

ual labels on the training set. Since AtlasIC7 is an icosahedron sphere that has a homogenous geometry, there are only two types of neighborhood for any vertex on AtlasIC7, shown as Fig. 2.60a and Fig. 2.60b. The prior probability of the labels at the pair vertices of a center vertex r and one of it's neighbors i is calculated as a conditional probability:

$$p(L_r = l_1 | L_i = l_2) = \frac{\# \text{ of times that } L_i = l_1 \text{ at } i \text{ and } L_r = l_2 \text{ at } r}{\# \text{ of times that } L_i = l_2 \text{ at } i} \qquad (2.55)$$

where $p(L_r = l_1 | L_i = l_2)$ denotes the probability that label l_1 occurs at vertex r when label l_2 occurs at vertex i.

Van Essen proposed a metric to evaluate the consistency of anatomical structures across training subjects, the index of surface alignment consistency (SAC)[112]. Assume there are N training subjects aligned in the atlas space, and each of them are parcellated with n manual labels. For each label, there are N_{total} number of vertices on the atlas surface that could possibly labeled as this label. The value of SAC for this label is calculated as:

$$\text{SAC} = \sum_{i=1}^{N} \frac{(i-1)n(i)}{(N-1)N_{\text{total}}} \qquad (2.56)$$

where $n(i)$ is the number of vertices on the atlas sphere assigned to this label by only one subject $(i = 1)$, by two subjects $(i = 2)$, etc., up to all N subjects in the training set. The value of SAC is between 0 and 1, whereas 1.0 indicates perfect alignment across all training subjects and 0 indicates no overlap among training subjects for this label. The higher SAC value indicates the higher consistency among training subjects for this label in the atlas space. Ideally, if there is no inter-individual variance for an

anatomical label and if there is no error exists in the surface registration, the SAC index for that label is 1.0.

2.9   Surface Parcellation Using A Probabilistic Atlas

Once the probabilistic atlas is constructed from a group of training subjects as described above, it can be used to automatically parcellate a new subject surface. FreeSurfer uses Bayesian framework to solve the problem of automated surface parcellation given the observed surface geometry and prior probability of labels in the training set. However, in this dissertation, we use a very efficient method to parcellate the subject's cortical surface and apply minor adjustments to the resulting labels guided by the local curvature information and pair label probability in the first order neighborhood on that subject.

As mentioned in the section of "Data Acquisition" (Sec. 2.1, 49 subjects have been enrolled in the experiment of this dissertation and MRI scans of them have been collected using the protocol described in Sec. 2.1. 35 subjects have been randomly chosen to be the training set to generate the population atlas which incorporates average geometry features and probabilities of manual labels across training subjects, and the remaining 14 subjects are used to test the proposed surface parcellation framework.

The testing set consists of 6 healthy controls and 8 schizophrenia patients. The ages of the subjects ranged from 16 to 39, with the mean: 24.9 years old and the standard deviation: 6.5 years. The MR scans of these 14 subjects went through BRAINS AutoWorkup pipeline to be processed and 28 genus zero cortical surfaces

of both hemispheres were generated. Only 14 surfaces from the left hemisphere were used as a testing set here.

As the training subjects, each of the testing subject also has manual labels that can be mapped to vertices on its cortical surface. Originally, there were 49 labels manually delineated by a rater which are then combined and renamed to be 24 labels with consecutive label values as shown in Table 2.8. Next, cortical surfaces were automatically parcellated and the resulting labeling was compared to the manual rater.

First, the cortical surface of each subject were given to BRAINS SurfaceAtlas to be registered with the atlas. The atlas is the population atlas with average geometry features mapped on the template sphere. The test subject's surface needs to be flattened onto a sphere first (see Sec. 2.5 "Surface Flattening"). The the atlas sphere was registered with the subject sphere in a multi-resolution registration framework (see Sec. 2.6 "Spherical Surface Registration"). Then, the inverse deformation field was used to map "MeanCurvature" from the subject sphere to the AtlasIC7, on which the subject's curvature is used to help adjust the labels for that subject.

As we generate the probabilistic atlas in the section of "Surface Atlas Generation" (Sec. 2.8), the prior probability of each label at each vertex is calculated using Eq. 2.54. In reality, the maximum number of labels that could possibly occur at a vertex is 6, so to predict a label at a vertex for one subject is to select one label out of no more than 6 possible labels. The simplest way to predict is to use the most likely label which is the label that has the agreement among major number of subjects in

the training subjects at the vertex on the atlas space. Fig. 2.61 shows the most likely labels on AtlasIC7 and the propagated most likely labels from the atlas sphere to one of the testing subject (please refer to Sec. 2.7 "Label Propagation" for details). The most likely labels can be used as an initial estimation for that subject.

| (a) | (b) | (c) |
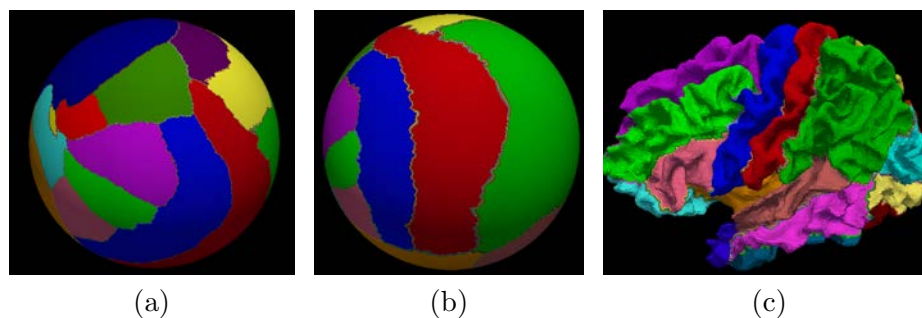
Figure 2.61: An example of mapping the most likely labels to a subject. (a) shows the most likely labels on AtlasIC7. (b) shows the most likely labels mapped from the AtlasIC7 to the subject sphere using the deformation field generated by the surface registration. (c) shows the most likely labels on the subject cortical surface. The average Dice index of the similarity between the most likely labels shown here and the manual labels is 0.87.

The surface parcellation using most likely labels is simple and fast. Ideally, if the surface registration has no errors and if the variability of the cortical surface structure is not so high, the most likely label method can give us good parcellation results which have high agreement with manual labels judging by Dice indices. However, pre-assumptions above are not valid for the human cerebral cortex parcellation because of following potential reasons:

- The surface registration can not bring a perfect alignment between the subject

surface and the atlas surface.

- Scalar values on the atlas are average values. In some regions, they might be over-smoothed so there is not enough anatomical information to drive the registration.

- The subject has a unique folding pattern which is unlikely to be captured by the average geometry features on the atlas.

Therefore, we propose an adaptive labeling method, which uses the most likely labels on the atlas as an initial parcellation and combines the prior information in the first order neighborhood, local curvature information, and locations (for example, the occipital part of fusiform) together to make adjustments to the most likely labels.

Theoretically, the adjustment on the most likely labels can be made on all vertices on the original cortical surface. However, considering the complexity of the folding patterns on human cortical surfaces and the lack of consistent criteria to decide the boundaries for different regions of interests, we choose to adjust boundaries at only a subset of regions. They are the post-central gyrus (PoCG), anterior cingulate gyrus (ACiG), fusiform (FU), inferior temporal gyrus (ITG), parahippocampal gyrus (PHG), inferior lateral occipital gyrus (ILOG), and superior lateral occipital gyrus (SLOG). As for labels that are other than these, the most likely labels can provide satisfactory results because one or more of the following reasons:

1. Major sulci are located at the boundaries of those regions.

2. Substantial surface area are covered by those regions. The relationship between the Dice index and the surface area for a certain label is discussed in Chap. 3.

3. The locations are stable across subjects, such as the "Straight Gyrus" and "Temporal Pole".

4. The region of interests are close to the anatomical features that are used in the registration. For example, the pre- and post- central gyri are close to the PC point in the anterior-posterior direction.

For the conveniences to use the prior probabilities on the atlas and to incorporate a vertex's neighborhood information into the adjustment, it is performed on the regular sphere AtlasIC7. So it requires to map the subject's geometry features needed in the adjustment onto the AtlasIC7. They are "DistanceToPCIS" and "MeanCurvature". The mapping is done by resampling the subject's geometry features on its deformed sphere (by the deformation field generated from the surface registration) for an AtlasIC7 vertex using the linear interpolation. In summary, if a vertex is located in the regions listed above, a list of information needed for the center vertex and its first order neighbors are: current labels; the prior probability for each possible label that could occur at those vertices (Eq. 2.54); the prior conditional probability for the center vertex's label on its neighbor's label (Eq. 2.55); the mean curvatures; and the distances to the PC point in the inferior-superior direction.

The first type of label adjustment is to adjust the boundary between two regions in a one-way direction ("push" the boundary from label A to label B). It is called "Type I Adjustment". The first place to make this type of adjustment is located at the inferior part of the boundary between the post-central gyrus (PoCG) and the parietal (PA), marked by the white circle as in Fig. 2.62a. The location is constraint
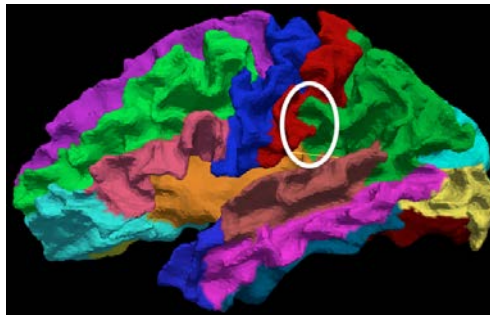
(a)
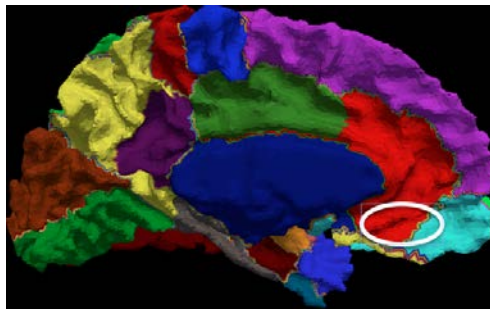
(b)
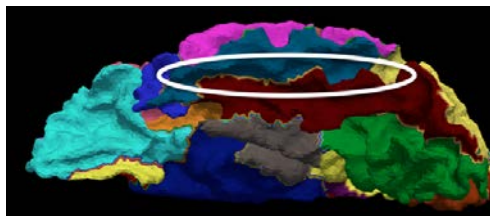
(c)

Figure 2.62: Locations of "Type I Adjustment" based on the most likely labels. (a) circles the location of the to-be-adjusted boundary between the PoCG (in red) and PA (in green). (b) circles the location of the to-be-adjusted boundary between the ACiG (in red) and OFC (in light blue). (c) circles the location of the to-be-adjusted boundary between the ITG (in air force blue). The labels in display are most likely labels.

by the Euclidean distance from the vertex to the PC point and the probability of the to-be-adjusted vertex being labeled as PoCG is not too low (> 0.1). The adjustment is performed by pushing the boundary toward the parietal iteratively. Since the most

likely label here tends to mistake the post-central gyrus to be the parietal, only one direction adjustment (from the post-central to the parietal) is needed. The actual adjustment of a vertex that is currently labeled as a "parietal" in the first order neighborhood of a "post-central gyrus" vertex, has to be also assured by having the same sign of the mean curvature value and the pair of labels (both "post-central") at those exact vertices on the AtlasIC7 can be referred in the training set, as the prior probability of being labeled as "post-central" for each individual vertex and the prior conditional probability as neighbors are all non-zero. The similar strategy is applied to push the boundary from the orbitofrontal cortex (OFC) to the anterior cingulate gyrus (ACiG), except that the location of the to-be-adjusted vertex is constrained by the probability of being labeled as the superior frontal gyrus (SFG) is zero (no adjustment is needed when the boundary is close to SFG). The region is marked by the white circle in Fig. 2.62b. So is the strategy to push the boundary from the inferior temporal gyrus (ITG) to the fusiform in the temporal lobe (see Fig. 2.62c). If "Type I Adjustment" is considered to be typical adjustments, there are two other types of adjustments that only apply to the characteristics at special boundaries. The first "special boundary" is between the parietal (PA) and the superior lateral occipital gyrus (SLOG). The boundary is marked by the white circle in Fig. 2.63. The actual location of the part of boundary is constraint by recognizing it as also "close to the inferior lateral occipital gyrus (ILOG)" ($p(L_r = \text{ILOG}) > 0$). It is referred as the "the parietal-occipital boundary on the lateral surface of the brain" in Crespo-Facorro and Kim's paper based on which the original manual labels were
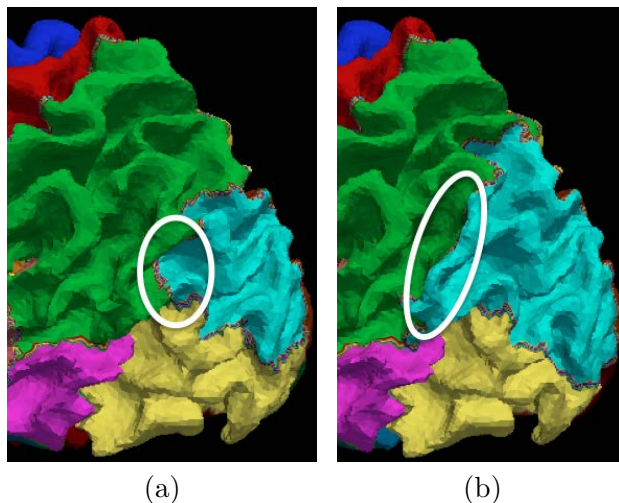
Figure 2.63: The boundary between PA (in green) and SLOG (in yellow). A part of the boundaries are marked by the white circle. (a) marks the boundary based on the most likely labels before any adjustment and (b) marks the new boundary after the adjustment.

delineated[69]. In the paper, the boundary is defined by "the lateral surface points located at the same level as the deepest points of the (parietal-occipital sulcus) POS". We studied the characteristic of the boundary on training subjects. It shows that the sum of mean curvatures at vertices on the boundary should be negative, so if a subject has a positive sum of mean curvatures, an adjustment is needed. The adjustment is made by pushing the boundary toward the parietal using the same iterative strategy above for "Type I Adjustment", except that the sum of mean curvature at the new boundary is calculated after each iteration. The adjustment stops when the sum value becomes negative.

The last but not the least region that needs to be adjusted is the parahippocampal gyrus (PHG). It is significantly affected by the surface generation. For
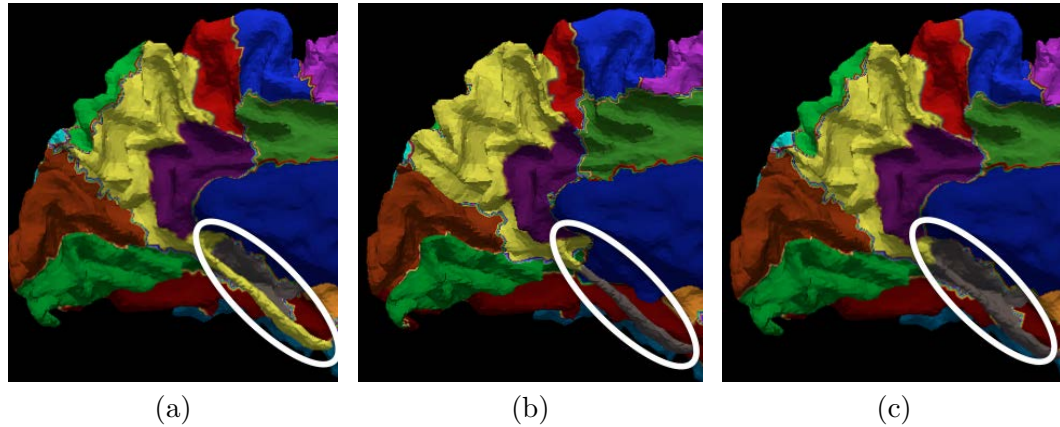
Figure 2.64: The mislabel at the parahippocampal gyrus (in gray). (a) shows that the PHG is mislabeled as the pre-cuneus gyrus (PreCuG) by the most likely labels (in yellow). (b) shows the manual label at the same region. (c) shows the same region after the label adjustment.

example, there is one subject out of 14 subjects in the testing set has the parahippocampal gyrus marked by the white circle in Fig. 2.64b. Neither of the label adjustment strategies mentioned above would help to correct the mislabeling at that region (most likely labels are shown in Fig. 2.64a). It can only be adjusted by growing the current PHG region into regions with non-zero prior probabilities being labeled as PHG and also with non-zero pair conditional probabilities at current PHG vertex and at to-be-adjusted non-PHG vertex. The region growing is constraint at the locations "close to lingual gyrus (LG) and pre-cuneus gyrus (PreCuG)" $((p(L_r = \text{LG}) > 0)\&(p(L_r = \text{PreCuG}) > 0))$. After the adjustment, the new PHG is shown as the marked region in Fig. 2.64c. It raises the Dice index of PHG for that subject from 0.0 to 0.52.

Since the adjustment at the boundary affects the labels at both sides of it,

the actually adjusted regions are: PoCG, PA, SLOG, ILOG, FU, ITG, PHG, OFC, and ACiG. The improvements judged by the Dice index are going to be shown in Sec. 3.4 of the next chapter. The change of the Dice index between the automated label and the manual label can be reflected by the coefficient of variance (CV), which is estimated by:

$$\hat{c}_v = \frac{s}{\bar{x}} \tag{2.57}$$

where s is the sample standard deviation and $\bar{x}$ is the sample mean.

Sec. 1.3 reviewed the surface parcellation in the FreeSurfer, a software application developed at the Martinos Center for Biomedical Imaging (`http://surfer.nmr.mgh.harvard.edu/`). The source code of the proposed surface parcellation is a part of the open source software system BRAINS3, which can be download from its website (`http://www.nitrc.org/projects/brains/`).

To be able to compare the proposed surface parcellation method with FreeSurfer, the same MR scans of 49 subjects were processed using FreeSurfer and the cortical surfaces are parcellated into 36 regions (34 cortical ROIs, insula and an unknown region)[103]. The surface generated by FreeSurfer is in a different space compared to the BRAINS surface. An iterative closest point (ICP) registration was used to bring the surfaces into correspondence. To apply the FreeSurfer labels to the BRAINS surface, the closest point on the FreeSurfer surface is used to define the label for each vertex. Only the left cortical surface for each subject was used for this evaluation. Fig. 2.65 shows FreeSurfer labels mapped on BRAINS surface and Table 2.10 lists the region names corresponding with the number marked on the surface in Fig. 2.65.
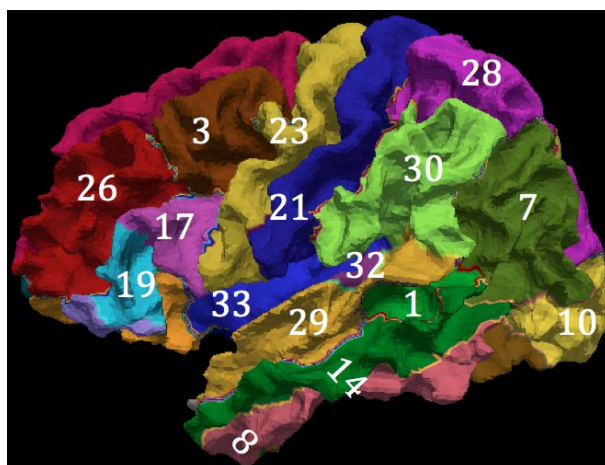
(a) Lateral View
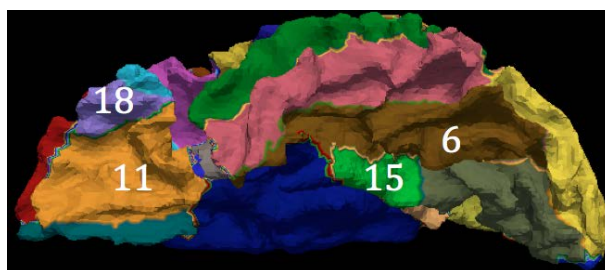
(b) Caudal View
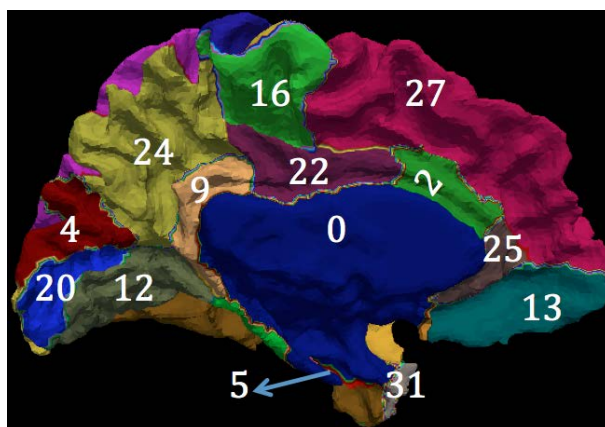
(c) Medial View

Figure 2.65: Parcellation labels defined in FreeSurfer. The full names of regions 0 to 33 that can be seen in different views are given in Table 2.10.

Table 2.10: The Names of FreeSurfer Regions on A Cortical Surface

Number	Region	Number	Region
0	Unlabeled subcortical region	17	Pars opercularis
1	Banks superior temporal sulcus	18	Pars orbitalis
2	Caudal middle frontal gyrus	19	Pars triangularis
3	Caudal middle frontal gyrus	20	Pericalcarine cortex
4	Cuneus cortex	21	Postcentral gyrus
5	Entorhinal cortex	22	Posterior-cingulate cortex
6	Fusiform gyrus	23	Precentral gyrus
7	Inferior parietal cortex	24	Precuneus cortex
8	Inferior temporal gyrus	25	Rostral anterior cingulate cortex
9	Isthmus-cingulate cortex	26	Rostral middle frontal gyrus
10	Lateral occipital cortex	27	Superior frontal gyrus
11	Lateral orbital frontal cortex	28	Superior parietal cortex
12	Lingual gyrus	29	Superior temporal gyrus
13	Medial orbital frontal cortex	30	Supramarginal gyrus
14	Middle temporal gyrus	31	Temporal pole
15	Parahippocampal gyrus	32	Transverse temporal cortex
16	Paracentral lobule	33	Insula

Please note that the frontal pole and the corpus callosum is missing from the surface, so there are 34 labels in total to compose the FreeSurfer's labels. They are marked with consecutive numbers in Fig. 2.65.

The same procedure is taken to generate the surface atlas from 35 training subjects. The population average of geometry features are the same, except the probabilistic prior based on the FreeSurfer labels was calculated. Then, the most likely labels were propagated from the atlas to individual subject, using the same deformation field generated above when the atlas sphere is registered to the subject sphere by a multi-resolution registration (see Sec. 2.7 for details). The parcellation is

applied to generate automated labels on left cortical surfaces of 14 testing subjects. The Dice index is calculated for each label on each subject to evaluate the resulting parcellation with FreeSurfer's parcellation.

There are many options to evaluate the accuracy of the automated parcellation apart from the similarity index (Dice). The accuracy can be quantified as the agreement between the automated parcellation and the manual parcellation at surface points. FreeSurfer use the disagreement between two kinds of parcellation method (automated vs. manual) calculated as the percentage of points to report the parcellation error[65]. Similarly, we calculate the parcellation error for each vertex on the AtlasIC7. It is called as "point-wise" parcellation error in this dissertation.

CHAPTER 3
RESULTS

3.1 Surface Flattening

The amount of distortion at each triangle on the cortical surface of one subject is shown in Fig. 3.1. It is calculated as D_i for triangle i using Eq. 2.26. The surface in Fig. 3.1 shows large expansion at the insula and some other regions close to the "split boundary" where the cortical surface was split into two parts. Significant compression is shown at regions furthest from the "split boundary". They are the anterior part of the frontal lobe and the posterior part of the occipital lobe.

(a) Lateral View   (b) Medial View
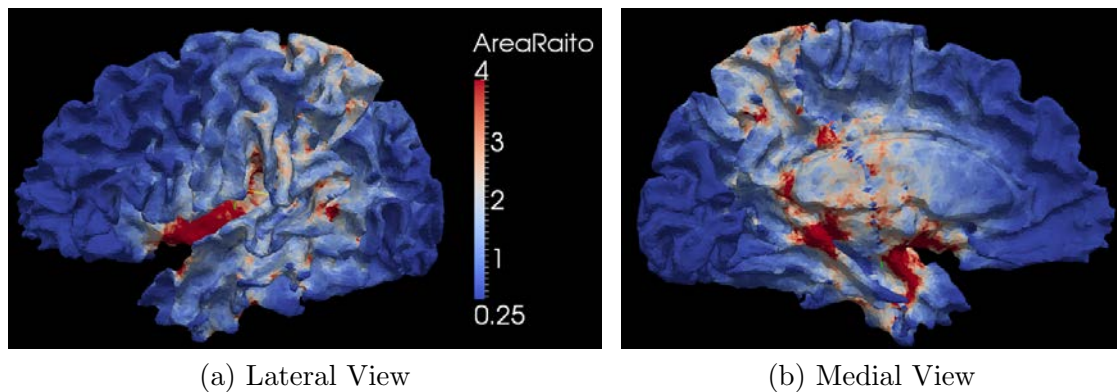
Figure 3.1: The areal distortion at surface triangles. The values of distortion are mapped with the triangles on the original surface of one subject. The surface is colored by legend shown at the right side of (a).

The distortion for each label R_l is calculated with Eq. 2.27. It can be calculated on cortical surfaces and on spheres of 14 testing subjects. Fig. 3.2a shows the ratio
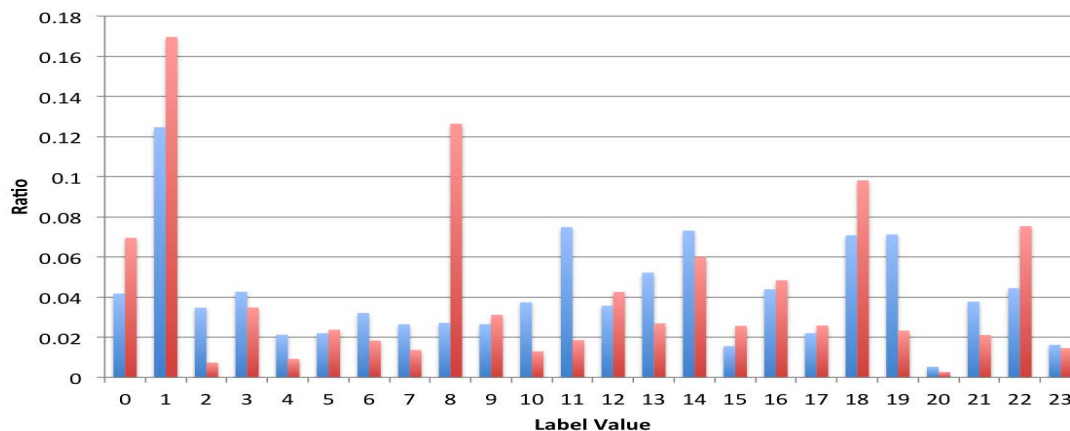
(a)

Figure 3.2: The areal distortion at parcellation labels. (a) shows the chart of the ratio value in Eq. 2.27 for each label on cortical surfaces (left bar in blue at each label) and the ratio value on spheres (right bar in red at each label).

value for each label (from 0 to 23) on surfaces (in blue) and on spheres (in red).

3.2   Lobar Labels Propagation Using Surface Registration

(a)   (b)   (c)
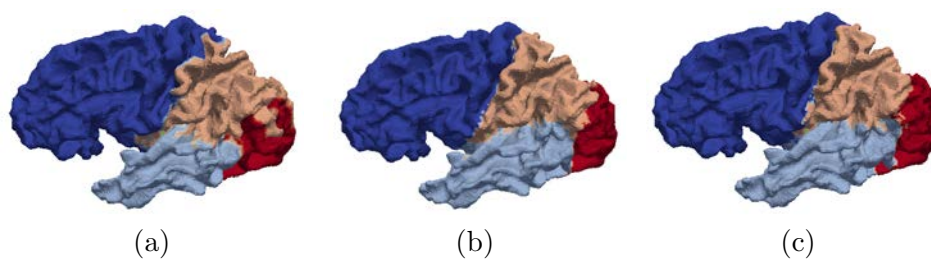
Figure 3.3: The result of surface parcellation for brain lobes, frontal (dark blue), temporal (light blue), parietal (tan), and occipital (red). (a) the mapping of labels from the atlas to the subject with rigid registration only. (b) the manual labels delineated by a rater. (c) the propagated labels from the atlas to the subject with a multi-resolution registration.

The label propagation method described in Sec. 2.7 is tested by propagating lobar labels from the cortical surface of a single subject atlas to cortical surfaces of 5 testing subjects. To show the role of spherical demons registration in the label propagation, Fig. 3.3 lists the left cortical surface of one testing subject with labels propagated from the atlas subject by the deformation field generated only from rigid surface registration (left), labels propagated by the deformation field generated from the multi-resolution surface registration (right), and manual labels (middle). Dice indices are used to calculate the similarity between manual labels and automated labels. In Fig. 3.3a, the Dice index shows 0.92 for the frontal lobe, 0.76 for the temporal lobe, 0.65 for the parietal lobe and 0.51 for the occipital lobe. After applying the multi-resolution surface registration, the same subject surface is labeled as shown in Fig. 3.3c, and the Dice indices then become 0.98, 0.90, 0.86 and 0.91 for the corresponding lobes. Table 3.1 shows the Dice indices for all of five subjects and the average Dice index across all lobes and all subjects is 0.89.

Table 3.1: Dice Indices for the Similarity Between Manual and Automated Labels

Lobe	Subject1	Subject2	Subject3	Subject4	Subject5	Average
Frontal	0.98	0.95	0.96	0.92	0.95	0.95
Temporal	0.90	0.90	0.82	0.87	0.87	0.87
Parietal	0.86	0.87	0.88	0.75	0.87	0.85
Occipital	0.91	0.88	0.87	0.87	0.88	0.88
Average	0.91	0.90	0.88	0.85	0.89	0.89

To show the improvement of using rigid followed by nonrigid registration in a multi-resolution manner compared to using rigid registration only in labeling each brain lobe, the average Dice indices of the overlapping between automated labels and manual labels for brain lobes across 5 subjects are given in Table 3.2. The values under "Rigid Only" are the mean and the standard deviation of Dice indices for labeling brain lobes across 5 subjects using rigid surface registration only. The values under "Rigid And Nonrigid" are the mean and the standard deviation of Dice indices for labeling brain lobes across 5 subjects using rigid followed by nonrigid registration in a multi-resolution manner. From the table we can see that, the multi-resolution surface registration improved significantly on propagating brain lobes from the atlas to a subject.

Table 3.2: Dice Indices for Brain Lobes Across 5 Subjects

Brain Lobe	Rigid Only		Rigid And Nonrigid	
	Standard Deviation	Mean	Mean	Standard Deviation
Frontal Lobe	0.01	0.92	0.96	0.01
Temporal Lobe	0.06	0.71	0.88	0.04
Parietal Lobe	0.09	0.66	0.86	0.01
Occipital Lobe	0.16	0.57	0.88	0.02

The average time to finish a pair-wise multi-resolution surface registration between two spheres is about 2 hours, but there are significant different for the time consuming at each resolution level. Fig. 3.4 shows the exact minutes needed to finish
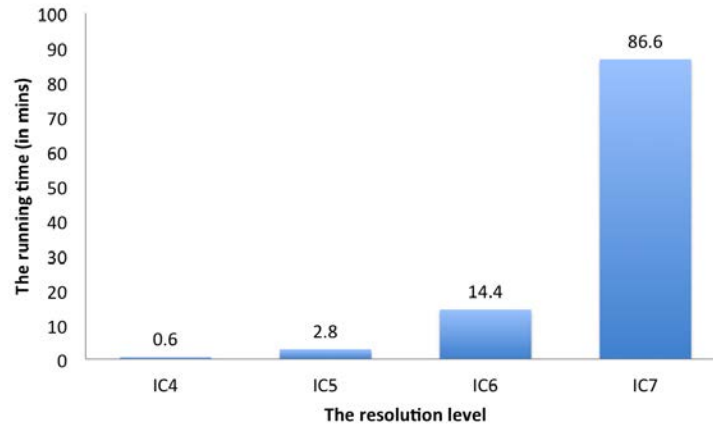
Figure 3.4: The time cost for each resolution level of the surface registration.

the rigid and nonrigid registration at each resolution level for one example. From the example shown in the figure, the last resolution level takes approximately 4 times longer than the total of time first three levels take to finish the registration.

3.3 Surface Atlas Generation

This section presents results of generating our surface atlas from left cortical surfaces of 35 training subjects. First, the population average of geometry features across 35 subjects are calculated in the template space. Then, the prior probability of manual labels on the training subjects are estimated on the icosahedron IC7 in the template space (AtlasIC7). The first training subject is chosen to be the template. Both of the prior probability of labels at individual vertex and the pair prior probability of labels at the center vertex with it's first order neighbor are calculated. Please refer to Sec. 2.8 in Chap. 2 for details of the surface atlas generation.

Fig. 3.5 shows the average geometry features ("DistanceToPCIS", "Distance-

ToPCAP", "DistanceToHull", and "MeanCurvature") calculated by following steps in Fig. 2.58, on the atlas sphere (left column) and on the cortical surface of the template (right column). Here, the average geometry features are mapped onto the cortical surface of the template just to show the reasonability of the resulting average values.

The prior information of labels at each independent vertex location can give us the distribution of each label (such as "parietal" shown in Fig. 3.6a). It also shows the homogeneity of folding patterns across training subjects. Fig. 3.6a shows the region that could possibly labeled as "parietal" (with probability > 0.0) is fairly big. However, from the color legend on the right side of it, we can see that a major part of the region has more than 75% chance to be labeled as "parietal", which means the folding patterns are used to define "parietal" are relatively homogeneity and the surface registration aligned them well. The "Number of Labels" shown in Fig. 3.8b can also present the consistency of anatomical structures across training subjects. It shows the number of possible labels that have occurred at a vertex in the atlas space. The number should consistent with (equal to) the number of labels that have nonzero probability at that vertex. Fig. 3.8b shows the atlas associated with "Number of Labels" as scalar values. From the figure we can see that, most of regions have no more than 3 possible labels to choose from.

The surface alignment consistency is calculated for each label using the Eq. 2.56. It is an index to show the consistency of alignment for an anatomical region across training subjects[112]. $SAC = 1.0$ indicates a perfect alignment at that region across
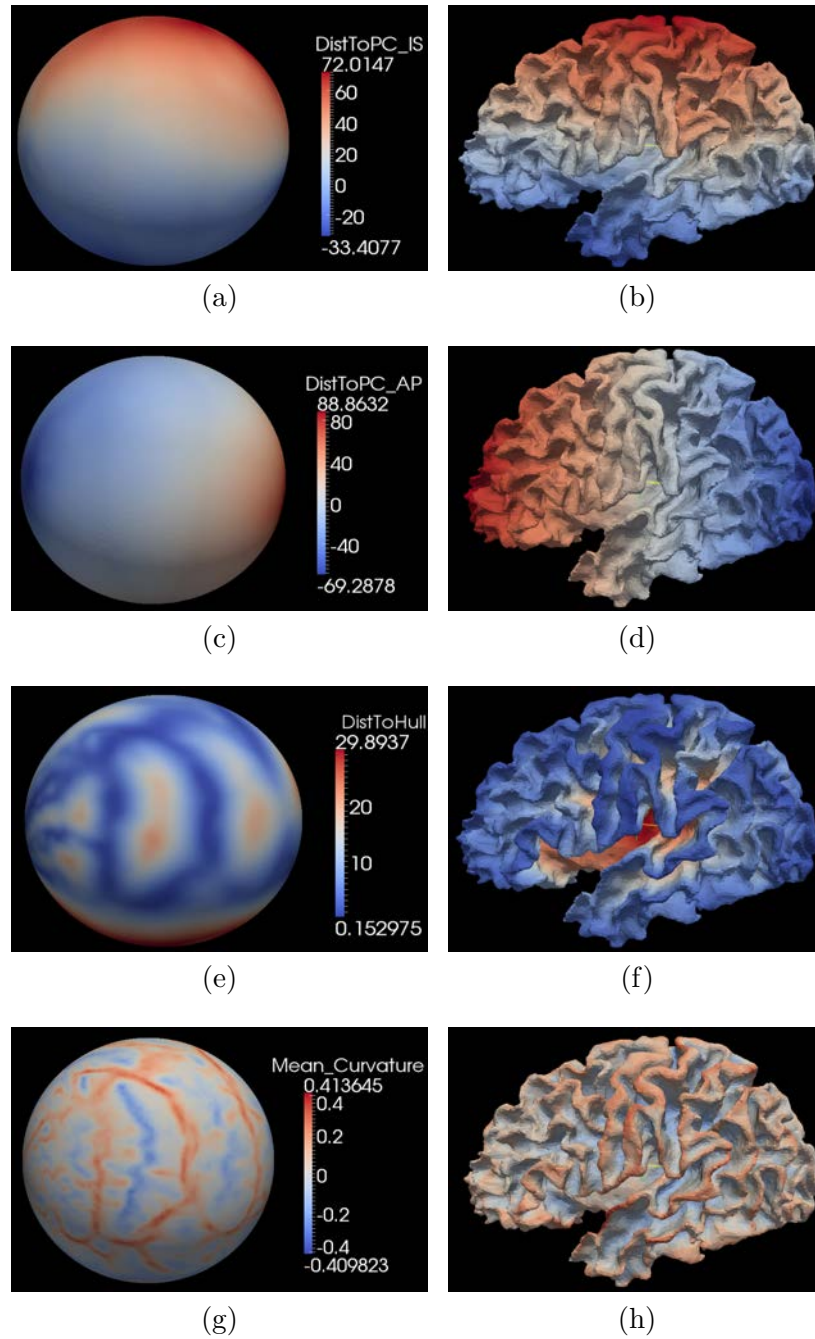
Figure 3.5: The atlas with population average values of geometry features. Both of the sphere and the surface are colored by the legend on the right side of spheres.

(a)   (b)
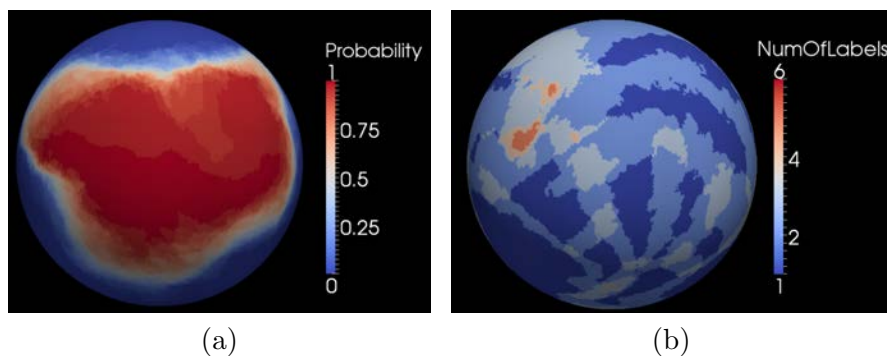
Figure 3.6: The atlas with prior information of labels. (a) shows the probability of being labeled as "parietal" on the atlas. (b) shows the number of labels that could possibly be given at vertices of the atlas. The color legend of (a) and (b) is shown on the right of each of them.

35 subjects, while $SAC = 0.0$ indicates no overlapping across them. The calculation is performed on the AtlasIC7 on which the probabilistic atlas is constructed. Fig. 3.7 shows a chart of SAC index at each label. In the chart, labels are denoted by abbreviations. Please refer to Table 2.8 for their full names.
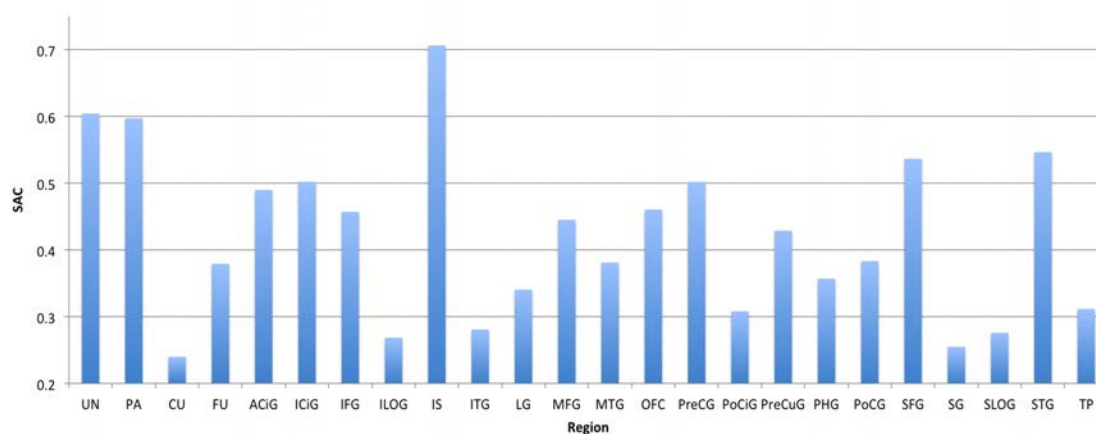
Figure 3.7: The values of surface alignment consistency (SAC) of parcellation labels.

(a) Lateral View   (b) Medial View
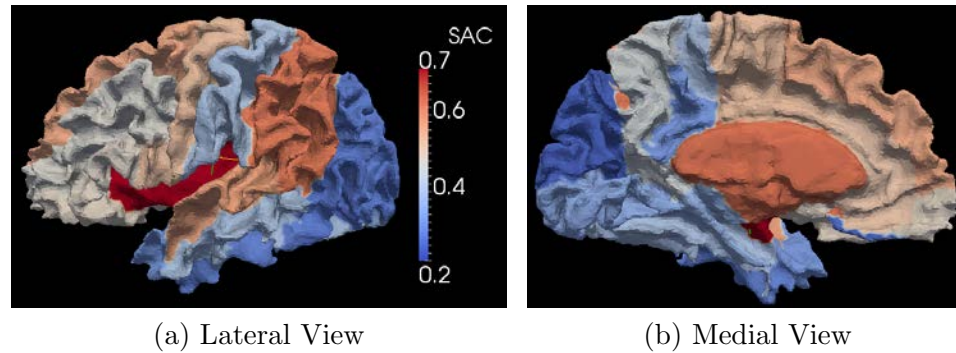
Figure 3.8: The values of surface alignment consistency (SAC) on a cortical surface. The surface is colored by the values of SAC using the color legend on the right side of (a).

To better visualize the variability of different anatomical region, the value of SAC is mapped onto the cortical surface of one subject. The vertex of the cortical surface is assigned with the SAC value according to its manual label. The mapped SAC on a cortical surface is shown as Fig. 3.8. The range of SAC across all 24 regions is from 0.24 to 0.71.

3.4 Surface Parcellation Using A Probabilistic Atlas

The surface parcellation performed by aligning the probabilistic atlas with the testing subject and then predicting the labels on the subject is applied on 14 subjects. The detail is described in Sec. 2.9 of Chap. 2. This section will first show results of using this method to automatically parcellate cortical surfaces of 14 subjects into 24 labels defined in Sec. 2.8. Then, to validate the robustness of this method, it is

(a) Manual Lateral   (b) Automated Lateral

(c) Manual Medial   (d) Automated Medial
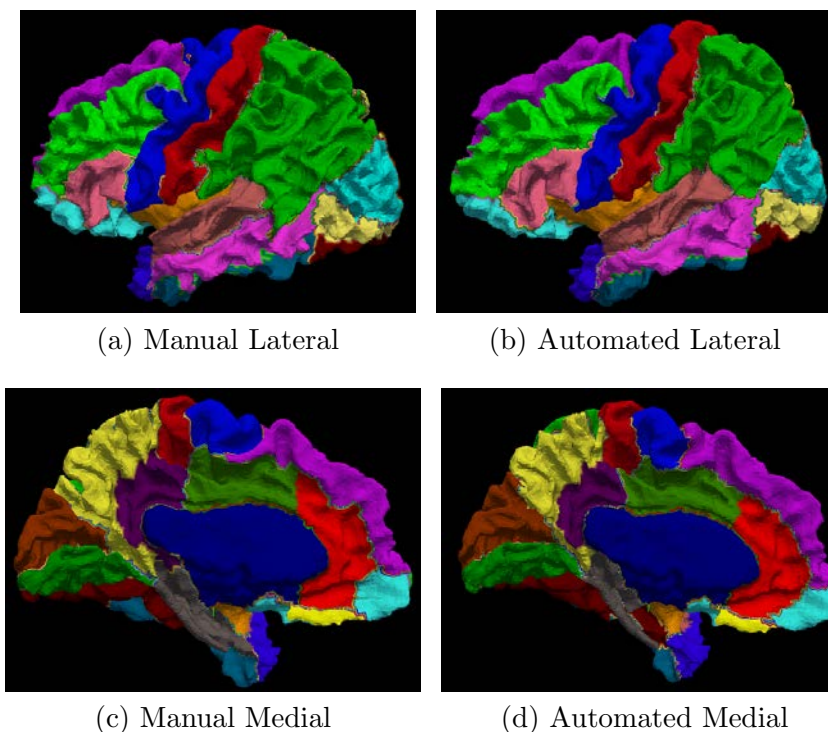
Figure 3.9: The most likely labels and the manual labels on one of the testing subject.The average Dice index between the manual labels and the automated labels across all of the regions is 0.87.

trained and tested with FreeSurfer's labels based on the same group of 49 subjects.

The automated labels that are generated using the most likely labels on one of 14 testing subjects are shown in Fig. 3.9. The manual labels for the same subject are also shown for the visual evaluation. The mean value of the Dice index for each label across 14 subjects is shown as the third column of Table 3.3, along with its standard deviation. Please refer to Table 2.8 on Page 133 for full names of the labels. The performance of the surface parcellation using only the most likely labels is done by choosing the label that has the highest agreement among training subjects. Geometry

(a) Mean Lateral   (b) Mean Medial

(c) SD Lateral   (d) SD Medial
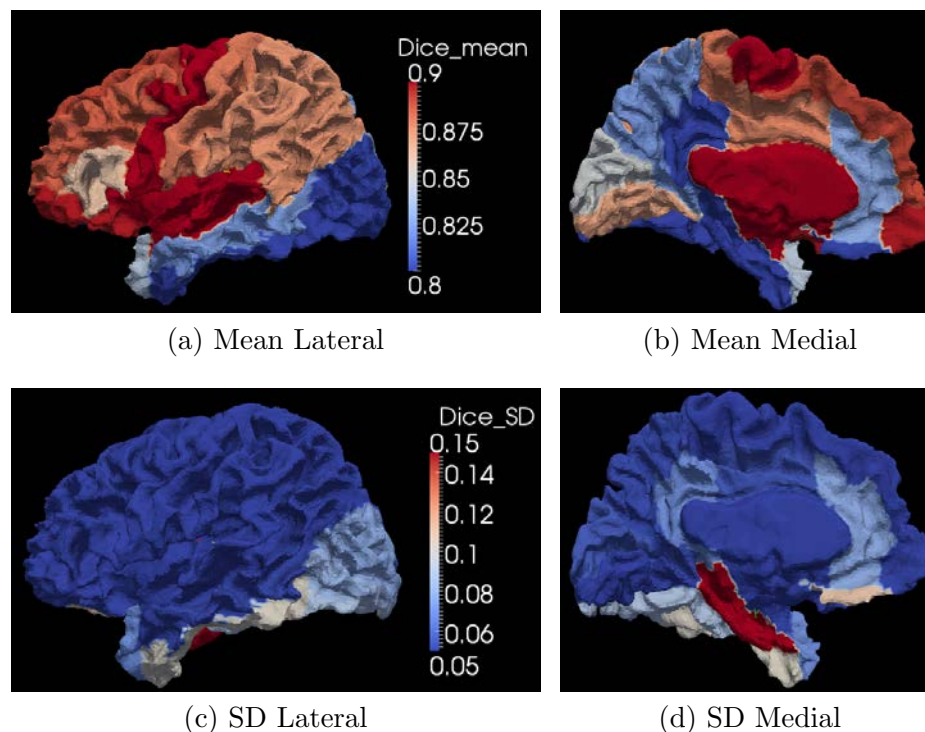
Figure 3.10: The mean and standard deviation of Dice indices across training subjects on one cortical surface. The surface is colored by the mean value (the first row) and the standard deviation (the second row) of the Dice index across 14 training subjects at the corresponding label. "SD" stands for the "Standard Deviation".

features such as "DistanceToPCIS/AP", "DistanceToHull", and "MeanCurvature" are used to align the atlas surface to the subject surface, before the most likely labels can be assigned to corresponding locations on the subject surface. It performs poorly at the place where there is no major folding pattern (sulci or gyri) to delineate the boundary. The average Dice index for each label and the standard deviation of it is mapped onto the cortical surface of one of the testing subjects, shown as Fig. 3.10. Here, manual labels are used to decide which label the Dice measurement corresponds to. From the figure, we can clearly see that the most likely labels produce relatively

weak similarities at the temporal lobe and the occipital lobe.

Table 3.3: Weighted Average Dice with Surface Area Ratio

Label Name	Surface Area (mm^2) (Ratio)	Dice (ML)	Weighted Dice (ML)	Dice (AD)	Weighted Dice(AD)
PA	9239 (.125)	.87($\pm$.04)	.109	.87($\pm$.03)	.109
MFG	5602 (.076)	.89($\pm$.04)	.066	.89($\pm$.04)	.066
PreCG	5495 (.074)	.90($\pm$.03)	.066	.90($\pm$.03)	.066
SFG	5223 (.070)	.89($\pm$.03)	.063	.89($\pm$.03)	.063
PoCG	5266 (.071)	.88($\pm$.04)	.062	.88($\pm$.03)	.062
OFC	3892 (.052)	.90($\pm$.02)	.047	.90($\pm$.02)	.047
STG	3322 (.045)	.90($\pm$.02)	.040	.90($\pm$.02)	.040
PreCuG	3278 (.044)	.82($\pm$.05)	.036	.82($\pm$.05)	.036
FU	3190 (.043)	.72($\pm$.09)	.031	.74($\pm$.08)	.030
UN	3030 (.041)	.93($\pm$.02)	.039	.93($\pm$.02)	.039
SLOG	2739 (.037)	.75($\pm$.08)	.028	.77($\pm$.08)	.029
LG	2699 (.036)	.87($\pm$.04)	.032	.87($\pm$.04)	.032
MTG	2573 (.035)	.82($\pm$.05)	.029	.82($\pm$.05)	.029
CU	2526 (.034)	.85($\pm$.06)	.029	.85($\pm$.06)	.029
IFG	2406 (.032)	.86($\pm$.04)	.028	.86($\pm$.04)	.028
IS	2021 (.027)	.91($\pm$.02)	.025	.91($\pm$.02)	.025
ITG	1972 (.027)	.76($\pm$.10)	.020	.78($\pm$.07)	.020
ILOG	2025 (.027)	.76($\pm$.08)	.020	.78($\pm$.08)	.021
ICiG	1659 (.022)	.88($\pm$.05)	.019	.88($\pm$.05)	.019
PHG	1699 (.023)	.76($\pm$.22)	.017	.79($\pm$.10)	.017
ACiG	1550 (.021)	.83($\pm$.08)	.018	.83($\pm$.07)	.018
TP	1201 (.016)	.84($\pm$.07)	.014	.84($\pm$.07)	.014
PoCiG	1149 (.015)	.79($\pm$.07)	.012	.79($\pm$.07)	.012
SG	395 (.005)	.78($\pm$.11)	.004	.77($\pm$.12)	.004
Average		.84	.86	.84	.86

ML: Most likely labels; AD: Adjusted labels. See Table 2.8 for abbreviations.

By comparing figures at the first row of Fig. 3.10 with Fig. 3.8, we can see both
of the surfaces share the same dark regions at the temporal lobe and the occipital

lobe. The first row of Fig. 3.10 shows the average Dice index of the most likely labels across 14 testing subjects mapped onto the corresponding labels defined by manual labels of the shown subject. Fig. 3.8 shows the SAC (surface alignment consistency) indices mapped onto corresponding regions. Each region has one SAC index. The index is used to quantify the consistency with which a parcel region was aligned on the atlas surface for 35 training surfaces. It is reasonable to think that the performance of the automated label is related with the consistency index of it in the training set. Fig. 3.11 shows the linear regression between two sets of values at the corresponding labels.
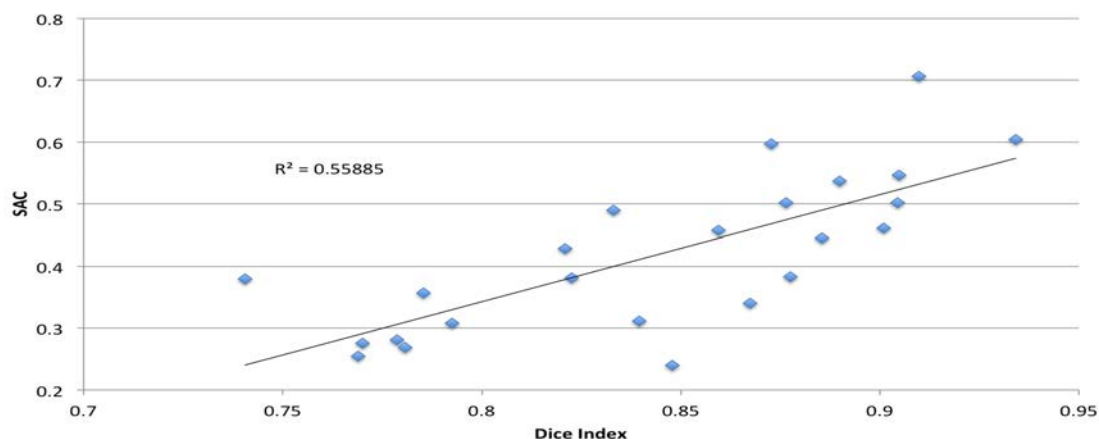
Figure 3.11: The linear regression between the Dice and SAC indices. The pair of the Dice index and SAC index for each label are shown as the scattered points in blue. There are 24 labels so there are 24 scattered points in the figure.

The surface area is believed to be another factor that can affect the performance of the surface parcellation[103]. We calculate the surface area for each manual

label on each training subject and then average the surface area for each label across 14 training subjects. A linear regression between the average Dice index and the average surface area for 24 labels is performed to show the correlation between them. The plot is shown in Fig. 3.12. The linear regression does not show strong correlation between them, with $R^2 = 0.19$. So, we can not simply assume that the region with small surface area will have bad Dice index and the region with big surface are will have good Dice index. For example, there are two red points in Fig. 3.12. The one below the line represent the region labeled as the straight gyrus. It has a relatively high Dice index because it's location is close to a geometric feature used in the registration, even though it has a relatively small surface area. The red point above the line in Fig. 3.12 represents the parietal region. It has the biggest surface area but its Dice index is not the highest one.
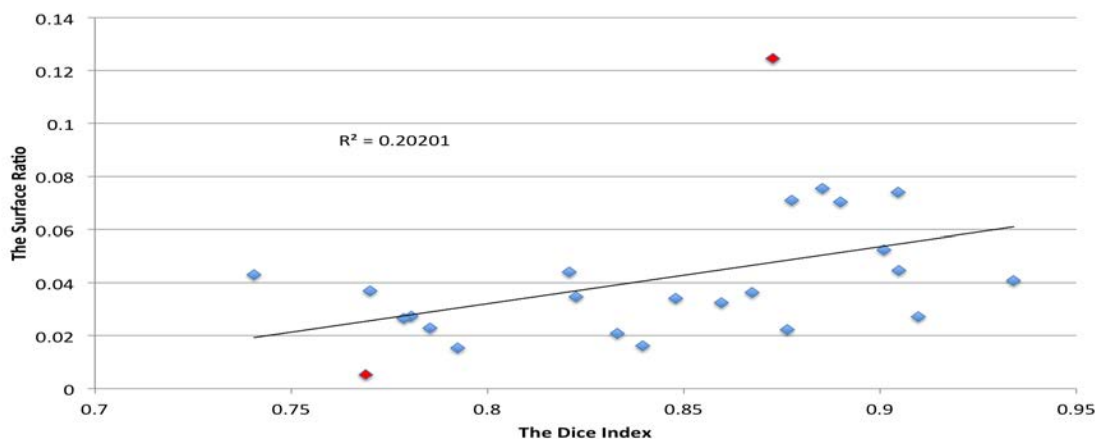
Figure 3.12: The linear regression between the Dice index and the surface area. The actual value that represents the surface area (vertical axis) of each label is the ratio of the average surface area across 14 subjects with the sum surface area across all labels and 14 subjects.

However, the surface area of a label can be used to weight the value of its Dice index when the average Dice index is needed for evaluating the similarity between automated labels and manual labels over the whole surface, such that not all regions are treated equally when an average Dice index is calculated across them. Table. 3.3 shows 24 parcellation labels in the descending order of surface area with the biggest region on the top. The second column of Table. 3.3 shows the average surface area in mm^2 for each label along with its ratio among all labels. The average surface area is calculated across 14 testing subjects according to their manual labels. The third column shows the average Dice index across 14 subjects comparing the similarity between the most likely label (marked as "ML" in the table) with the manual label, with the standard deviation of it. The column next to it shows the weighted Dice index which is the multiplication of the "Surface Area Ratio" and the "Dice" at the same row for each label. The sum of the "Weighted Dice (ML)" is the weighted average Dice for the most likely labels across 24 labels. The equation for calculating the weighted average Dice D_i^w over n labels is:

$$\text{Dice}_i^w = \sum_{i=0}^{n} r_i \text{Dice}_i \tag{3.1}$$

where $\sum_{i=0}^{n} r_i = 1.0$. r_i denotes the ratio of its surface area to the whole surface. Dice_i is used to denote the Dice index for label i.

The last two columns of Table 3.3 show the Dice indices and the weighted Dice indices for the automated labels after the adjustment is made based on the most likely labels. The details of the adjustment is describe in Sec. 2.9 of Chap. 2.

The improvement caused by the label adjustment is difficult to be seen in Table 3.3 because it lists all 24 labels but not all of them are adjusted. As mentioned in Sec. 2.9, the labels that are actually affected by the label adjustment are: PoCG, PA, SLOG, ILOG, FU, ITG, PHG, OFC, and ACiG. Table. 3.4 lists the mean and standard deviation (SD) of Dice indices for the most likely labels and for the adjusted labels when they are compared with the manual labels at those regions. It also lists the coefficient of variance (CV) of each of them. Because the adjustment is made based on the most likely labels, Dice indices for the most likely labels are simply mentioned as "Before Adjustment" in the table. The CV values of labels listed in Table 3.4 are demonstrated with columns in Fig. 3.13. The calculation of CV is shown as Eq. 2.57 on Page 147. By showing the CV values in columns, it is easy to detect the change made by the label adjustment on Dice indices. Big change can be seen at the PHG (parahippocampal gyrus) and the ITG (inferior temporal gyrus).

Table 3.4: Dice Indices of Most Likely Labels and Adjusted Labels

Label Name	Before Adjustment			After Adjustment		
	Mean	SD	CV(%)	Mean	SD	CV(%)
PA	.873	.037	4.21	.873	.028	3.21
FU	.723	.087	12.03	.741	.080	10.75
ACiG	.826	.077	9.29	.833	.065	7.83
ILOG	.762	.081	10.62	.780	.075	9.67
ITG	.758	.101	13.36	.779	.066	8.47
OFC	.898	.024	2.64	.901	.021	2.30
PHG	.759	.225	29.63	.785	.099	12.58
PoCG	.879	.037	4.21	.878	.025	3.21
SLOG	.749	.077	10.27	.770	.078	10.10
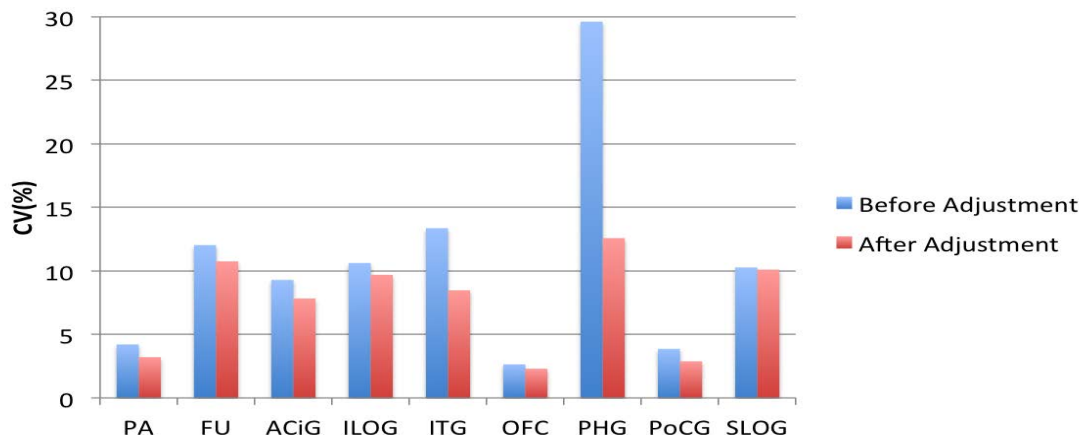
Figure 3.13: The comparison of CV before and after label adjustment at selected labels.

So far, we have been showing results for each label across subjects. Fig. 3.14 shows the evaluation of the automated surface parcellation for each subject across labels. The weight for each label is the ratio value shown within parentheses of the second column in Table 3.3. The values shown in Fig. 3.14 are from 0.83 to 0.88, with the median of 0.85.

The "point-wise parcellation error" which is calculated as the percentage of disagreement between the automated parcellation and the manual parcellation is shown on the template surface (see Fig. 3.15). Please see Sec. 2.9 for the detail of it. Fig. 3.15 shows that the majority of vertices are correctly labeled (with accuracy $> 75\%$), with the median accuracy at 92%, which is reported as 80% for the left hemisphere by FreeSurfer[65]. As we can see from Fig. 3.15, most errors (with accuracy $< 25\%$) occur at the boundary between labels at which there are also high variabilities for
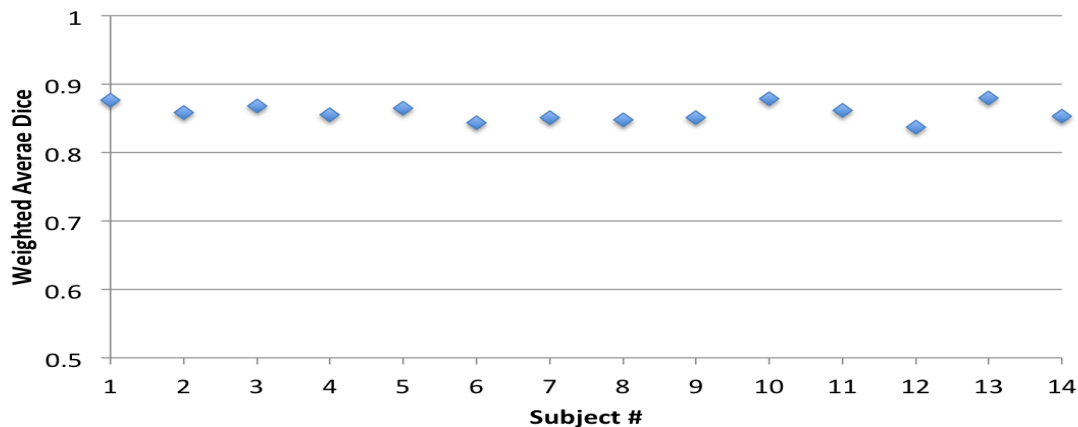
Figure 3.14: The scatter plot of the weighted average Dice for subjects.

manual labels.

(a) Latera Viewl   (b) Medial View
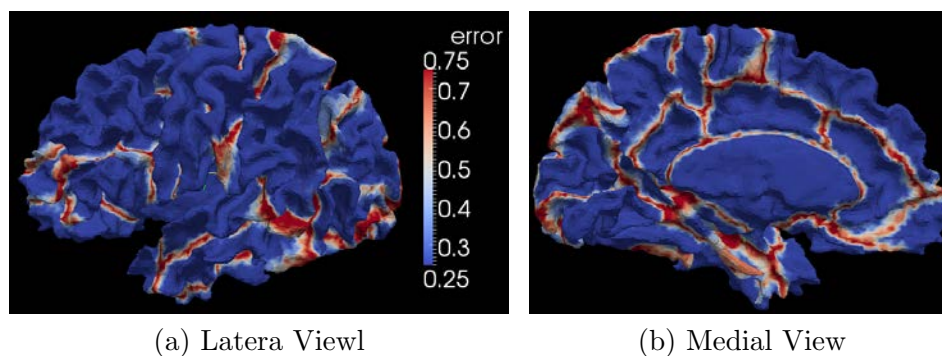
Figure 3.15: The point-wise parcellation error on the template surface. The color legend is given on the right side of (a).

The distribution of accuracy across 14 subjects for the left hemisphere is given

in Fig. 3.16. It is shown as the histogram of the percent correct on the AtlasIC7. The

value of the percent correct is the percentage of agreement between the automated

parcellation and the manual parcellation among 14 subjects at a vertex on the Atlas-sIC7. It can be calculated as 1.0 minus the value of "point-wise parcellation error". The original values along the y axis of Fig. 3.16 are the number of vertices on the AtlasIC7. It is converted to the "Percent of Surface" by dividing the number of vertices by the total number of vertices on AtlasIC7. From Fig. 3.16 shows that almost 60% of the surface is correct more than 90% time using the proposed automated surface parcellation. It is much higher than the value of 40% reported by FreeSurfer[65].
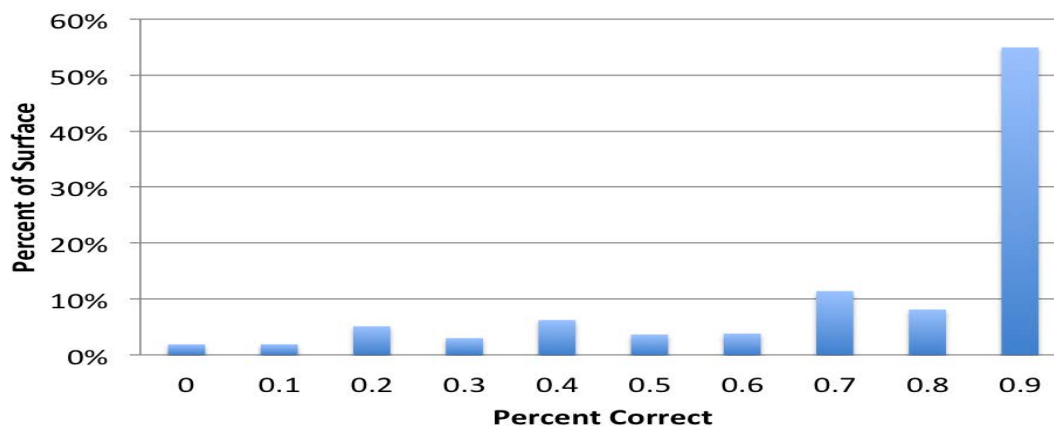
Figure 3.16: The histogram of the percent correct. The values along x axis are actually the minimum value of bins. "0" denotes the bin with a range of $[0, 0.1)$ and "0.1" denotes the bin with a range of $[0.1, 0.2)$, etc.

The accuracy of the parcellation is calculated for each subject, as the percentage of the number of correctly labeled points to the total number of points on the original cortical surface with two sets of labels (automated and manual). The scatter plot of the accuracy for 14 subjects is shown as Fig. 3.17. The accuracy in

14 testing subjects are from 82.3% to 87.8%, with the median accuracy of 85.6%. It is significantly higher than the median accuracy (78%) reported in a literature of the surface parcellation[65].
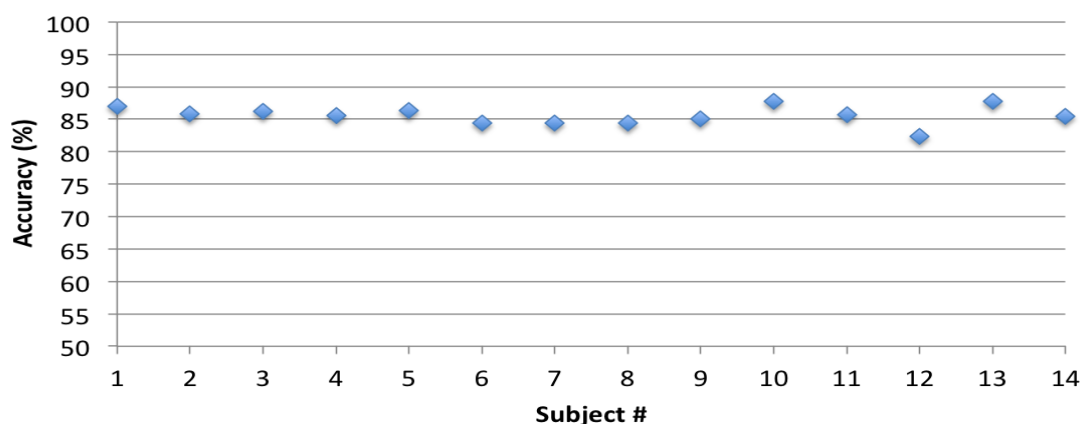
Figure 3.17: The scatter plot of the accuracy for 14 testing subjects.

To compare the surface area of regions that are parcellated by the automated labels and the manual labels, the mean and standard error of the surface area across 14 subjects at certain region is shown in Fig. 3.18. As can be seen, the surface area of two sets of labeling system (automated vs. manual) is close to each other, while the manual labeled regions have slightly bigger standard errors.

The overall Dice index across 34 regions and 14 subjects was about 0.81, with a median value of 0.86. For visual comparison, the parcellation labels generated from FreeSurfer (on the left) and from our method (on the right) mapped on the left cortical surface of a testing subject are shown in Fig. 3.19. It should be noted that
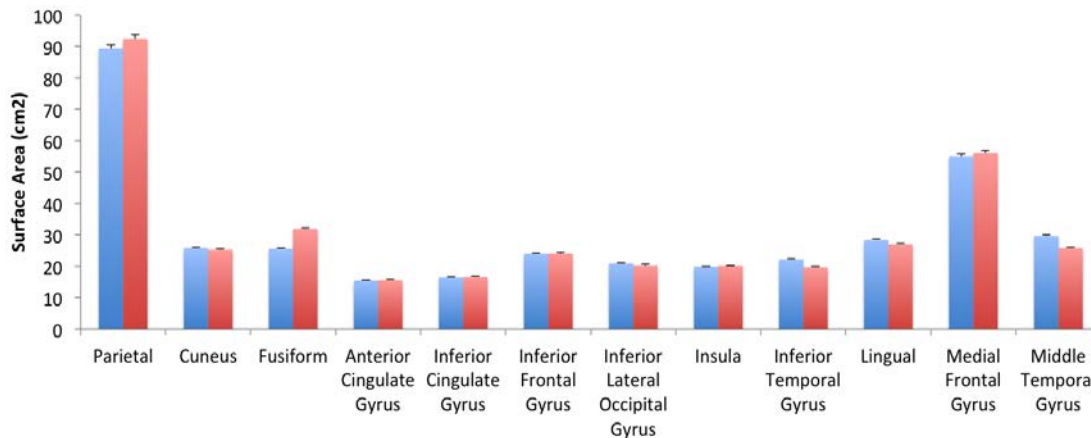
Figure 3.18: Comparison of mean and standard error of surface area at 12 parcellation regions. For each region, the left column shows the mean and standard error of the surface area with the automated label and the right column is for the manual label.

BRAINS processing takes approximately 1 hour to finish preprocessing and generate genus zero cortical surfaces for both hemispheres. The automated parcellation on each cortical surface takes approximately 2 hours. So it takes approximately 5 hours to finish the whole parcellation for both hemispheres on a macbook pro with a 2 GHz quad core CPU and a DDR3 RAM of 8GB. It is only 1/4 of the time that FreeSurfer needs to finish its process. The much shorter processing time allows us to be able to efficiently (fast and accurately) analyze data from a large population of subjects which is quite common in clinical data analysis.
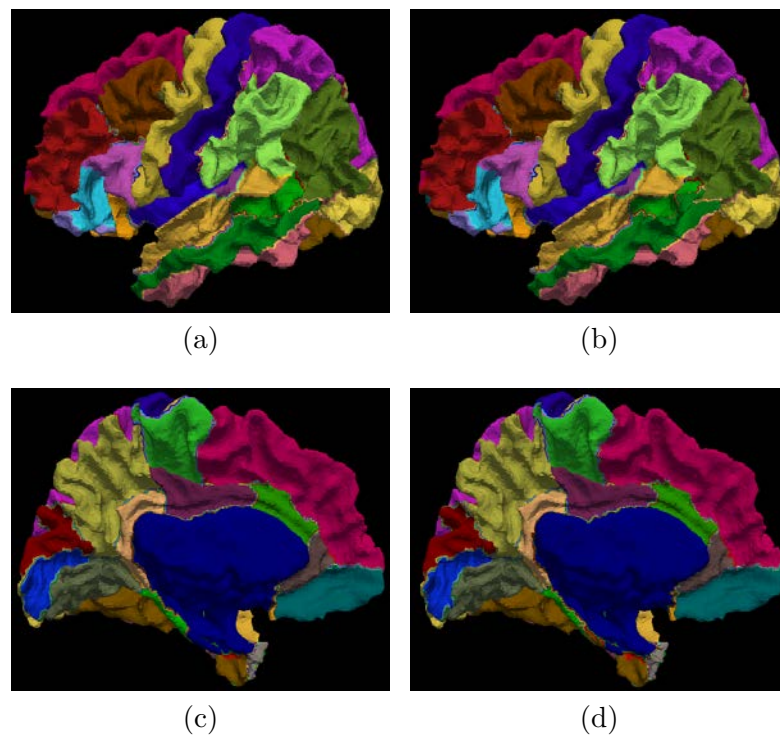
Figure 3.19: The visual comparison of the surface parcellaiton with FreeSurfer. (a) and (c) shows FreeSurfer labels in a lateral and medial view respectively. (b) and (d) shows BRAINS labels in a lateral and medical view respectively.

CHAPTER 4
DISCUSSION AND CONCLUSION

Automated parcellation of human cerebral cortex has a great potential to provide insight into the neurobiology of psychiatric diseases and response to the treatment. An efficient auomated parcellation system can not only save researchers and physicians from the labor-intensive process, and it provides a consistent delineation while avoiding rater drift and bias. Results presented in Chap. 3 show that the automated surface parcellation pipeline proposed in this dissertation can be used to assign different sets of labels to the cortical surface in an efficient and reliable way.

The implementation of rotational (rigid) registration and demons (deformable) registration in multi-resolution levels can not only speed up the procedure, it can also make it possible to use the combination of different geometry features to drive the registration between two cortical surfaces. Among geometry features used in co-registering surfaces, the first two, superior-inferior and anterior-posterior distance from PC point were able to provide the registration a good initial starting position, while the last two, distance from the surface to a convex hull and the mean curvature of the surface provided richer anatomical information about gyri and sulci patterns on the surface, and were used to register small anatomical features on the surface.

The method of generating the population atlas from training subjects is innovative and effective. Unlike some other groups' method, it does not need manual delineations[112] or iteratively updating the atlas[99][111]. The goal of constructing the population atlas for surface parcellation is to build the surface representation of

mean anatomical structures existing in a population of cerebral cortices. We did it by aligning other subjects in the training set to the first subject using pair-wise surface registration and averaging the measured geometry features in the spherical domain. By visualizing resulting average values on the template surface, we can see that, the measured value that is unique for the template itself is blurred out and only the values representing common geometry features is retained (see Fig. 3.5). Our population averaging is generated from a mixture of both controls and patients with a wide range of age, so it incorporates a wide range of anatomical variance of the cortical surfaces.

The cortical surface was delineated into 24 regions. The Dice index was used to evaluate the similarity between the automated label and the manual label. It was calculated using the surface area of regions delineated by both labels. Some regions have big surface areas. For example, the parietal covers %12.5 of the surface area on the cortical surface on average. Some regions have small surface area. For example, the straight gyrus covers only %0.5 of the surface area on the cortical surface. When we calculate the average Dice index across all regions, it may be biased on surface area, therefore we also calculated the weighted average based on surface area. The weighted average Dice metric was 0.86.

As for individual regions, the similarity index varies. Generally, regions having consistent boundaries and locations have higher Dice indices(see Fig. 3.10). However, it is not so related with the surface area of a particular region (see Fig. 3.12). It is also not directly related to surface flattening. Comparing Fig. 3.10 with Fig. 3.1, we can see lower Dice lobes (temporal and occipital) are compressed in the process of

surface flattening but the compression also happens at the frontal lobe, which has relatively higher Dice. The same situation can be observed at insula, with relatively high distortion but also high Dice index. The performance of at individual region is however, shown to be influenced by the proximity and the consistent anatomical information that is included in the features used for registration.

FreeSurfer is the only other software that can also perform automated parcellation on human cortical surfaces. The proposed method is shown to be able to give comparable results, but in a much shorter time. Both of the proposed method and the method in FreeSurfer can be used to automatically parcellate a cerebral cortex into anatomically and functionally meaningful regions on its surface. However, the two methods are fundamentally different in some major aspects:

- The surface generation is different (details are described in Sec. 2.3 and reference paper[107] respectively). Both of the surfaces are located in between the gray matter and white matter, but BRAINS3 surface has only 70,000 triangles and 35,002 vertices on it, which is about a quarter of the data size generated by FreeSurfer (298,392 triangles and 149,198 vertices).

- The surface flattening used to map a cortical surface into the spherical domain is different. Please see Sec. 2.5 and reference paper[107] for details of the method in BRAINS3 and the method in FreeSurfer respectively.

- The geometry features used to encode folding patterns at the cortical surface are different. The average convexity is calculated in FreeSurfer to represent folding patterns[99], while BRAINS3 incorporates four types of geometry features to

represent the locations and folding features for the patterns (please see Sec. 2.4 for details).

- The surface registration used to align cortical surfaces together in the spherical domain is different. FreeSurfer aligns two surfaces in the spherical domain by minimizing a cost function designed based on average convexities at vertices on spheres. BRAINS3 integrates the spherical demons registration proposed by Yeo[108] with rotational registration into a registration framework, which applies geometry features of the cortical surface from coarse to refined scale in implementing the registration in a multi-resolution manner (described in Sec. 2.6).

- The average atlas is constructed differently. FreeSurfer uses an iterative atlas building strategy to generate the population average[99]. BRAINS3 uses a single registration scheme (see Sec. 2.8).

- The probabilistic atlas is built differently. FreeSurfer calculates three types of probabilistic at each vertex on the atlas sphere[65], while BRAINS3 only calculates the first two (see Sec. 2.8). The reason is that the relationship of the measured value such as mean curvature with the boundary definitions of anatomical labels is not clear. And we think the distribution model of the measured value at each vertex for each label needs a further verification.

- After a new subject is aligned with the atlas, the classification of each vertex for that subject in the atlas space is different. FreeSurfer uses a Beysian classifier combined with MRF model[65]. BRAINS3 uses the prior probability of of labels

at each vertex in the training set to assign an initial label and then modify the initial classification based on the subject's curvature and neighborhood label prior information (details described in Sec. 2.8).

The most likely labels warped onto a subject's surface is adjusted by incorporating the subject's curvature information in re-evaluating some regions labels. Those regions are: parietal, fusiform, anterior cingulate gyrus, inferior lateral occipital gyrus, inferior temporal gyrus, orbital frontal cortex, parahippocampal gyrus, post-central gyrus, and superior lateral occipital gyrus. From Table 3.4, we can only detect mild increasement for the average Dice indices at the adjusted regions. A couple of regions even slide down (inferior temporal gyrus and fusiform). It shows that the adjustment method is lack of capability to catch the correct boundary for each subject because of the high inter-individual variability at that region. A more intelligent adjustment is required or a more sophisticated statistic model is need to improve label evaluations at those regions.

REFERENCES

[1] C.R. Noback, N.L. Strominger, R.J. Demarest, and D.A. Ruggiero, *The human nervous system structure and function*, Humana Press, Totowa, N.J., 6th edition, 2005.

[2] M.L. Jouandet, M.J. Tramo, D.M. Herron, A. Hermann, W.C. Loftus, J. Bazell, and M.S. Gazzaniga, "Brainprints: Computer-generated two-dimentional maps of the human cerebral cortex in vivo," *Journal of Cognitive Neuroscience*, vol. 1, pp. 88–117, 1989.

[3] K. Brodmann, *Vergleichende Lokalisationslehre der Grosshirnrinde in ihren Prinzipien dargestellt auf Grund des Zellenbaues*, Johann Ambrosius Barth Verlag, Leipzig, 1909.

[4] C. Economo and G.N. Koskinas, *Die Cytoarchitectonik der Hirnrinde des erwachsenen Menschen*, Springer, 1925.

[5] F. Sandies, "Structure and function of the human frontal lobe," *Neuropsychologia*, vol. 2, pp. 209–219, 1964.

[6] G.M. Edelman and V.B. Mountcastle, *The mindful brain*, MIT Press, Cambridge, M.A., 1978.

[7] A.R. Luria, *The working brain: an introduction to neuropsychology*, Basic Books, Allen Lane, London, 1973.

[8] B. Kolb and I.Q. Whishaw, *Fundamentals of human neuropsychology*, W. H. Freeman, San Francisco, 1980.

[9] S.G. Waxman, *Clinical neuroanatomy*, McGraw-Hill Medical, New York, NY, 26th edition, 2009.

[10] M.A. Rocca, A. Ceccarelli, A. Falini, B. Colombo, P. Tortorella, L. Bernasconi, G. Comi, G. Scotti, and M. Filippi, "Brain gray matter changes in migraine patients with T2-visible lesions: a 3-T MRI study," *Stroke*, vol. 37, pp. 1765–1770, 2006.

[11] M.S. Matharu, C.D. Good, A. May, A. Bahra, and P.J. Goadsby, "No change in the structure of the brain in migraine: a voxel-based morphometric study," *European Journal of Neurology*, vol. 10, pp. 53–57, 2003.

[12] C.D. Good, I.S. Johnsrude, J. Ashburner, R.N.A. Henson, K.J. Fristen, and R.S.J. Frackowiak, "A voxel-based morphometric study of ageing in 465 normal adult human brains," *NeuroImage*, vol. 14, pp. 21–36, 2001.

[13] J.D. Bartleson and F.M. Cutrer, "Migraine update. diagnosis and treatment," *Minnesota Medicine*, vol. 93, pp. 36–41, 2010.

[14] F.M. Cutrer, "Pathophysiology of migraine," *Seminars in Neurology*, vol. 30, pp. 120–130, 2010.

[15] C. Weiller, A. May, V. Limmroth, M. Juptner, H. Kaube, R. V. Schayck, H.H. Coenen, and H.C. Diener, "Brain stem activation in spontaneous human migraine attacks," *Nature Medicine*, vol. 1, pp. 658–660, 1995.

[16] A. May, J. Ashburner, C. Buchel, D.J. McGonigle, K.J. Friston, R.S.J. Frackowiak, and P.J. Goadsby, "Correlation between structural and functional changes in brain in an idiopathic headache syndrome," *Nature Medicine*, vol. 5, pp. 836–838, 1999.

[17] T. Schmidt-Wilcke, E. Leinisch, A. Straube, N. Kampfe, B. Draganski, H.C. Diener, U. Bogdahn, and A. May, "Gray matter decrease in patients with chronic tension type headache," *Neurology*, vol. 65, pp. 1483–1486, 2005.

[18] H. Brody, "Organization of the cerebral cortex. III. a study of aging in the human cerebral cortex," *Journal of Comparative Neurology*, vol. 102, pp. 511–516, 1955.

[19] V.A. Magnotta, N.C. Andreasen, S.K. Schultz, G. Harris, T. Cizadlo, D. Heckel, P. Nopoulos, and M. Flaum, "Quantitative in vivo measurement of gyrification in the human brain: changes associated with aging," *Cerebral Cortex*, vol. 9, pp. 151–160, 1999.

[20] C.E. Coffey, J.F. Lucke, J.A. Saxton, G. Ratcliff, L.J. Unitas, and R.N. Bryan, "Sex differences in brain aging: a quantitative magnetic resonance imaging study," *Archives of Neurology*, vol. 55, pp. 169–179, 1998.

[21] K.L. Double, G.M. Halliday, J.J. Krill, J.A. Harasty, K. Cullen, W.S. Brooks, H. Creasey, and G.A. Broe, "Topography of brain atrophy during normal aging and Alzheimer's disease," *Neurobiology of Aging*, vol. 17, pp. 513–521, 1996.

[22] C. DeCarli, J.A. Kaye, B. Horwitz, and S.I. Rapoport, "Critical analysis of the use of computer-assisted transverse axial tomography to study human brain in aging and dementia of the Alzheimer type," *Neurology*, vol. 40, pp. 872–883, 1990.

[23] J.P. Kesslak, O. Nalcioglu, and C.W. Cotman, "Quantification of magnetic resonance scans for hippocampal and parahippocampal atrophy in Alzheimer's disease," *Neurology*, vol. 41, pp. 51–54, 1991.

[24] C.R. Jack Jr., R.C. Petersen, P.C. O'Brien, and E.G. Tangalos, "MR-based hippocampal volumetry in the diagnosis of Alzheimer's disease," *Neurology*, vol. 42, pp. 183–188, 1992.

[25] S. Lehericy, M. Baulac, J. Chiras, L. Pierot, N. Martin, B. Pillon, B. Deweer, B. Dubois, and C. Marsault, "Amygdalohippocampal MR volume measurements in the early stages of Alzheimer disease," *American Journal of Neuroradiology*, vol. 15, pp. 929–937, 1994.

[26] M.P. Laakso, H. Soininen, K. Partanen, E.L. Helkala, P. Hartikainen, P. Vainio, M. Hallikainen, T. Hänninen, and P.J.Sr. Riekkinen, "Volumes of hippocampus, amygdala and frontal lobes in the MRI-based diagnosis of early Alzheimer's disease: correlation with memory functions," *Journal of Neural Transmission: Parkinson's Disease and Dementia Section*, vol. 9, pp. 73–86, 1995.

[27] H.S. Soininen, K. Partanen, A. Pitkänen, P. Vainio, T. Hänninen, M. Hallikainen, K. Koivisto, and P.J.Sr. Riekkinen, "Volumetric MRI analysis of the amygdala and the hippocampus in subjects with age-associated memory impairment: correlation to visual and verbal memory," *Neurology*, vol. 44, pp. 1660–1668, 1994.

[28] G.D. Pearlson, G.J. Harris, R.E. Powers, P.E. Barta, E.E. Camargo, G.A. Chase, J.T. Noga, and L.E. Tune, "Quantitative changes in mesial temporal volume, regional cerebral blood flow, and cognition in Alzheimer's disease," *Archives of General Psychiatry*, vol. 49, pp. 402–408, 1992.

[29] R.J. Killiany, M.B. Moss, M.S. Albert, T. Sandor, J. Tieman, and F. Jolesz, "Temporal lobe regions on magnetic resonance imaging identify patients with early Alzheimer's disease," *Archives of Neurology*, vol. 50, pp. 949–954, 1993.

[30] A. Convit, M.J. de Leon, J. Golomb, A.E. George, C.Y. Tarshish, M. Bobinski, W. Tsui, S. De Santi, J. Wegiel, and H. Wisniewski, "Hippocampal atrophy in early Alzheimer's disease: anatomic specificity and validation," *The Psychiatric Quarterly*, vol. 64, pp. 371–387, 1993.

[31] A. Convit, M.J. de Leon, C. Tarshish, S. De Santi, A. Kluger, H. Rusinek, and A.E. George, "Hippocampal volume losses in minimally impaired elderly," *The Lancet*, vol. 345, pp. 266, 1995.

[32] B.C. Dickerson, I. Goncharova, M.P. Sullivan, C. Forchetti, R.S. Wilson, D.A. Bennett, L.A. Beckett, and L. deToledo Morrell, "MRI-derived entorhinal and hippocampal atrophy in incipient and very mild Alzheimer's disease," *Neurobiology of Aging*, vol. 22, pp. 747–754, 2001.

[33] N.C. Fox, E.K. Warrington, P.A. Freeborough, P. Hartikainen, A.M. Kennedy, J.M. Stevens, and M.N. Rossor, "Presymptomatic hippocampal atrophy in Alzheimer's disease: a longitudinal MRI study," *Brain*, vol. 119, pp. 2001–2007, 1996.

[34] M.P. Laakso, K. Partanen, P.Jr. Riekkinen, M. Lehtovirta, E.L. Helkala, M. Hallikainen, T. Hänninen, P. Vainio, and H. Soininen, "Hippocampal volumes in Alzheimer's disease, Parkinson's disease with and without dementia and in vascular dementia: An MRI study," *Neurology*, vol. 46, pp. 678–681, 1996.

[35] J.P. Seab, W.J. Jagust, S.T.S. Wong, M.S. Roos, B.R. Reed, and T.F. Budinger, "Quantitative NMR measurements of hippocampal atrophy in Alzheimer's disease," *Magnetic Resonance in Medicine*, vol. 8, pp. 200–208, 1988.

[36] N.C. Andreasen, "Negative symptoms in schizophrenia: definition and reliability," *Archives of General Psychiatry*, vol. 39, pp. 784–788, 1982.

[37] T.E. Goldberg, J.R. Kelsoe, D.R. Weinberger, N.H. Pliskin, P.D. Kirwin, and K.F. Berman, "Performance of schizophrenic patients on putative neuropsychological tests of frontal lobe function," *International Journal of Neuroscience*, vol. 42, pp. 51–58, 1988.

[38] K. Kleist, "Schizophrenic symptoms and cerebral pathology," *British Journal of Psychiatry*, vol. 106, pp. 246–255, 1960.

[39] W.M. Perlstein, C.S. Carter, D.C. Noll, and J.D. Cohen, "Relation of prefrontal cortex dysfunction to working memory and symptoms in schizophrenia," *The American Journal of Psychiatry*, vol. 158, pp. 1105–1113, 2001.

[40] N.C. Andreasen, S.A. Olsen, J.W. Dennert, and M.R. Smith, "Ventricular enlargement in schizophrenia: relationship to positive and negative symptoms," *The American Journal of Psychiatry*, vol. 139, pp. 297–302, 1982.

[41] N.C. Andreasen, "Brain imaging: applications in psychiatry," *Science*, vol. 239, pp. 1381–1388, March 1988.

[42] I.C. Wright, S. Rabe-Hesketh, P.W.R. Woodruff, A.S. David, R.M. Murray, and E.T. Bullmore, "Meta-analysis of regional brain volumes in schizophrenia," *The American Journal of Psychiatry*, vol. 157, pp. 16–25, 2000.

[43] K.E. Ward, L. Friedman, A. Wise, and S.C. Schulz, "Meta-analysis of brain and cranial size in schizophrenia," *Schizophrenia Research*, vol. 22, pp. 197–213, 1996.

[44] S.M. Lawrie and S.S. Abukmeil, "Brain abnormality in schizophrenia. a systematic and quantitative review of volumetric magnetic resonance imaging studies," *The British Journal of Psychiatry*, vol. 172, pp. 110–120, 1998.

[45] J.M. Goldstein, J.M. Goodman, J. Seidman, L, D.N. Kennedy, N. Makris, H. Lee, J. Tourville, V.S. Caviness, S.V. Faraone, and M.T. Tsuang, "Cortical abnormalities in schizophrenia identified by structural magnetic resonance imaging," *Archives of General Psychiatry*, vol. 56, pp. 537–547, 1999.

[46] H. Yamasue, A. Iwanami, Y. Hirayasu, H. Yamada, O. Abe, N. Kuroki, R. Fukuda, K. Tsujii, S. Aoki, K. Ohtomo, N. Kato, and K. Kasai, "Localized volume reduction in prefrontal, temporolimbic, and paralimbic regions in schizophrenia: an MRI parcellation study," *Psychiatry Research*, vol. 131, pp. 195–207, 2004.

[47] G. Donohoe, T. Frodl, D. Morris, I. Spoletini, D.M. Cannon, A. Cherubini, C. Caltagirone, P. Bossù, C. McDonald, M. Gill, A.P. Corvin, and G. Spalletta, "Reduced occipital and prefrontal brain volumes in dysbindin-associated schizophrenia," *Neuropsychopharmacology*, vol. 35, pp. 368–373, 2010.

[48] NINDS and NIH, "Parkinson's disease," `http://www.ninds.nih.gov/disorders/parkinsons_disease/parkinsons_disease.htm`, 2011.

[49] J.P. Lefaucheur, "Motor cortex dysfunction revealed by cortical excitability studies in Parkinson's disease: influence of antiparkinsonian treatment and cortical stimulation," *Clinical Neurophysiology*, vol. 116, pp. 244–253, 2005.

[50] E.J. Burton, I.G. McKeith, D.J. Burn, E.D. Williams, and J.T. O'Brien, "Cerebral atrophy in Parkinson's disease with and without dementia: a comparison with Alzheimer's disease, dementia with lewy bodies and controls," *Brain*, vol. 127, pp. 791–800, 2004.

[51] F.O. Walker, "Huntington's disease," *Seminars in Neurology*, vol. 27, pp. 218–228, 2007.

[52] S.M. de la Monte, J.P. Vonsattel, and E.P.Jr. Richardson, "Morphometric demonstration of atrophic changes in the cerebral cortex, white matter, and neostriatum in Huntington's disease," *Journal of Neuropathology and Experimental Neurology*, vol. 47, pp. 516–525, 1988.

[53] S.M. Henley, E.J. Wild, N.Z. Hobbs, C. Frost, D.G. MacManus, R.A. Barker, N.C. Fox, and S.J. Tabrizi, "Whole-brain atrophy as a measure of progression in premanifest and early Huntington's disease," *Movement Disorders*, vol. 24, pp. 932–936, 2009.

[54] F. Squitieri, M. Cannella, M. Simonelli, J. Sassone, T. Martino, E. Venditti, A. Ciammola, C. Colonnese, L. Frati, and A. Ciarmiello, "Distinct brain volume changes correlating with clinical stage, disease progression rate, mutation size, and age at onset prediction as early biomarkers of brain atrophy in Huntington's disease," *CNS Neuroscience Therapeutics*, vol. 15, pp. 1–11, 2009.

[55] N.Z. Hobbs, J. Barnes, C. Frost, S.M.D. Henley, E.J. Wild, K. MacDonald, R.A. Barker, R.I. Scahill, N.C. Fox, and S.J. Tabrizi, "Onset and progression of pathologic atrophy in Huntington disease: A longitudinal MR imaging study," *Brain*, vol. 31, pp. 1036–1041, 2010.

[56] E.H. Aylward, P.C. Nopoulos, C.A. Ross, D.R. Langbehn, R.K. Pierson, J.A. Mills, H.J. Johnson, V.A. Magnotta, A.R. Juhl, and J.S. Paulsen, "Longitudinal change in regional brain volumes in prodromal Huntington disease," *Journal of Neurology, Neurosurgery and Psychiatry with practical neurology*, vol. 82, pp. 405–410, 2010.

[57] P.C. Nopoulos, E.H. Aylward, C.A. Ross, H.J. Johnson, V.A. Magnotta, A.R. Juhl, R.K. Pierson, J. Mills, D.R. Langbehn, and J.S. Paulsen, "Cerebral cortex structure in prodromal Huntington disease," *Neurobiology of Disease*, vol. 40, pp. 544–554, 2010.

[58] F. Di Salle, F. Esposito, A. Elefante, T. Scarabino, A. Volpicelli, S. Cirillo, R. Elfante, and E. Seifritz, "High field functional MRI," *European journal of radiology*, vol. 48, pp. 138–145, 2003.

[59] W. van der Zwaag, S. Francis, K. Head, A. Peters, P. Gowland, P. Morris, and R. Bowtell, "fMRI at 1.5, 3 and 7 T: characterising BOLD signal changes.," *Neuroimage*, vol. 47, pp. 1425–1434, 2009.

[60] A. Gholipour, N. Kehtarnavaz, R. Briggs, M. Devous, and K. Gopinath, "Brain functional localization: a survey of image registration techniques," *IEEE Transactions on Medical Imaging*, vol. 26, pp. 427–451, 2007.

[61] N. Tzourio-Mazoyer, B. Landeau, D. Papathanassiou, F. Crivello, O. Etard, N. Delcroix, B. Mazoyer, and M. Joliot, "Automated anatomical labeling of activations in spm using a macroscopic anatomical parcellation of the MNI MRI single-subject brain," *NeuroImage*, vol. 15, pp. 273–289, 2002.

[62] P.E. Roland and K. Zilles, "Structural divisions and functional fields in the human cerebral cortex," *Brain Research Reviews*, vol. 26, pp. 87–105, 1998.

[63] N. Tzourio, L. Petit, E. Mellet, C. Orssaud, F. Crivello, K. Benali, G. Salamon, and B. Mazoyer, "Use of anatomical parcellation to catalog and study structure-function relationships in the human brain," *Human Brain Mapping*, vol. 5, pp. 228–232, 1997.

[64] P. Jannin, X. Morandi, O.J. Fleig, E.L. Rumeur, P. Toulouse, B. Gibaud, and J. M. Scarabin, "Integration of sulcal and functional information for multimodal neuronavigation," *Journal of Neurosurgery*, vol. 96, pp. 713–723, 2002.

[65] B. Fischl, A. van der Kouwe, C. Destrieux, E. Halgren, F. Ségonne, D.H. Salat, E. Busa, L.J. Seidman, J. Goldstein, D. Kennedy, V. Caviness, N. Makris, B. Rosen, and A.M. Dale, "Automatically parcellating the human cerebral cortex," *Cerebral Cortex*, vol. 14, pp. 11–22, 2004.

[66] J. Rademacher, A.M. Galaburda, D.N. Kennedy, P.A. Filipek, and V.S. Caviness, "Human cerebral cortex: localization, parcellation, and morphometry with magnetic resonance imaging," *Journal of Cognitive Neuroscience*, vol. 4, pp. 352–374, 1992.

[67] B. Crespo-Facorro, J.J. Kim, N.C. Andreasen, D.S. O'Leary, A.K. Wiser, J.M. Bailey, G. Harris, and V.A. Magnotta, "Human frontal cortex: an MRI-based parcellation method," *Neuroimaging*, vol. 10, pp. 500–519, 1999.

[68] J.J. Kim, B. Crespo-Facorro, N.C. Andreasen, D.S. O'Leary, B. Zhang, G. Harris, and V.A. Magnotta, "An MRI-based temporal lobe parcellation," *Neuroimaging*, vol. 11, pp. 271–288, 2000.

[69] B. Crespo-Facorro, J.J. Kim, N.C. Andreasen, R. Spinks, D.S. O'Leary, H.J. Bockholt, G. Harris, and V.A. Magnotta, "Cerebral cortex: a topographic segmentation method using magnetic resonance imaging," *Psychiatry Research: Neuroimaging*, vol. 100, pp. 97–126, 2000.

[70] B. Fischl, D.H. Salat, E. Busa, M. Albert, M. Dieterich, C. Haselgrove, A. van der Kouwe, R. Killiany, D. Kennedy, S. Klaveness, A. Montillo, N. Makris, B. Rosen, and A.M. Dale, "Whole brain segmentation: automated labeling of neuroanatomical structures in the human brain," *Neuron*, vol. 33, pp. 341–355, 2002.

[71] G. Lohmann and D.Y. von Cramon, "Automatic labeling of the human cortical surface using sulcal basins," *Medical Image Analysis*, vol. 4, pp. 179–188, 2000.

[72] M. E. Rettmann, X. Han, C. Xu, and J. L. Prince, "Automated sulcal segmentation using watersheds on the cortical surface," *NeuroImage*, vol. 15, pp. 329–344, 2002.

[73] G. Li, L. Guo, J. Nie, and T. Liu, "Automatic cortical sulcal parcellation based on surface principal direction flow field tracking," *NeuroImage*, vol. 46, pp. 923–937, 2009.

[74] A.W. Toga and P.M. Thompson, "The role of image registration in brain mapping," *Image And Vision Computing*, vol. 19, pp. 3–24, 2001.

[75] J. Talairach and P. Tournoux, *Co-Planar Stereotaxic Atlas of the Human Brain*, Thieme Publishing Group, 1st edition, 1988.

[76] M. Brett, I.S. Johnsrude, and A.M. Owen, "the problem of functional localization in the human brain," *Nature Reviews Neuroscience*, vol. 3, pp. 243–249, 2002.

[77] N.C. Andreasen, R. Rajarethinam, T. Cizadol, S. Arndt, V.W.II Swayze, L.A. Flashman, D.S. O'Leary, J.C. Ehrhardt, and W.T.C. Yuh, "Automatic atlas-based volume estimation of human brain regions from MR images," *Journal of Computer Assisted Tomography*, vol. 20, pp. 98–106, 1996.

[78] J.L. Lancaster, L.H. Rainey, J.L. Summerlin, C.S. Freitas, P.T. Fox, A.C. Evans, A.W. Toga, and J.C. Mazziotta, "Automated labeling of the human brain: a preliminary report on the development and evaluation of a forward-transform method," *Human Brain Mapping*, vol. 5, pp. 238–242, 1997.

[79] J.L. Lancaster, M.G. Woldorff, L.M. Parsons, M. Liotti, C.S. Freitas, L. Rainey, P.V. Kochunov, D. Nickerson, S.A. Mikiten, and P.T. Fox, "Automated talairach atlas labels for functional brain mapping," *Human Brain Mapping*, vol. 10, pp. 120–131, 2000.

[80] D.L. Collins, P. Neelin, T.M. Peters, and A.C. Evans, "Automatic 3D inter-subject registration of MR volumetric data in standardized Talairach space," *Journal of Computer Assisted Tomography*, vol. 18, pp. 192–205, 1994.

[81] D.L. Collins, T.M. Peters, and A.C. Evans, "An automated 3D non-linear image deformation procedure for determination of gross morphometric variability in human brain," in *Proceedings of Conference on Visualization in Biomedical Computing*, 1994, vol. SPIE 2359, pp. 180–190.

[82] D.L. Colins, C.J. Holmes, T.M. Peters, and A.C. Evans, "Automatic 3-d model-based neuroanatomical segmentation," *Human Brain Mapping*, vol. 3, pp. 190–208, 1995.

[83] J. Rademacher, V.S. Caviness, H. Steinmetz, and A.M. Galaburda, "Topographical variation of the human primary cortices: implications for neuroimaging, brain mapping, and neurobiology," *Cerebral cortex*, vol. 3, pp. 313–329, 1993.

[84] G. Rajkowska and P.S. Goldman-Rakic, "Cytoarchitectonic definition of prefrontal areas in the normal human cortex. II. variability in the locations of areas 9 and 46 and relationship to the talairach coordinates system," *Cerebral cortex*, vol. 5, pp. 323–337, 1995.

[85] K. Zilles, E. Amstrong, A. Schleicher, and H.J. Kretschmann, "The human pattern of gyrification in the cerebral cortex," *Anatomy and Embryology*, vol. 179, pp. 173–179, 1988.

[86] M. Ono, S. Kubik, and C.D. Abemathey, *Atlas of The Cerebral Sulci*, Thieme Medical Publishers, Inc., New York, NY, 1st edition, 1990.

[87] P.M. Thompson, C. Schwartz, R.T. Lin, A.A. Khan, and A.W. Toga, "Three-dimensional statistical analysis of sulcal variability in the human brain," *The Journal of Neuroscience*, vol. 16, pp. 4261–4274, 1996.

[88] P.E. Roland and K. Zilles, "Brain atlases - a new research tool," *Trends in Neurosicences*, vol. 17, pp. 458–467, 1994.

[89] D.C. Van Essen, "Windows on the brain: the emerging role of atlases and databases in neuroscience," *Current Opinion in Neurobiology*, vol. 12, pp. 574–579, 2002.

[90] R. Bajcsy, "Digital anatomy atlas and its registration to MRI, fMRI, PET: the past presents a future," *Lecture Notes in Computer Science*, vol. 2717, pp. 201–211, 2003.

[91] M.I. Miller, G.E. Christensen, Y. Amit, and U. Grenander, "Mathematical text-book of deformable neuroanatomies," in *Proceedings of the National Academy of Sciences of the United States of America*, 1993, vol. 90, pp. 11944–11948.

[92] D.V. Iosifescu, M.E. Shenton, S.K. Warfield, R. Kikinis, J. Dengler, F.A. Jolesz, and R.W. McCarley, "An automated registration algorithm for measuring MRI subcortical brain structures," *NeuroImage*, vol. 6, pp. 13–25, 1997.

[93] R.A. Heckemann, J.V. Hajnal, P. Aljabar, D. Rueckert, and A. Hammers, "Automatic anatomical brain MRI segmentation combining label propagation and decision fusion," *NeuroImage*, vol. 33, pp. 115–126, 2006.

[94] M.R. Sabuncu, B.T.T. Yeo, K. Van Leemput, B. Fischl, and P. Golland, "A generative model for image segmentation based on label fusion," *IEEE Transactions on medical imaging*, vol. 29, pp. 1714–1729, 2010.

[95] R.A. Heckemann, S. Keihaninejad, P. Aljabar, D. Rueckert, J.V. Hajnal, and A. Hammers, "Improving intersubject image registration using tissue-class information benefits robustness and accuracy of multi-atlas based anatomical segmentation," *NeuroImage*, vol. 51, pp. 221–227, 2010.

[96] R.A. Heckemann, S. Keihaninejad, P. Aljabar, K.R. Gray, C. Nielsen, D. Rueckert, J.V. Hajnal, and A. Hammers, "Automatic morphometry in alzheimer's disease and mild cognitive impairment," *NeuroImage*, 2011, in press.

[97] V.L. Towle, L. Khorasani, S. Uftring, C. Pelizzari, R. K. Erickson, J. P. Spire, K. Hoffmann, D. Chu, and M. Scherg, "Noninvasive identification of human central sulcus: a comparison of gyral morphology, functional MRI, dipole localization, and direct cortical mapping," *NeuroImage*, vol. 19, pp. 684–697, 2003.

[98] D.C. Van Essen, H.A. Drury, S. Joshi, and M. Miller, "Functional and structural mapping of human cerebral cortex: solutions are in the surfaces," in *Proceedings of the National Academy of Sciences of the United States of America*, 1998, vol. 95, pp. 788–795.

[99] B. Fischl, M.I. Sereno, R.B.H. Tootell, and A.M. Dale, "High-resolution inter-subject averaging and a coordinate system for the cortical surface," *Human Brain Mapping*, vol. 8, pp. 272–284, 1999.

[100] M. Özcan, U. Baumgärtner, G. Vucurevic, P. Stoeter, and R.-D Treede, "Spatial resolution of fMRI in the human parasylvian cortex: comparison of somatosensory and auditory activation," *NeuroImage*, vol. 25, pp. 877–887, 2005.

[101] B. Fischl and A.M. Dale, "Measuring the thickness of the human cerebral cortex from magnetic resonance images," in *Proceedings of the national academy of sciences of the United States of America*, 2000, vol. 97, pp. 11050–11055.

[102] L.T. Eyler, E. Prom-Wormley, M.S. Panizzon, A.R. Kaup, C. Fennema-Notestine, M.C. Neale, T.L. Jernigan, B. Fischl, C. E. Franz, M.J. Lyons, M. Grant, A. Stevens, J. Pacheco, M.E. Perry, J.E. Schmitt, L.J. Seidman, H.W. Thermenos, M.T. Tsuang, C-H. Chen, W.K. Thompson, A. Jak, A.M. Dale, and W.S. Kremen, "Genetic and environment contributions to regional cortical surface area in humans: a magnetic resonance imaging twin study," *Cerebral Cortex*, vol. missing, pp. missing, 2011.

[103] R.S. Desikan, F. Sgonne, B. Fischl, B.T. Quinn, B.C. Dickerson, D. Blacker, R.L. Buckner, A.M. Dale, R.P. Maguire, B.T. Hyman, M.S. Albert, and R.J. Killiany, "An automated labeling system for subdividing the human cerebral cortex on mri scans into gyral based regions of interest," *NeuroImage*, vol. 31, pp. 968–980, 2006.

[104] B. Fischl, A. Liu, and A.M. Dale, "Automated manifold surgery: constructing geometrically accurate and topologically correct models of the human cerebral cortex," *IEEE Transaction on Medical Imaging*, vol. 20, pp. 70–80, 2001.

[105] F. Ségonne, E. Grimson, and B. Fischl, "A genetic algorithm for the topology correction of cortical surfaces," *Inf. Process. Med. Imag.*, vol. 19, pp. 393–405, 2005.

[106] A.M. Dale, B. Fischl, and M.I. Sereno, "Cortical surface-based analysis i: segmentation and surface reconstruction," *NeuroImage*, vol. 9, pp. 179–194, 1998.

[107] B. Fischl, M.I.Sereno, and A.M. Dale, "Cortical surface-based analysis ii: inflation, flattening, and a surface-based coordinate system," *NeuroImage*, vol. 9, pp. 195–207, 1999.

[108] B.T.T. Yeo, M.R. Sabuncu, T. Vercauteren, N. Ayache, B. Fischl, and P. Golland, "Spherical demons: Fast diffeomorphic landmark-free surface registration," *IEEE Transactions on Medical Imagings*, vol. 29, pp. 650–668, 2010.

[109] S. Sandor and R. Leahy, "Surface-based labeling of cortical anatomy using a deformable atlas," *IEEE Transactions on Medical Imaging*, vol. 16, pp. 41–54, 1997.

[110] D.C. Van Essen and D. Dierker, "Surface-based and probabilistic atlases of primate cerebral cortex," *Neuron*, vol. 56, pp. 209–225, 2007.

[111] O. Lyttelton, M. Boucher, S. Robbins, and A. Evans, "An unbiased iterative group registration template for cortical surface analysis," *NeuroImage*, vol. 34, pp. 1535–1544, 2007.

[112] D.C. Van Essen, "A population-average, landmark- and surface-based (PALS) atlas of human cerebral cortex," *NeuroImage*, vol. 28, pp. 635–662, 2005.

[113] V.A. Magnotta, G. Harris, N.C. Andreasen, D.S. O'Leary, W.T. Yuh, and D. Heckel, "Structural MR image processing using the BRAINS2 toolbox," *Computerized Medical Images and Graphics*, vol. 26, pp. 251–264, 2002.

[114] R. Pierson, H. Johnson, G. Harris, H. Keefe, J.S. Paulsen, N.C. Andreasen, and V.A. Magnotta, "Fully automated analysis using BRAINS: AutoWorkup," *NeuroImage*, vol. 54, pp. 328–336, 2011.

[115] W. Lu, "A method for automated landmark constellation detection using evolutionary principal components and statistical shape models," M.S. thesis, The University of Iowa, Iowa City, IA, 2010.

[116] P. Viola and W. M. Wells III, "Alignment by maximization of mutual information," *International journal of computer vision*, vol. 24, pp. 137–154, 1997.

[117] H. Johnson, G. Harris, and K. Williams, "BRAINSFit: mutual information registrations of whole brain 3d images, using the insight toolkit," *The Insight Journal*, 2007.

[118] K. Pohl, W. Wells, A. Guimond, K. Kasai, M. Shenton, R. Kikinis, W. Grimson, and S. Warfield, "Incorporating non-rigid registration into expectation maximization algorithm to segment MR images," in *Medical Image Computing and Computer-Assisted Intervention MICCAI 2002*, Takeyoshi Dohi and Ron Kikinis, Eds., vol. 2488 of *Lecture Notes in Computer Science*, pp. 564–571. Springer Berlin / Heidelberg, 2002.

[119] C.J. Holmes, R. Hoge, L. Collins, R. Woods, A.W. Toga, and A.C. Evans, "Enhancement of MR images using registration for signal averaging," *Journal of Computer Assisted Tomography*, vol. 22, pp. 324–333, 1998.

[120] G. Harris, N.C. Andreasen, T. Cizadlo, J.M. Bailey, H.J. Bockholt, V.A. Magnotta, and S. Arndt, "Improving tissue classification in mri: a three-dimensional multispectral discriminant analysis method with automated training class selection," *Journal of Computer Assisted Tomography*, vol. 23, pp. 144–154, 1999.

[121] T. Vercauteren, X. Pennec, A. Perchant, and N. Ayache, "Diffeomorphic demons: efficient non-parametric image registration," *NeuroImage*, vol. 45, pp. S61–S72, 2009.

[122] S. Powell, V.A. Magnotta, H. Johnson, V.K. Jammalamadaka, R. Pierson, and N.C. Andreasen, "Registration and machine learning-based automated segmentation of subcortical and cerebellar brain structures," *NeuroImage*, vol. 39, pp. 238–247, 2008.

[123] R.C. Gonzales and R.E. Woods, *Digital image processing*, Prentice Hall, Upper Saddle River, N.J., 2nd edition, 2002.

[124] J. Koenderink, "The structure of images," *Biology Cybernetics*, vol. 50, pp. 363–370, 1984.

[125] R.A. Hummel, "Representations based on zero-crossings in scale-space," in *Readings in computer vision: issues, problems, principles, and paradigms*, M. A. Fischler and O. Firschein, Eds., pp. 753–758. Morgan Kaufmann Publishers Inc., San Francisco, CA, USA, 1987.

[126] P. Perona and J. Malik, "Scale-space and edge detection using anisotropic diffusion," *IEEE Transactions on pattern analysis and machine intelligence*, vol. 12, pp. 629–639, 1990.

[127] S. Jaume, P. Rondao, and B. Macq, "Open topology: a toolkit for brain isosurface correction," *The Insight Journal - 2005 MICCAI Open-Source Workshop*, 2005.

[128] W. Schroeder, K. Martin, and B. Lorensen, *The Visualization Toolkit*, Kitware, Inc., Clifton Park, N.Y., 4th edition, 2006.

[129] D.W. Shattuck and R.M. Leahy, "Automated graph-based analysis and correction of cortical volume topology," *IEEE Transaction on Medical Imaging*, vol. 20, pp. 1167–1177, 2001.

[130] X. Han, C. Xu, U. Braga-Neto, and J.L. Prince, "Topology correction in brain cortex segmentation using a multiscale, graph-based algorithm," *IEEE Transaction on Medical Imaging*, vol. 21, pp. 109–121, 2002.

[131] T. Saito and J. Toriwaki, "New algorithms for Euclidean distance transformation of an n-dimensional digitized picture with applications," *Pattern Recognition*, vol. 27, pp. 1551–1565, 1994.

[132] N. Kriegeskorte and R. Goebel, "An efficient algorithm for topologically correct segmentation of the cortical sheet in anatomical MR volumes," *NeuroImage*, vol. 14, pp. 329–346, 2001.

[133] W.E. Lorensen and H.E. Cline, "Marching cubes: A high resolution 3d surface construction algorithm," *Computer Graphics*, vol. 21, pp. 163–169, 1987.

[134] J. Rossignac and P. Borrel, "Multi-resolution 3D approximations for rendering complex scenes," in *Geometric Modeling in Computer Graphics*, B. Falcidieno and T. L. Kunii, Eds., pp. 455–465. Springer Verlag, Genova, Italy, 1993.

[135] M. Eck, T. De Rose, T. Duchamp, H. Hoppe, M. Lounsbery, and W. Stuetzle, "Multiresolution analysis of arbitrary meshes," in *Proceedings of the 22nd annual conference on Computer graphics and interactive techniques*, New York, NY, USA, 1995, pp. 173–181, ACM Press.

[136] W.J. Schroeder, J.A. Zarge, and W.E. Lorensen, "Decimation of triangle meshes," in *Proceedings of the 19th annual conference on Computer graphics and interactive techniques*, New York, NY, USA, 1992, pp. 65–70, ACM Press.

[137] H. Hoppe, "Progressive meshes," in *Proceedings of the 23rd annual conference on Computer graphics and interactive techniques*, New York, NY, USA, 1996, pp. 99–108, ACM Press.

[138] A. Gelas, A. Gouaillard, and S. Megason, "Surface meshes incremental decimation framework," *The Insight Journal*, vol. July-December, August 2008.

[139] A. Gouaillard, L. Flórez-Valencia, and E. Boix, "itkQuadEdgeMesh: a discrete orientable 2-manifold data structure for image processing," *The Insight Journal*, vol. July-December, July 2006.

[140] H. Gray, *Gray's Anatomy of the Human Body*, Lea&Febiger, Philadelphia, the United States, 20th, u.s. edition, 1918.

[141] B. Yeo, Mert Sabuncu, Tom Vercauteren, Nicholas Ayache, Bruce Fischl, and Polina Golland, "Spherical demons: Fast surface registration," in *Medical Image Computing and Computer-Assisted Intervention MICCAI 2008*, vol. 5241 of *Lecture Notes in Computer Science*, pp. 745–753. Springer Berlin / Heidelberg, 2008.

[142] L. Ibanez, B. Yeo, and P. Golland, "Iterative smoothing of field data in spherical meshes," *The Insight Journal*, vol. July-December, July 2009.

[143] W. Li, L. Ibanez, N.C. Andreasen, and V.A. Magnotta, "The effectiveness of geometry features on multi-resulotion diffeomorphic demons registration in the implementation of human cortex surface parcellation," in *Proceedings of 2011 IEEE International Symposium on Biomedical Imaging*, Chicago, IL, 2011.

[144] K. Hormann, B. Lévy, and A. Sheffer, "Mesh parameterization: Theory and practice," in *ACM SIGGRAPH Course Notes*, San Diego, CA, 2007, vol. 2, ACM Press.

[145] S. Angenent, S. Haker, A. Tannenbaum, and R. Kikinis, "On the laplace-beltrami operator and brain surface flattening," *IEEE Transactions on Medical Imaging*, vol. 18, pp. 700–711, 1999.

[146] S. Haker, S. Angenent, A. Tannenbaum, R. Kikinis, G. Sapiro, and M. Halle, "Conformal surface parameterization for texture mapping," *IEEE Transactions on Visualization and Computer Graphics*, vol. 6, pp. 181–189, 2000.

[147] M.P. Do Carmo, *Differential geometry of curves and surfaces*, Prentice-Hall, Englewood Cliffs, N.J., 1976.

[148] A. Gelas and A. Gouaillard, "Parameterization of discrete surfaces," *The Insight Journal*, vol. July-December, December 2007.

[149] J. A. Sethian, "Fast marching methods," *Society for Industrial and Applied Mathematics*, vol. 41, pp. 199–235, 1999.

[150] W.T. Tutte, "How to draw a graph," in *Proceedings of the London Mathematical Society*, 1963, vol. 13, pp. 743–767.

[151] J.P. Thirion, "Image matching as a diffusion process: an analogy with maxwell's demons," *Medical Image Analysis*, vol. 2, pp. 243–260, 1998.

[152] J.P. Thirion, "Non-rigid matching using demons," in *Computer Vision and Pattern Recognition, 1996. Proceedings CVPR '96, 1996 IEEE Computer Society Conference on*, 1996, pp. 245–251.

[153] P. Cachier, E. Bardinet, D. Dormont, X. Pennec, and N. Ayache, "Iconic feature based nonrigid registration: the PASHA algorithm," *Computer Vision and Image Understanding*, vol. 89, pp. 272–298, 2003.

[154] T. Vercauteren, X. Pennec, A. Perchant, and N. Ayache, "Non-parametric diffeomorphic image registration with the demons algorithm," in *Medical Image Computing and Computer-Assisted Intervention MICCAI 2007*. 2007, vol. 4792 of *Lecture Notes in Computer Science*, pp. 319–326, Springer Berlin / Heidelberg.

[155] P. Cachier and N. Ayache, "Isotropic energies, filters and splines for vector field regularization," *Journal of Mathematical Imaging and Vision*, vol. 20, pp. 251–265, 2004.

[156] T. Vercauteren, *Image registration and mosaicing for dynamic in vivo fibered confocal microscopy*, Ph.D. thesis, École Nationale Supérieure des Mines de Paris, Paris, France, 2008.

[157] V.V. Gorbatsevich, A.L. Onishchik, and E.B. Vinberg, *Foundations of Lie theory and Lie transformation groups*, Springer, 1997.

[158] V. Arsigny, O. Commowick, X. Pennec, and N. Ayache, "A log-euclidean framework for statistics on diffeomorphisms," in *Medical Image Computing and Computer-Assisted Intervention MICCAI 2006*, R. Larsen, M. Nielsen, and J. Sporring, Eds., vol. 4190 of *Lecture Notes in Computer Science*, pp. 924–931. Springer Berlin / Heidelberg, 2006.

[159] L. Ibanez, M. Audette, B.T.T. Yeo, and P. Goland, "Rotational registration of spherical surfaces represented as quadedge meshes," *The Insight Journal*, vol. January-June, 2009.

[160] L. Ibanez, M. Audette, B.T.T. Yeo, and P. Goland, "Spherical demons registration of spherical surfaces," *The Insight Journal*, vol. July-December, 2009.

[161] L. Ibanez, W. Li, V.A. Magnotta, B.T.T. Yeo, and P. Goland, "Multi-resolution demons registration of spherical surfaces," *The Insight Journal*, vol. January-June, 2010.

[162] G. Lehmann, "Combining labeled images with itk," *The Insight Journal*, vol. January-June, 2007.